



UNIVERSITÀ DEGLI STUDI DELL'AQUILA

Department of Civil, Construction-Architectural and  
Environmental Engineering

**DOCTORAL THESIS**

---

**Remote Sensing: integration  
between optical and SAR images  
for shoreline extraction**

---

Ph.D Course in Civil, Construction-Architectural  
and Environmental Engineering

XXXIII cycle

SSD

**ICAR/06**

Candidate  
**Sara Zollini**

Curriculum  
**Civil-Environmental**

Course Coordinator  
**Prof. Marcello Di Risio**

Thesis Tutor  
**Prof. Donatella Dominici**

Academic Year 2019 - 2020



---

REMOTE SENSING:  
INTEGRATION BETWEEN  
OPTICAL AND SAR IMAGES  
FOR SHORELINE EXTRACTION

Sara Zollini

Prof. Donatella Dominici

---

---

**Remote Sensing: integration between optical and SAR images for shoreline extraction**

Sara Zollini  
Candidate ID number: 255370

Department of Civil, Construction-Architectural and Environmental Engineering-  
DICEAA  
University of L'Aquila

Copyright © 2020, Sara Zollini. All rights reserved.

Material for which the author is the copyright owner cannot be used without the written permission of the author. The permission to reproduce copyright protected material does not extend to any material that is copyright of a third party; authorization to reproduce such material must be obtained from the copyright owners concerned. This thesis has been typeset by L<sup>A</sup>T<sub>E</sub>X and phdiceaa class.

Website: <http://diceaa.univaq.it/>

*To my mum and dad, to Francesco.*  
*“Happiness can be found, even in the darkest of times,  
if one only remembers to turn on the light.”*  
*J.K. Rowling*

[Blank page]

# ACKNOWLEDGEMENTS

I would like to thank my tutor, Prof. Donatella Dominici, who guided me from my Bachelor degree until this PhD with her knowledges, expertise and experience not only in geomatic field.

Thanks to Maria, researcher at geomatic laboratory, for her knowledges and capabilities, for all the time we spent together and for all the experiences we lived.

Thanks to Peppe, geomatic laboratory technician, for the work and for his availability.

Thanks to all the UNIVAQ. I am spending the best years of my life there.

Thanks to the reviewers of this thesis, Prof. Michele Crosetto and Prof. Francesco Carlo Nex for the precious suggestions they give to improve this work. Thanks in advance to Professors González Aguilera, Aristodemo and Kadkhodaei of the examining board.

Thanks to Prof. Paolo Massimo Buscema and all the staff in Semeion research centre, for their help in the mathematical part, for the interesting days we spent together trying the algorithms I used in this research and for the best amatriciana ever.

I would also like to show my gratitude to my tutors in Spain, María Cuevas, researcher, and Oriol Monserrat, senior researcher, who made me enter to the fascinating and complex world of SAR and understand what “research” means. Thanks also to Eduard, Jesús and the UPC team for providing the GPS measurements in Castelldefels’ case study.

Thanks to Div. For everything. Only God knows the good and the bad we lived, and we are still here, together and for each other. I am done talking.

Thanks to Piera, my eternal classmate and my personal confidant for 14 years. I wish we can continue to grow old together.

I would thank Crisinha, my special Brazilian friend. “Few” kilometres divide us, but we are chained by heart. I will always “say a little prayer for you”.

Thanks to Samita, my friend from Nepal. We do not need lots of words to understand each other. I miss you so much.

Thanks to my “snack friend”, Peppe, Luca, Angela, Lollo and Antonella and also Betty, Asietta and Mattia. Quarantine was sweeter with you.

Thanks to the PhD friends, Cioccolatino, Ballerino and Alessietto for sharing with me this period of life and for our tasty and delicious dinners in the most remote places in the world.

Thanks to Sam, Marty and Ary, my travel friends. This year stopped us, but I am sure we will recover as well as we could possibly imagine.

Thanks to Federico, Valentina and all their family. They are always present in my life.

Thanks to Mary, a friendship born among the school desks that still survives.

Thanks to the music, faithful companion of life. I wish that this year all the projects with my “musical friends” can be realised.

Thanks to Qiu and Xini, my Chinese friends, always funny and smiling, and to all the amazing friends I met in Barcelona, Anna, Giorgio, Roberto, Ludovico, Guido, Aldina, Annalisa, Marco, Alessia, Trinh, Vrinda, Jadoon, Maham, Carlos, Mixalis and all. The fantastic experience I made would not have been the same without you.

Thanks to my family, my favourite and only cousin Gaia, for her sweetness and honesty, aunts Lallina and Daniela, uncles Giulio and Leonardo, grandparents Anna, Vincenzo (my soul), Jole and Remo and all the relatives around the world. Thanks also to my parents-in-law Mara and Pietro and sister-in-law Silvia. Thanks to Pieradolfo, Marika and Elsinia, that are always present, also during the darkest times. Family is the greatest value.

Thanks to mum and dad, my real driving force. Thanks for supporting me in every situation of my life. When I think to give up, you are always there to let me go beyond my limits. I love you.

Finally, thanks to me, to my perseverance and my determination. I pray for a more peaceful 2021.

[Blank page]



# ABSTRACT

Coastal environments are facing constant changes over time due not only to their dynamic nature but also to geological, geomorphological, hydrodynamic, biological, climatic and anthropogenic factors. Nowadays, erosion phenomena exceed those of accretion. For these reasons, the monitoring of these areas is crucial for the safeguarding of the cultural heritage and the populations living there. Knowledge of shoreline dynamics helps to understand and study a wide range of coastal area studies and, in general, its management and planning. The focus of this research is based on the integration between optical and SAR data for shoreline extraction. High (Sentinel-1 SAR and Sentinel-2 optical) and very high (WorldView-2 optical) resolution satellite images were used. Two coastal sites, Ortona (Chieti, Italy) and Castelldefels (Barcelona, Spain) were detected. After pre-processing, necessary for geometric and radiometric corrections, enhancement techniques were applied in order to increase the readability of the data. Several indices, algorithms and filters were tested. The experimentation critically analysed algorithms already commonly used in literature and led to the study of new algorithms within the world of artificial intelligence. The innovation has conducted to their experimentation on the case studies taken into account in this thesis. These algorithms are the ACM Systems (Active Connection Matrix), which were compared to the common ones considering, as ground truth, once the shoreline manually extracted by visual inspection and once by GPS measurements. The results showed that the ACM Systems, and in particular the Contractive Maps and the J-Net Dynamic, provide a better definition and extraction of the shorelines, which were closer to the reference ones, compared to the most common methodologies. They reached, in most of the tests, a sub-pixel/pixel accuracy. Moreover, one of the aim of this work was to develop a semi-automatic methodology for instantaneous shoreline extraction, mainly using Sentinel images as part of Copernicus programme, which provide full, open and free-of-charge data, in addition to ease of access and use. Through the aforementioned study, it was also demonstrated that the ACM Systems make the best of SAR data, because they were found to be less sensitive to the speckle effect. The new methodology can quickly extract the shorelines of images taken in different time periods and, therefore, evaluate any occurred change. In this way, a concrete possibility of an appropriate intervention plan can be developed by institutions to preserve the environment.



# SOMMARIO

L'ambiente costiero sta subendo, nel corso del tempo, continui cambiamenti dovuti non solo alla sua natura dinamica ma anche a fattori geologici, geomorfologici, idrodinamici, biologici, climatici e antropici. Ad oggi, i fenomeni di erosione superano quelli di sedimentazione. Per questo, il monitoraggio di tali aree è fondamentale per la salvaguardia del patrimonio culturale e delle popolazioni che vi abitano. La conoscenza delle dinamiche del litorale aiuta a comprendere un'ampia gamma di studi sull'area costiera e sulla sua gestione e pianificazione. Il focus di questa ricerca si basa sull'integrazione di dati ottici e SAR per l'estrazione della linea di riva istantanea. Le immagini utilizzate sono state quelle satellitari ad alta (Sentinel-1 SAR e Sentinel-2 ottiche) ed altissima risoluzione (WorldView-2 ottiche). Sono stati studiati due siti costieri, Ortona (Chieti, Italia) e Castelldefels (Barcellona, Spagna). Dopo una pre-elaborazione, necessaria per correggere distorsioni geometriche e radiometriche, sono state applicate tecniche di enhancement per aumentare la leggibilità del dato. Diversi indici, algoritmi e filtri sono stati testati. La sperimentazione ha analizzato in modo critico algoritmi già comunemente utilizzati in letteratura e ha portato allo studio di nuovi algoritmi del mondo dell'intelligenza artificiale. L'innovazione ha condotto alla sperimentazione di essi sui casi di studio della presente tesi. Tali algoritmi sono i Sistemi ACM (Active Connection Matrix), che sono stati confrontati con i quelli comuni considerando, come verità a terra, una volta la linea di riva estratta manualmente tramite ispezione visiva e un'altra tramite misure GPS. I risultati hanno mostrato che i Sistemi ACM, ed in particolare il Contractive Maps e il J-Net Dynamic, forniscono una migliore definizione ed estrazione della linea di riva, avvicinandosi maggiormente a quella di riferimento, rispetto alle metodologie più comuni e raggiungendo, nella maggior parte dei test, precisioni dell'ordine del sub-pixel/pixel. Inoltre, uno degli scopi di questo lavoro è stato quello di mettere a punto una nuova metodologia semi-automatica per l'estrazione della linea di riva istantanea, utilizzando prevalentemente immagini Sentinel come parte del programma Copernicus, il quale fornisce dati completi, liberi e gratuiti, facili da reperire ed utilizzare. Tramite il suddetto studio, si è anche dimostrato che i Sistemi ACM sono in grado di sfruttare al meglio il dato SAR, perché sono risultati essere meno sensibili all'effetto dello speckle. La nuova metodologia può essere sfruttata per estrarre in maniera rapida le linee di riva di immagini catturate in istanti di tempo differenti e, quindi, per valutarne l'eventuale cambiamento avvenuto. In questo modo, è possibile facilitare la gestione di un piano di intervento da parte delle istituzioni a favore della salvaguardia del luogo.



# CONTENTS

<b>1</b>	<b>Shoreline extraction - State of art</b>	<b>1</b>
1.1	Introduction . . . . .	2
1.2	Why shoreline studies? . . . . .	4
1.3	Definitions . . . . .	10
1.4	State of art for shoreline detection . . . . .	15
1.4.1	Remote sensing techniques for shoreline detection . . . . .	17
<b>2</b>	<b>Multispectral and SAR sensors</b>	<b>21</b>
2.1	Introduction . . . . .	22
2.2	About resolutions . . . . .	25
2.3	Passive sensors: optical images . . . . .	26
2.3.1	Multispectral sensors . . . . .	29
2.3.2	Geometric distortion in optical images . . . . .	30
2.3.3	Radiometric distortion in optical images . . . . .	32
2.4	Active sensors: SAR images . . . . .	32
2.4.1	SAR geometry . . . . .	34
2.4.2	SAR images resolution . . . . .	35
2.4.3	Geometric Distortions . . . . .	37
2.4.4	Radiometric distortion: Speckle . . . . .	38
2.5	Satellite platforms . . . . .	39
2.5.1	Sentinel-1 . . . . .	39
2.5.2	Sentinel-2 . . . . .	43
2.5.3	WorldView-2 . . . . .	45
2.5.4	COSMO-SkyMed . . . . .	46
<b>3</b>	<b>Satellite image analysis</b>	<b>49</b>
3.1	Introduction . . . . .	50
3.2	Image pre-processing . . . . .	52
3.2.1	Orthorectification . . . . .	52
3.2.2	Georeferencing . . . . .	56
3.2.3	Resampling . . . . .	56
3.2.4	Pansharpen . . . . .	57
3.3	Image processing: state of art . . . . .	58
3.3.1	Decorrelation Stretch . . . . .	58

3.3.2	NDVI, Normalized Difference Vegetation Index . . .	59
3.3.3	WVWI, WorldView Water Index . . . . .	59
3.3.4	Supervised and Unsupervised Classification . . . . .	60
3.3.5	Canny Edge Detector . . . . .	65
3.4	Image processing: new experimental algorithms . . . . .	66
3.4.1	Automata Rule . . . . .	68
3.4.2	New IAC, Interactive Activation and Competition Network . . . . .	69
3.4.3	New CS, Constraint Satisfaction Networks . . . . .	70
3.4.4	CM, local Contractive Maps . . . . .	70
3.4.5	J-Net Dynamic . . . . .	70
<b>4</b>	<b>First case study:</b>	
	<b>Ortona's coast</b>	<b>73</b>
4.1	Introduction . . . . .	74
4.2	WorldView-2 . . . . .	77
4.2.1	Pre-Processing . . . . .	77
4.2.2	Processing . . . . .	78
4.2.3	Results and discussion . . . . .	83
4.3	Sentinel-1 . . . . .	85
4.3.1	Pre-processing . . . . .	86
4.3.2	Processing . . . . .	89
4.3.3	Results and discussions . . . . .	92
<b>5</b>	<b>Second case study:</b>	
	<b>Castelldefels' coast</b>	<b>101</b>
5.1	Introduction . . . . .	102
5.2	Dataset . . . . .	104
5.3	Pre-processing . . . . .	106
5.3.1	Sentinel-2 . . . . .	106
5.3.2	Sentinel-1 . . . . .	108
5.4	Processing . . . . .	109
5.5	Results and discussion . . . . .	111
<b>6</b>	<b>Conclusion</b>	<b>115</b>
6.1	Future studies . . . . .	118
	<b>References</b>	<b>120</b>
	<b>Terms and abbreviations</b>	<b>155</b>
<b>A</b>	<b>Appendix A: ACM systems</b>	<b>163</b>
A.1	Automata Rule . . . . .	163
A.2	New IAC . . . . .	164
A.3	New CS . . . . .	165

---

A.4 Contractive Maps . . . . .	166
A.5 J-Net Dynamic . . . . .	168
<b>B Appendix B: ACM elaborations</b>	<b>171</b>

[Blank page]

# LIST OF FIGURES

1.1	Trend of the global mean sea level from 1880 to 2019 . . . . .	5
1.2	Trend prevision of the global mean sea level by 2100 . . . . .	5
1.3	Overall gained and lost of land and active zone in all the Earth	7
1.4	Map and graph of the coastal erosion patterns in Europe (2004) . . . . .	8
1.5	Map and graph of the coastal erosion patterns in some eu- ropean country (2004) . . . . .	10
1.6	Typical beach profile with the respective terminology. . . . .	11
1.7	Spatial relationship between many of the commonly used shoreline indicators in literature. . . . .	14
2.1	Remote Sensing workflow . . . . .	22
2.2	Passive and active remote sensors . . . . .	23
2.3	Scheme about optical and radar sensors with their typical wavelengths ranges . . . . .	24
2.4	How an image is formed . . . . .	26
2.5	Structure of image arranged in pixels . . . . .	27
2.6	RGB bands which form the natural colour image . . . . .	29
2.7	Example of how a multispectral image is composed . . . . .	30
2.8	First example of geometric distortion: objects far from the center of the image along the nadir show not only their tops visible but also their side part . . . . .	31
2.9	External and internal distortions in optical satellite images	31
2.10	How a synthetic aperture radar works . . . . .	33
2.11	Imaging geometry for a synthetic aperture radar imaging system . . . . .	34
2.12	SAR range and azimuth resolutions . . . . .	36
2.13	SAR geometric distortions . . . . .	37
2.14	Speckle effect . . . . .	38
2.15	Sentinel-1 observation scenario . . . . .	40
2.16	Sentinel-1 IW acquisition mode: images are formed by three swaths and many bursts . . . . .	41
2.17	Sentinel-1 modes . . . . .	42

2.18	Sentinel-2 bands and relative wavelengths . . . . .	44
2.19	Sentinel-2 coverage and revisit time . . . . .	45
2.20	WorldView-2 bands . . . . .	46
2.21	COSMO-SkyMed acquisition modes . . . . .	47
3.1	Orthorectification . . . . .	52
3.2	Rigorous model for orthorectification . . . . .	53
3.3	GCP: Ground Control Point . . . . .	55
3.4	Resampling techniques . . . . .	57
3.5	Pansharpening . . . . .	57
3.6	Steps for supervised classification . . . . .	61
3.7	Parallelepiped classification . . . . .	62
3.8	Gaussian Probability Distribution Function (PDF) . . . . .	63
3.9	Spectral Angle Mapping . . . . .	64
3.10	Unsupervised classification steps . . . . .	64
3.11	The $I_{(u_{ij})}$ neighborhood of an example image with $radius=1$ and the relevant connections. . . . .	67
3.12	Groups of ACM Systems . . . . .	68
3.13	Pixel-unit connections with Automata Rule . . . . .	69
3.14	J-Net Dynamic scheme . . . . .	71
4.1	WorldView-2 raw image. Scene: Ortona's coast . . . . .	77
4.2	Results of the decorrelation stretch . . . . .	79
4.3	Results of NDVI . . . . .	80
4.4	Results of WWVI . . . . .	81
4.5	Unsupervised (on the left) and supervised classification (on the right) . . . . .	81
4.6	NDVI image (a), WWVI image (b), and application of CM on the NIR2 band image (c) . . . . .	82
4.7	Profiles over three sample distances on the pansharpened image: Profile 1 is blue, Profile 2 green, and Profile 3 red . . . . .	83
4.8	Profiles over three sample distances . . . . .	84
4.9	Pre-processed and georeferenced Sentinel-1 image . . . . .	89
4.10	Canny algorithms applied on the pre-processed Sentinel-1 image acquired on 31 December 2019. . . . .	90
4.11	Application of the J-Net Dynamic algorithm on the SAR Sentinel-1 image acquired on 31 December 2016. . . . .	91
4.12	J-Net algorithm tested on NIR2 band of the WorldView-2 image. . . . .	93
4.13	WorldView-2 image with three shorelines: the red line is the manually extracted shoreline; the yellow one is generated using the WWVI and the blue one from the J-Net Dynamic algorithm. . . . .	94

---

4.14	SAR Sentinel-1 image on the background showing four shorelines . . . . .	94
4.15	Ten transects every 100 m, drawn from the land to the sea, to calculate the intersection between them and seven shorelines extracted from WorldView-2, WWVI, J-Net Dynamic on the VHR image, Sentinel-1, Sentinel-2, Canny and J-Net Dynamic on the HR image . . . . .	96
5.1	Crops of the original Sentinel-2 a) and Sentinel-1 b) images	105
5.2	Sentinel-2 tested input data for Castelldefels shoreline extraction . . . . .	106
5.3	Sentinel-2 images results tested as input data for Castelldefels shoreline extraction . . . . .	107
5.4	Sentinel-1 pre-processing steps . . . . .	108
5.5	From the original image to the shoreline extraction . . . . .	109
5.6	Zoom on step e) of figure 5.5 . . . . .	110
5.7	Semi-automatic methodology chain to extract shorelines . .	111
B.1	ACM Batch software platform . . . . .	171
B.2	Four-band image elaborated by ACM filters . . . . .	172
B.3	Coastal image elaborated by ACM filters . . . . .	173
B.4	Coastal plus NIR2 band image elaborated by ACM filters .	174
B.5	NIR2 band image elaborated by ACM filters . . . . .	175

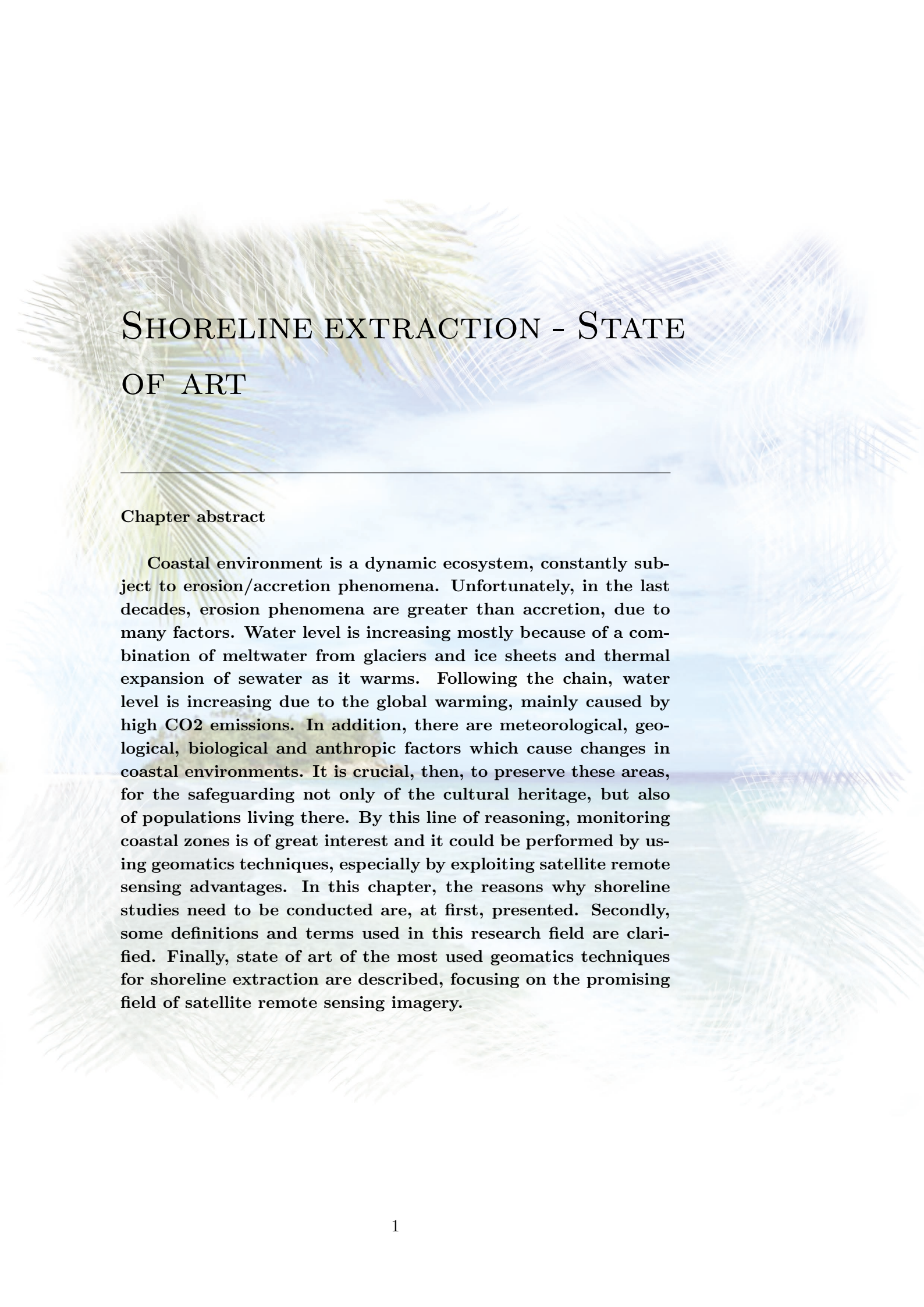
[Blank page]

# LIST OF TABLES

1.1	Percentage of coastal dynamic in European Seas and Ocean. (European Environment Agency, 2004) . . . . .	8
1.2	Shoreline changes between 1950/1999 and 2000/2007 (ISPRA - Istituto Superiore per la Prevenzione e la Ricerca Ambientale, 2011, 2014). . . . .	9
2.1	Incidence angle, resolutions, swath width and polarization of Sentinel-1 acquisition modes (ESA, European Space Agency, ndg) . . . . .	43
2.2	WorldView-2 characteristics . . . . .	45
4.1	Differences between the reference images and the other filters at the shoreline (m) . . . . .	85
4.2	List of the Sentinel-1 images used for Ortona’s coast analysis.	86
4.3	I Index values (both in metres and in pixel) and percentage of increase for VHR optical and HR Sentinel-1 images . . .	95
4.4	Statistic table. The means and the standard deviations have been calculated on the difference between the reference shorelines with the tested algorithms. The difference has been calculated on the values obtained from the intersection between the transects and the seven shorelines. . . . .	96
5.1	Dataset: Sentinel-2 and Sentinel-1 images taken into account for shoreline extraction. The time gap is the number of days between GPS measurments and the date of the images. . .	104
5.2	Sentinel-2 dataset . . . . .	105
5.3	Sentinel-1 dataset. In bold, the days of interest, while the others were used to better remove the speckle. . . . .	105
5.4	Mean and standard deviation between Sentinel-2 and GPS reference images in terms of distance by using J-Net Dynamic algorithm . . . . .	111
5.5	Mean and standard deviation between Sentinel-1 and GPS reference images in terms of distance by using J-Net Dynamic algorithm . . . . .	112

5.6	Mean and standard deviation between Sentinel-2 and GPS reference images in terms of distance by using Canny edge detector . . . . .	113
5.7	Mean and standard deviation between Sentinel-1 and GPS reference images in terms of distance by using Canny edge detector . . . . .	114
A.1	Some of the rules available to create new images . . . . .	167

[Blank page]



# SHORELINE EXTRACTION - STATE OF ART

---

## Chapter abstract

Coastal environment is a dynamic ecosystem, constantly subject to erosion/accretion phenomena. Unfortunately, in the last decades, erosion phenomena are greater than accretion, due to many factors. Water level is increasing mostly because of a combination of meltwater from glaciers and ice sheets and thermal expansion of seawater as it warms. Following the chain, water level is increasing due to the global warming, mainly caused by high CO<sub>2</sub> emissions. In addition, there are meteorological, geological, biological and anthropic factors which cause changes in coastal environments. It is crucial, then, to preserve these areas, for the safeguarding not only of the cultural heritage, but also of populations living there. By this line of reasoning, monitoring coastal zones is of great interest and it could be performed by using geomatics techniques, especially by exploiting satellite remote sensing advantages. In this chapter, the reasons why shoreline studies need to be conducted are, at first, presented. Secondly, some definitions and terms used in this research field are clarified. Finally, state of art of the most used geomatics techniques for shoreline extraction are described, focusing on the promising field of satellite remote sensing imagery.

## 1.1 Introduction

“Shoreline: the edge of a body water” (American Heritage Dictionary of the English Language, 2016).

Definition of “shoreline” has always been a topic of great debate. The shoreline is the strip of land that delimits a natural body of water. It differs from coastline, which is a strip of land of indefinite length and width that extends inland starting from the shoreline (Boak and Turner, 2005). The main problem of its definition concerns its nature. The coastal environment is a dynamic ecosystem, in which erosion phenomena are influenced by numerous factors including meteorological/climatic, geological, biological, and anthropic elements (Lasalandra, 2009). Moreover, shoreline depends on waves and tides. This represents a great threat, not only to the national heritage and economy, but also to human life. Close to the coast there are houses, structures and infrastructures. For these reasons, constant monitoring and management of coastal area is of great relevance. Knowledge of shoreline dynamics helps to understand and study a wide range of coastal area studies, like erosion - accretion analysis, extraction of the boundary between private and state owned areas, hazard mapping and, in general, management and planning of coastal zone. In addition, by means of the knowledge of shoreline positions, information about changes caused by man-made structures and beach dynamics can be provided (Manno et al., 2012). In this sense, the shoreline position is one of the most useful indicator for the study of coastal areas. In the first part of the thesis, the state of art of the methods used to determine and extract the shoreline are presented. Due to its dynamic nature, it is more appropriate the term “instantaneous shoreline”, which is the shoreline taken in a specific instant of time. By means of the comparison of the instantaneous shorelines taken in different periods of time, it is possible to detect and monitoring the dynamism of changes in coastal areas. However, the instantaneous shoreline does not give information about average conditions. Shoreline, in general, is not defined as a single line but within a strip, that is the range where it can be positioned during time.

Several geomatic techniques have been used for the presented purpose;

---

each of them allows to detect a specific feature. They are described in the following paragraphs. The identification of the shoreline involves two main steps (Boak and Turner, 2005):

1. selection and definition of shoreline indicator features;
2. detection of the chosen shoreline features within the available data sources.

The most common method is the simple visual interpretation but, recently, photogrammetric, satellite remote sensing, topographic data collection, digital image processing techniques have been considered valid methods to detect shoreline objectively. The requirements for shoreline delineation depend on the characteristics of the study purpose. For this reason, specific investigation methodologies have to satisfy different requirements, e.g., spatial resolution and shoreline position accuracy (from hundred to sub-metre), temporal and spatial scale of investigation (e.g., long- or medium-term analyses, regional or local scale), temporal frequency and response time for up-to-date information (Braga et al., 2013). The challenge is to create a robust and repeatable method to extract what is defined as “shoreline” among the available data sources.

## 1.2 Why shoreline studies?

“Is beach erosion a natural cycle or is it getting worse with rising sea levels?”  
(Scientific American, 2008).

Coastal zone represents one of the most populated and developed area in the world (Small and Nicholls, 2003). It has rich biodiversity and it is said that more than 45% of the worlds population lives there (Rajib, 2019). It has always been the subject of humans attraction because of their resources, starting from economic reasons, as it is the main access points to marine trade and transport, to cultural activities and cultural heritage. For these reasons, coastal zones have been growing and developing continuously and their utilisation has greatly increased during the recent decades (Neumann et al., 2015). This led inevitably to many changes of coastal environment not only from the point of view of the aspect, but also of the biodiversity and the entire ecosystem. Coastal zone is, indeed, a really vulnerable environment. The hazards, like typhoons, cyclones, hurricanes, storm surges, tsunami, represent a significant threats to the population, infrastructure and to the environment itself. There are also other hazards which are not visible or produce long-term effects, such as rising sea levels and coastal erosion. According to some authors (Church and White, 2011; Lindsey, 2019), global mean sea level has risen about 21 – 24cm since 1880 and a third of that coming in just the last decades. The rate of sea level rise is accelerating. It has more than doubled from 1.4mm per year throughout most of the twentieth century to 3.6mm per year from 2006-2015. In 2018, the global mean sea level was the highest annual average in satellite records from 1993 to 2019 (Fig. 1.1). It was one of four warmest years, behind 2016, 2015 and 2017, respectively. Scientists from NOAA’s National Centers for Environmental Information published the Bulletin of the American Meteorological Society (Blunden and Arndt, 2019), in which they report that “the 2018 average global CO<sub>2</sub> concentration was 407.4 parts per million, up from 405.0 parts per million last year. This is the highest ever measured in the modern 60-year measurement record”. They continue saying that “the globally averaged surface temperature was 0.30° – 0.40°C above the 1981 - 2010 average” which means that “for the seventh year in a row, the global

average sea level rose” and it is rising following an average rate of 3.1cm per decade.

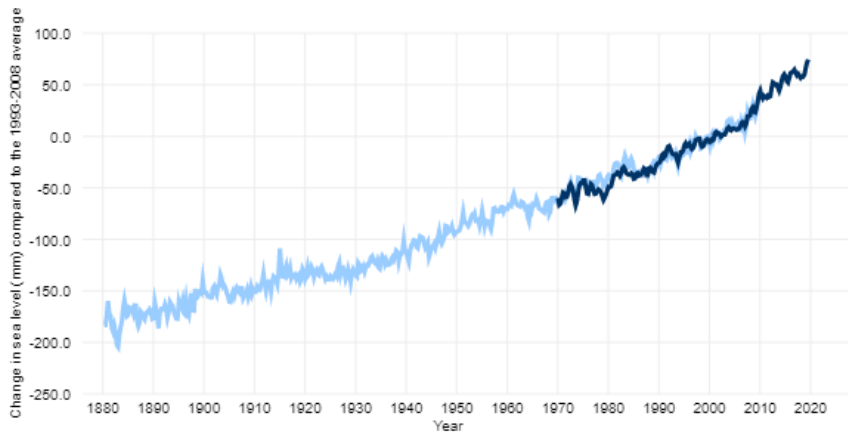


**Figure 1.1.** Trend of the global mean sea level from 1880 to 2019. The light blue line shows seasonal (3-months) sea level estimates by Church and White (2011). The blue line is based on University of Hawaii Fast Delivery (University of Hawaii, 2016) sea level data (Lindsey, 2019).

Even if the world follows a low CO<sub>2</sub> emission trend, global sea level will likely rise at least 0.3m by 2100. On the contrary, if it follows a pathway with high emissions, a worst-case scenario of as much as 2.5m by 2100 is possible (Sweet et al., 2017). In figure 1.2 is reported a graph where a possible trend of sea level for different GreenHouse Gas (GHG) pathways is showed.

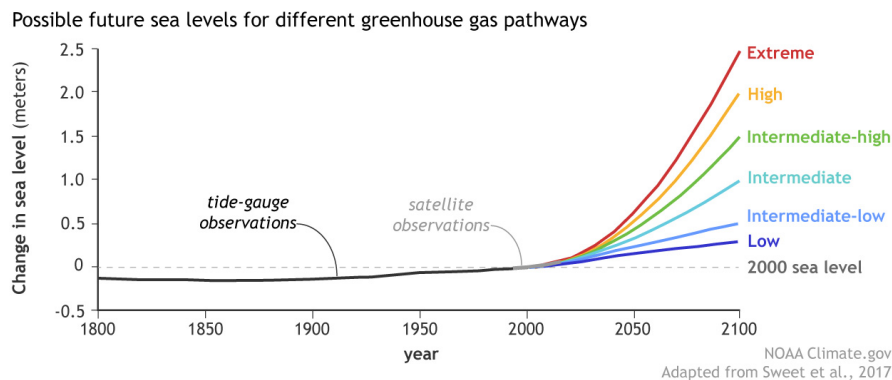


**Figure 1.2.** Trend prevision of the global mean sea level by 2100. Observed sea level from tide gauges (dark gray) and satellites (light gray) from 1800-2015, with future sea level through 2100 considering six possible future scenarios (colored lines). It is calculated assuming different potential future rates of greenhouse gas emissions which causes glacier and ice sheet loss (Lindsey, 2019; Parris et al., 2016; Sweet et al., 2017).

In the last decades, reduction of GHG emissions has been regulated

by a series of international agreements. Among them, the first and one of the most important is the Kyoto Protocol, where 70 signatory States have undertaken to reduce GHG emissions by 5% on average, compared to the 1990 level, within the five-years period 2008-2012 (Comini et al., 2011). Recently, the Paris Agreement was adopted to limit global warming to below 2 degree Celsius (UNFCCC, United Nations Climate Change, 2020).

The water level is rising mostly because of a combination of meltwater from glaciers and ice sheets and thermal expansion of seawater as it warms. The first main consequence is beach erosion. Beach erosion is defined as “the removal of sand from a beach to deeper water offshore or alongshore into inlets, tidal shoals and bays” (Scientific American, 2008). This is caused by various factors (natural, anthropological and so on), including the simple inundation of the land by rising sea levels resulting from the melting of the polar ice caps. Climate change is one of the main reason, but it is not the only one. Beaches are greatly influenced by the frequency and magnitude of storms along a particular shoreline. Extreme weather and climate-related hazards, such as heat waves, floods and droughts are becoming more frequent and intense in many regions. This will lead to adverse impacts on ecosystems, economic sectors, and human health and well-being. Another important reason is the human impact, through the construction of transport infrastructures and buildings in coastal zones, for agriculture, industry, ports, tourism and residential use. Dams are some of the most man-made infrastructure which have influence on erosion. Between 1960 and 1990 about 100 dams per year have been constructed and over 6000 large dams exist now in Europe, most of them in Spain (1200), followed by Turkey, France, Italy and the UK, each having more than 500 large dams (Universitat Autònoma de Barcelona, 2002). The damming of streams causes a decrease of sediments, as they are trapped behind the dams, and erosion in river delta.

A global and consistent evaluation of coastal morphodynamics over 32 years, from 1984 to 2015, based on satellite observations was studied by Mentaschi et al. (2018). They used more than 2 million virtual transects in the coastal active zone to estimate the land losses and gains. The coastal active zone is the dynamic part and it is defined as the buffer area between

permanent land and water. They demonstrate (Fig. 1.3) that the overall surface of eroded permanent land is almost  $28,000\text{km}^2$ , twice the surface of gained land over the same period. On the other hand, the surface of gained active zone (about  $25,000\text{km}^2$ ) is more than twice larger than the surface of lost active zone (about  $11,500\text{km}^2$ ).

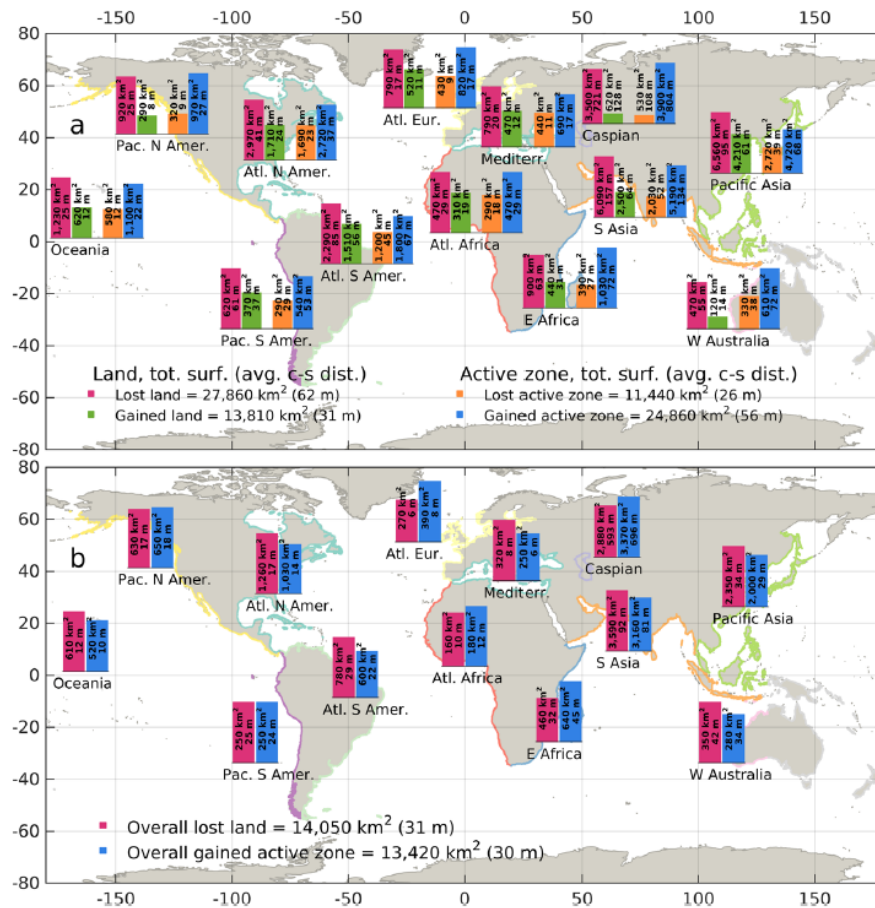


**Figure 1.3.** “Overall gained and lost (a), and gained-lost neat balance (b) of land and active zone, aggregated by continent/ocean and expressed in  $\text{km}^2$  and in cross-shore distance. The global aggregated quantities are also shown in both panels. Coastline colors identify the considered areas.” (Mentaschi et al., 2018)

To sum up, about the situation all over the world, erosion is more than accretion. They also analysed the differences region by region, founding out that Caspian Sea is the region with the highest change per unit coast (about  $600\text{m}$  of average net cross-shore land loss and  $700\text{m}$  of active zone gain), followed by Southern Asia (with an average land erosion of  $158\text{m}$  partially balanced by an accretion of  $69\text{m}$ ). Also Pacific Asia, Southern America, Eastern Africa and Western Australia present an average cross-shore erosion above  $50\text{m}$  (Mentaschi et al., 2018).

In Europe the situation is really alarming. In figure 1.4, the map and the graph of the coastal erosion patterns in Europe (2004) is showed.

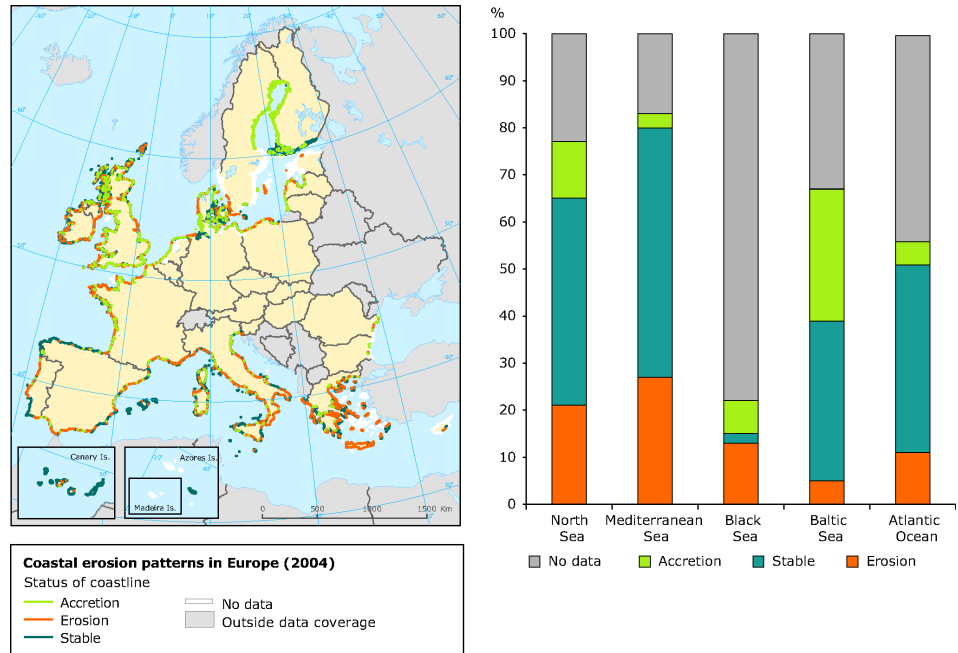


**Figure 1.4.** Map and graph of the coastal erosion patterns in Europe (2004). (European Environment Agency, 2004)

From figure 1.4 and table 1.1, it can be noticed that most of the European seas and oceans are eroding. The North Sea shows an accretion of about 9% less than the erosion; Black Sea and Atlantic Ocean of about 6%. Mediterranean Sea is the most worrying, indeed it presents a difference between erosion and accretion of about 24% (erosion more than accretion). Only Baltic Sea shows a trend for accretion (23% more than erosion).

**Table 1.1.** Percentage of coastal dynamic in European Seas and Ocean. (European Environment Agency, 2004)

Seas/Oceans	Erosion (%)	Stable (%)	Accretion (%)	No data (%)	Total (%)
<i>North Sea</i>	21,00	44,00	12,00	23,00	100,00
<i>Mediterranean Sea</i>	27,00	53,00	3,00	17,00	100,00
<i>Black Sea</i>	13,00	2,00	7,00	78,00	100,00
<i>Baltic Sea</i>	5,00	34,00	28,00	33,00	100,00
<i>Atlantic Ocean</i>	11,00	40,00	5,00	44,00	100,00

Italy is experiencing a number of environmental problems, including considerable coastline variations (Bianco et al., 2020; Bonaldo et al., 2019; Ietto et al., 2018; Roskopf et al., 2018). The data available on shoreline variation are of considerable concern: the extent of beach erosion ex-

ceeds the magnitude of sedimentation. Important ecosystems and areas of great biodiversity are risking destruction or severe impoverishment. Italy's coastal development is approximately 8300 km in length, and the natural coastline is about 7500 km long. More than 9% of the coastline is now artificial and bordered by work close to the shoreline (3.7%), ports (3%), and structures partially superimposed onto the coast (2.4%). About 3250 km of this are constituted by sandy coastlines (ISPRA - Istituto Superiore per la Prevenzione e la Ricerca Ambientale, 2011, 2014). According to Pranzini et al. (2015), 42% of Italian sandy coasts is eroding.

According to ISPRA data (ISPRA - Istituto Superiore per la Prevenzione e la Ricerca Ambientale, 2011, 2014), from 1950-1999, 46% of low-lying coastal areas underwent changes exceeding 25 m, and in particular, there are more stretches of coastline subject to erosion than sedimented. Analysis of the 2000-2007 changes confirmed this trend: 37% of the coastline underwent variations of over 10 m, and quantities of coastline subject to erosion (897 km) were still higher than those in progradation (Table 1.2).

**Table 1.2.** Shoreline changes between 1950/1999 and 2000/2007 (ISPRA - Istituto Superiore per la Prevenzione e la Ricerca Ambientale, 2011, 2014).

	1950/1999		2000/2007	
	Variations >± 25 m	Variations >± 5 m	Variations >± 5 m	Variations >± 5 m
Low-lying coastal	km	%	km	%
Total	4862	100.0	4715	100.0
Stable	2387	49.1	2737	58.0
Modified	2227	45.8	1744	37.0
Undefined	248	5.1	234	5.0
Backwardness	1170	24.1	895	19.0
Progress	1058	21.8	849	18.0

Same situation can be found in Spain, in particular in Catalan coast, which is subject to erosion phenomena, too. Within the EUROSION project (Salman et al., 2004), the erosion problems of european coasts was widely studied in 2004. The main goals of the project was to draw up (Sutherland, 2019):

- a map-based assessment of European coasts exposure to coastal erosion;
- state of art of coastal erosion management;

- guidelines to incorporate coastal erosion into environmental assessment, spatial planning and hazard prevention;
- policy recommendations to improve coastal erosion management.

The map of erosion about Catalan coasts shows a worrying scenario (Fig. 1.5). More than 30% of the coast is eroding and about 5% is sedimenting.

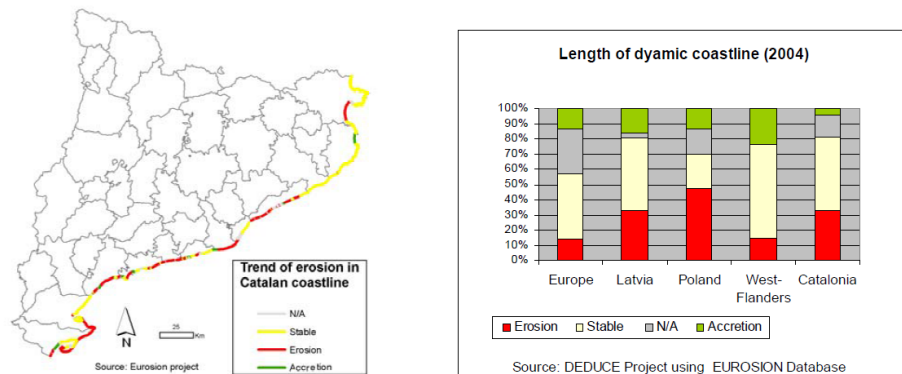


**Figure 1.5.** Map and graph of the coastal erosion patterns in some european country, like Latvia, Poland, West-Flanders and more specifically in Catalonia. (Domaradzki, nd)

It is clear that coastal environment needs to be protected, not only for the heritage but also to preserve human life. For the management of coastal areas, prevention assumes a central role. The protection of coastal green belts as well as the shoreline through coastal dykes or other hard infrastructures should be based on a carefully performed risk analysis. A complete analysis of coast protection structure currently present is shown in Pranzini et al. (2015). On the other hand, “softer” components, such as coastal watching and monitoring, are also important to help the preservation of these areas (Rajib, 2019). In this work, two coasts will be studied: the first one is in Italy centre, namely in Ortona (CH, Abruzzo region); the second one in Spain, in Castelldefels (Barcelona).

### 1.3 Definitions

The definition of “shoreline” is a really complex task. Although many authors use the terms *shoreline* and *coastline* as synonymous (Bagli et al., 2004; Gens, 2010; Misra and Balaji, 2015; Ouma and Tateishi, 2006), a few

authors have tried to make clear the concept. The shoreline is the line that divides a natural body of water from land. It is different from coastline, which is a strip of land of indefinite length and width that extends inland starting from the shoreline (Boak and Turner, 2005). The shoreline position change continuously not only because of the dynamic nature of water level but also because of cross-shore and along-shore sediment movements. The term “coastal dynamics” indicates the phenomena that govern the evolution of the coastal area over time. It is, therefore, appropriate to specify the temporal moment in which a shoreline is detected. It depends on which kind of application is going to be studied (Boak and Turner, 2005). As most of the applications consider images (derived from satellite, aircraft, videocamera, and so on), it is better talking about “instantaneous shoreline” that is the line extracted when the sensor acquires the radiation and creates the image. The shoreline is a time-dependent phenomenon that may exhibit substantial short-term (Morton and Speed, 1998) and long-term variability. So, it is necessary to give some explanations about coastal area.

In figure 1.6 a typical beach profile is showed.

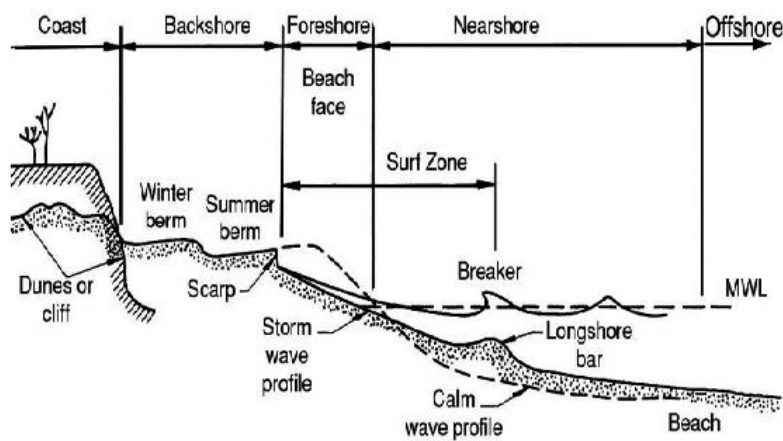


**Figure 1.6.** Typical beach profile with the respective terminology (Sorensen, 2005; Toure et al., 2019)

Figure 1.6 is representative of most of the beaches. There is the part farther away from the shoreline whose name is “coast”. Following the direction toward the sea, there are four areas: backshore, foreshore, nearshore and offshore. Although the coastal area is difficult to define due to the great variety of coastal morphological types, towards the mainland the limit can be

set using a morpho-vegetational for the high coasts and a sedimentological-vegetational criterion for the low coasts (e.g. internal limit of the dunes). The beach is the “living” portion of the coastal area. It is composed of an emerged part, between the shoreline and the front of the dunes, and a submerged part that extends from the shoreline to the line of the first deposition of the fine sediments. The submerged beach is composed by gravelly and/or sandy materials. The wave motion, governed by meteorological factors, can move them, according to both transversal and longitudinal movements with respect to the shoreline (Ferretti et al., 2003). During the spring season, in general, the sandy materials feed the emerged beach. On the contrary, in stormy weather conditions, as it generally happens during winter, materials of the emerged beach feed the submerged beach. Sea, through the action of waves, models significantly the coast conformation, carrying out a triple action of erosion, transport and accumulation of coastal sediments. By means of the movements, it can produce two main actions: erosion or sedimentation, which means retreat or progress of the shoreline, depending on sediments movements.

In nature, there are two main types of coasts (Baiocchi et al., 2011):

- high and rocky coasts;
- low and sandy coasts.

The beach profile is obviously different from coast to coast, so there is not an indicator which can be used for all the situations: functional indicators depend on the specific coast profile and the study purposes. A shoreline indicator is a feature that is used as variable to represent the “true” shoreline position. Indicators are divided into three main groups (Boak and Turner, 2005):

1. the ones based on a visually discernible coastal feature,
2. the ones based on a specific tidal datum,
3. the ones based on image processing techniques.

In the first group, indicators refer to features that can be visually seen, like, for example, a previous high-tide line or the wet/dry boundary. In the

---

second, indicators refer to a tidal datum determined by the intersection of the coastal profile with a specific vertical elevation, defined by the tidal constituents of a particular area, for example, mean high water (MHW) or mean sea level (Boak and Turner, 2005). A third group is taking hold, based on the application of image processing techniques, which are able to extract features not visible to human eyes (Pardo-Pascual et al., 2012).

In Boak and Turner (2005), a list of 45 examples of shoreline indicators from the shoreline analysis literature is presented. The authors specify the name of the indicator, a description of its feature, a generic classification, additional comments, the data source, the used detection technique, and references to relevant publications. Four of them are tidal datum based, 35 are based on visually discernible features and the remaining six are based on feature extraction from digital images.

Figure 1.7 shows the spatial relationship between many of the commonly used shoreline indicators. Unfortunately, many of the identified indicators do not take into account the spatial and temporal influences in shoreline position, like storms, wave conditions, seasonal influences and so on.

The most used indicator is the High-Water Line (HWL). It is generally detect by visual inspection, only in one case it is detected by supervised digital image analysis (Shoshany and Degani, 1992). Most of the authors in literature define the HWL as the line determined by “a change colour or gray tone caused by differences in water content of the sand on either side of the HWL” (Crowell et al., 1997; Smith and Zarillo, 1990; Stafford and Langfelder, 1971; Zhang et al., 2002). There are other shoreline indicators, like PIC (Pixel Intensity Clustering), CBD (Colour Band Divergence), ANN (Artificial Neural Network) which derive from digital image analysis. They differentiates pixels based on reflectance differences between wet and dry beach. In particular, PIC is an image segmentation method which differentiates pixels based on the colour difference between the “wet” and “dry” beach using H (Hue), S (Saturation), and V (Value); CBD differentiates pixels considering the reflectance properties of “wet” and “dry” regions based on a divergence of the relative intensity in the RGB spectrum; ANN differentiates pixels based on the color difference between the “wet” and “dry” beach using an artificial neural network. The RGB values of a pixel

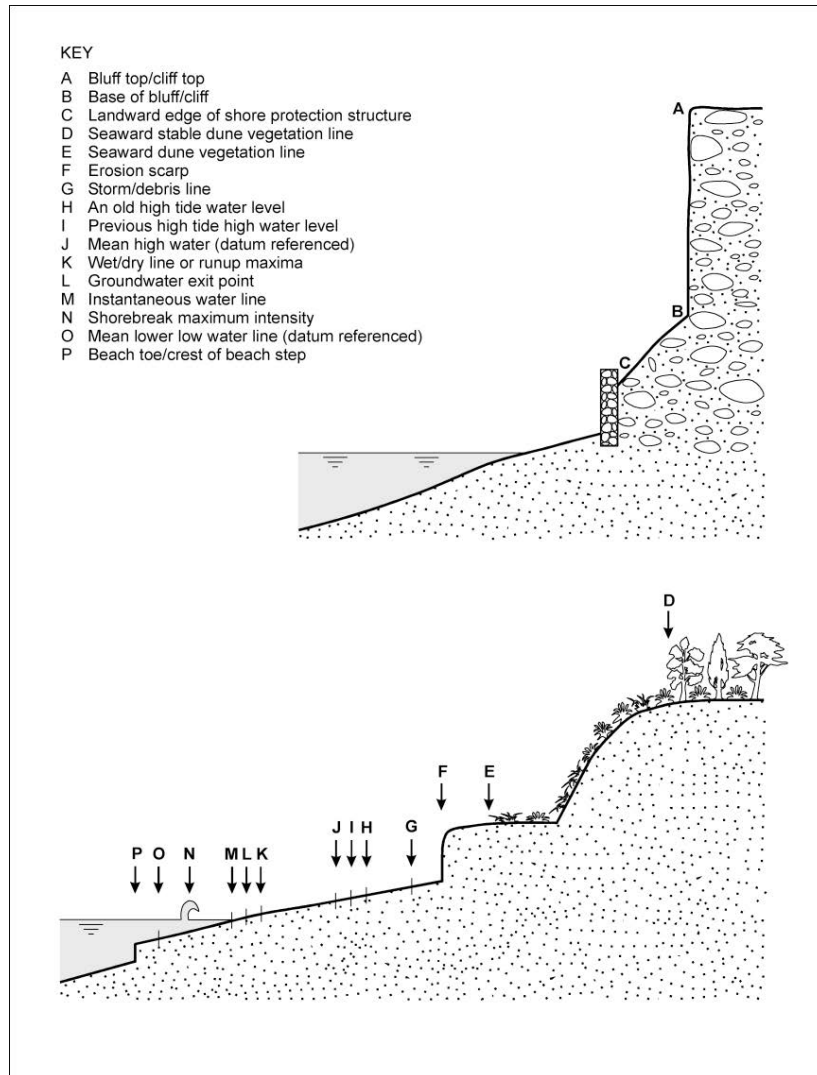


**Figure 1.7.** Spatial relationship between many of the commonly used shoreline indicators in literature (Boak and Turner, 2005)

are the inputs to ANN while the output is a binary classification of either water (0) or sand (1). As reported by Boak and Turner (2005), these indicators can determine an objective, repeatable (scientifically valid) and automated (so very quick) shoreline.

To sum up, the identification of the shoreline involves two steps (Boak and Turner, 2005):

1. selection and definition of shoreline indicator;
2. choice of the data source, useful for the chosen indicator.

The coastal area is subject to changes due to its own nature and to the growing human pressure; on the coast there are more than two thirds of

---

the world population (Baiocchi et al., 2011). Therefore, there is the need to support coastal areas by monitoring the shoreline with frequent surveys, in order to keep track of seasonal variations or singularities induced by intense storms.

In this work, satellite images are processed to extract the shoreline, taking into account the aforementioned indicators, especially the CBD. In the next paragraph, a state of art about the techniques used to extract the shoreline is presented.

## 1.4 State of art for shoreline detection

In this paragraph, state of art about how shoreline has been extracted is presented. There is a great variability of geomatic data source to examine the position of the shoreline: GNSS, aerial photography, video imaging, remote sensing, beach survey, LIDAR, microwave and multi-spectral sensors, and so on. None of them is used individually, but, in all the studies, the techniques are used in synergy, taking advantage of all the sensors features. There is no single method for modeling the shoreline, although over the last ten years, great progress has been made in mapping technology, ranging from the development of new and increasingly-precise measurement techniques, such as GNSS (Global Navigation Satellite System), to high and very high resolution satellite images and in the development of particularly efficient devices for coastal topography assessment. The most common methods currently used for the identification of the shoreline include:

- **Traditional topographical surveys (levelling, surveys with total stations) and GNSS** (Carli et al., 2004; Harley et al., 2011; Morton et al., 1993): these allow high precision measurements in individual points, without any possibility to repeat the survey. They are intensive and time-consuming and it is not always possible to have the access to the area to be detected;
- **Video systems** (Carli et al., 2004; Harley et al., 2011): the technique is used mainly with a network of fixed terrestrial cameras (e.g., ARGUS (Holman and Stanley, 2007) and Siren) from a few units up to

tens, installed at prominent points in the landscape or on specially-positioned supports. They acquire at intervals of up to 10 Hz, encompassing 180° views and allowing total coverage of about 46 km of beach. The acquired images are oblique and require orthorectification operations, as well as georeferencing with algorithms derived from classical photogrammetry. They reach a good accuracy but they cover a local area;

- **Aerophotogrammetric/UAV survey** (Gonçalves and Henriques, 2015; Lee et al., 2009; Mills et al., 2005; Moore, 2000; Papakonstantinou et al., 2016; Paravolidakis et al., 2016, 2018; Stockdonf et al., 2002; Turner et al., 2016): this does not provide a detailed relief, but represents the entire study area at the time of acquisition. Achievable precisions are at the centimetre-subcentimetre level, but the costs are high. Ad hoc flights must be planned, and above all, it is significantly influenced by weather conditions (sunny and minimal wind conditions are needed); this leads to limitations on flight seasons;
- **Satellite remote sensing** (Di et al., 2003; Dominici et al., 2006): This refers to the latest-generation remote sensing satellites, which are becoming more effective as compared to those available previously. Traditionally, medium resolution satellites (e.g., Landsat) have been used advantageously for coastline studies that did not require very high accuracy. Satellites with high and very high resolution are required because they are particularly advantageous compared to traditional photogrammetric aerial acquisitions. High spatial resolution remote sensing satellites allow data to be acquired and processed more quickly, with comparable precision, while offering a very high level of detail. Furthermore, the fundamental ability to capture the scene in several spectral bands allows more information to be extracted than is extractable from images covering only the visible part of the electromagnetic spectrum and thus allows thematic maps of the territory to be created through multispectral classification. Moreover, a new generation of high resolution satellite radar images (SAR, Synthetic Aperture Radar) are becoming even more effective. They operate

---

in the microwave field of the electromagnetic spectrum, allowing the survey during day or night and in every weather condition. The topic is discussed in detail in Chapter 2. Another advantage, which makes this technique more attractive than the others, is that satellite revisit times are very short (a few days), which allows the area to be studied on images taken at different times.

As mentioned above, there is no single method for modeling shoreline but, in the recent years, mapping technology showed a great development. From the literature, it is clear that the use of satellite images is the most diffused for the coastal environment by now. There are a lot of satellites whose sensors produce images suitable for coastal science, using automated or semi-automated image processing techniques to extract the shoreline position. They present many advantages compared to the others:

- they are time-saving,
- they are always available in relative short periods of time,
- there is no need to go physically to the place under investigation,
- they do not need “ad hoc” flight,
- the newest sensors can reach very high resolutions,
- the costs are relatively limited.

To conclude, it is important to reach a good compromise between accuracy, costs and time to find the better methods for shoreline extraction. In most of the studies, the techniques are not used alone but in synergy with others.

#### **1.4.1 Remote sensing techniques for shoreline detection**

Man has always wished to explore, to know and to represent the places and the environments where he lives. From the beginnings, he tried to trace itineraries or paths to get food and nowadays all the information about territory derives from physic observations. In this regard, remote sensing occupies an important role for scientific community. The possibility to

detect Earth from above is tangible thanks to the developments in aerospace technologies, photography, optics, electronics fields. They allowed to extend the study beyond the visible, offering to the man new instruments for Earth Observation (EO). The extension of the perception of the world, both by new observation positions and by the use of new fields of the electromagnetic radiations, introduced a new way to survey events not directly accessible or not easily identified. This type of investigation is called “Remote Sensing”, that is “the acquiring of information from a distance” (NASA, 2020).

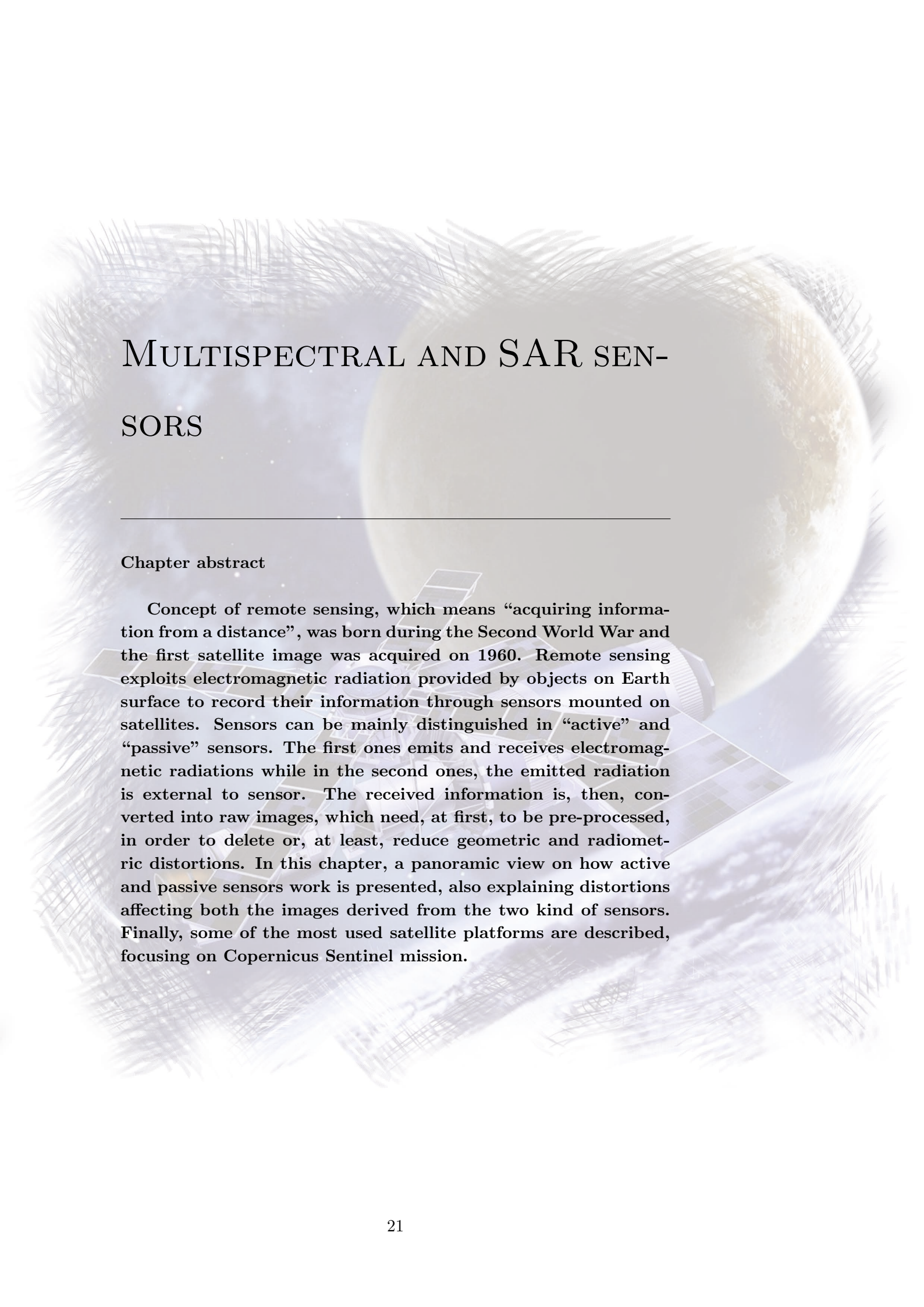
There are many remote sensing techniques that are commonly used to detect shorelines. Traditionally, they have been extracted using photogrammetric technique. With the development of satellites sensors in the optical and microwave part of the electromagnetic spectrum, remote sensing turns out to be a powerful technique for this kind of applications. The accuracies of the different techniques are directly related to their spatial resolution. “While the vertical accuracy might vary considerably, the horizontal accuracy, which actually determines the location of the shoreline, is typically of the same order of magnitude as the spatial resolution of its source data” (Gens, 2010). Especially satellite remote sensing, thanks to the last generation of sensors mounted on satellites, proved to be really effective for shoreline mapping. Until 2000, pixel resolution was too low to detect most of the changes in the shoreline within the timescale required for coastal management (Braga et al., 2013). For example, Landsat images have 30 metres of spatial resolution, so they are suitable only for medium or long-term morphological changes in very dynamic coastal areas. Despite of this, various researchers analysed Landsat data to provide information, especially since the USGS (United States Geological Survey) announced in 2008 that the images would be freely available. Ouma and Tateishi (2006) present an approach for true lake edge information extraction and change detection from Landsat TM/ETM+ (Thematic Mapper/Enhanced Thematic Mapper plus) data series. They studied five of the lakes within the East African Rift Valley. The dataset was integrated with DGPS (Differential Global Positioning System) observations. They demonstrate that in the case of fast mapping of changes in lakes, a combination of Tasseled Cap Wetness (TCW) and Normalised Difference Water Index (NDWI),

---

can be applied to multi-date data such as 30 m spatial resolution Landsat 7 ETM+ and Landsat 5 TM, achieving an accuracy of 98.4%, which was 22.33% higher than the TCW results, and 43.19% more accurate than the NDWI results. Bagli et al. (2004) present a new methodology for the automatic extraction of shoreline and lake boundaries, using morphological image segmentation techniques. The algorithms have been implemented in GIS and the results demonstrates that the coastline extracted automatically is better than available datasets. Pardo-Pascual et al. (2018) evaluates the accuracy of shoreline positions obtained from the infrared (IR) bands of Landsat 7, Landsat 8, and Sentinel-2 imagery on natural beaches. They found a mean horizontal error around 5m for Landsat 7 and around 3m for Landsat 8 and Sentinel-2 shorelines. Gonçalves et al. (2015) propose an approach to derive a tide-coordinate shoreline from two extracted instantaneous shorelines corresponding to a nearly low tide and high tide events. The results have shown that an automatic tide-coordinated extraction method can be efficiently implemented using Landsat 8 and open source software (QGIS and Orfeo toolbox) and python scripting for task automation and software integration.

Since 2000, the new generation of high (for example, Sentinel-1 and Sentinel-2) and very high resolution satellite images (like WorldView, GeoEye, COSMO-SkyMed) has given accuracy comparable with aerial photographs, allowing a rapid spread of their use for a wide variety of purposes. Many studies have been conducted both on optical/multispectral and on radar images. Braga et al. (2013) extract the instantaneous shoreline from remote sensing data acquired with very high resolution multispectral and SAR sensors, in particular IKONOS, GeoEye and COSMO-SkyMed. The study area was a sandy beach in Venice (Italy) and the results have been validated using GPS measurement. The extracted shorelines show very good accuracies: 1-2 pixels for multispectral images (whose resolution is 0.5 – 4m) and 1 pixel for COSMO-SkyMed (whose resolution is 3m). Palazzo et al. (2012), as part of COSMOCOast project, analysed COSMO-SkyMed images to extract the shoreline. They found that this sensor, recording X-band data, appears to be more sensitive to small-scale waves during windy weather. In addition, they found that HH polarization

is better than VV. Pradhan et al. (2018) detect shoreline changes using two synthetic aperture radar RADARSAT images for the state of Kelantan, Malaysia. The results achieved 98% accuracy and they were validated using a thematic map. The change detection showed an average difference in the shoreline of 12.5m. Rishikeshan and Ramesh (2017) present a flexible mathematical morphology-driven approach for shoreline extraction. The data-sets consist of very high-resolution panchromatic data of 0.8 metre (Cartosat), moderate resolution Resource sat-2 LISS IV 5.8 metre data, and low-resolution Landsat ETM+ 30 metre data. The proposed algorithm extracts shorelines with a better accuracy of 99.91% compared to the accuracy obtained by existing methods. Sekovski et al. (2014) used a semi-automatic approach in delineating a proxy-based shoreline by processing high-resolution multispectral WorldView-2 satellite imagery. WorldView-2 images are really suitable for the purpose, because of their spatial resolution of 50cm (panchromatic) and 2m (multispectral) for civilian (Kramer, 2002a,b). The results showed that the average distance between reference shorelines and those resulting from classification methods was less than 5.6m (Maximum likelihood), whereas a valuable distance of just 2.2m was detected from ISODATA and Mahalanobis. The case study was carried out on coastal area of the Ravenna Municipality. In this area, a frequent monitoring of shoreline position is required because of the “extreme vulnerability to erosion phenomena that have resulted in a general trend of coastal retreat over recent decades”. The same problem affects the area of Ortona’s coast (center of Italy), that is part of Adriatic Sea as well as Castelldefels sea (Barcelona, Spain). These are the two areas taken into account for the present research. They are both part of Mediterranean Sea, so the conditions (tides, waves, weather) could be considered the same. As presented in the case study chapters (chapters 4 and 5), they are sandy coast, subject to slow changes during time. The changes are the response to a complex relationship between tidal currents and wave energy, sediment fluvial discharge and long-shore currents, eustacy and land subsidence, and the effects of human interventions (Braga et al., 2013).

The background of the page features a satellite in orbit over Earth, with a large, bright moon in the upper right corner. The satellite is shown from a perspective that highlights its solar panels and various instruments. The Earth's surface is visible below, showing cloud patterns and landmasses. The overall scene is set against a dark, starry space background.

# MULTISPECTRAL AND SAR SENSORS

---

## Chapter abstract

Concept of remote sensing, which means “acquiring information from a distance”, was born during the Second World War and the first satellite image was acquired on 1960. Remote sensing exploits electromagnetic radiation provided by objects on Earth surface to record their information through sensors mounted on satellites. Sensors can be mainly distinguished in “active” and “passive” sensors. The first ones emits and receives electromagnetic radiations while in the second ones, the emitted radiation is external to sensor. The received information is, then, converted into raw images, which need, at first, to be pre-processed, in order to delete or, at least, reduce geometric and radiometric distortions. In this chapter, a panoramic view on how active and passive sensors work is presented, also explaining distortions affecting both the images derived from the two kind of sensors. Finally, some of the most used satellite platforms are described, focusing on Copernicus Sentinel mission.

## 2.1 Introduction

Man has always tried to explore Earth from above, in order to have a wider vision of the phenomenon he wanted to detect. “Remote Sensing” means “acquiring of information from a distance” (Gomasasca, 2009; NASA, 2020). Remote Sensing was born during the Second World War, following the technological development. The first images from satellite are dated on 1960, thanks to meteorological satellite TIROS-1. “Remote Sensing is the scientific subject which help to obtain information, qualitative and quantitative, about distant objects and about the surrounding” (Brivio et al., 2006).

Electromagnetic radiation, interacting with objects on Earth, represents the transport vehicle of surfaces information (Dermanis and Biagi, 2002). Their acquisition by means of remote sensing is developed into four phases (Gomasasca, 2009), as shown in figure 2.1:

1. data collection from satellite acquisition stations;
2. pre-processing of the collected data;
3. processing of the collected data;
4. data interpretation and information extraction.

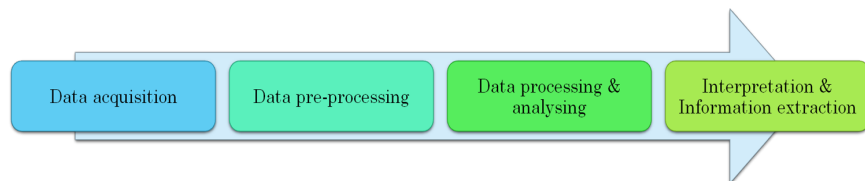


**Figure 2.1.** Remote Sensing workflow

Using satellite sensors, it is possible to derive satellite images. Satellite remote sensing is going to have a promising future in a low cost acquisition of high and very high-resolution data. Many countries, like Russia, USA, China, India, Japan, Europe, have been contributing to launch multiple satellite to explore Earth from space.

Firstly, satellites can be classified by their orbital geometry, timing and altitude.

---

Three types of orbits are typically used in remote sensing satellites, such as geostationary, equatorial, and sun-synchronous orbits. A geostationary satellite has a period of rotation equal to that of Earth (24 hours) so the satellite is positioned always over the same place on Earth. In an equatorial orbit, a satellite circles the Earth at a low inclination (the angle between the orbital plane and the equatorial plane). Sun-synchronous satellites have orbits with high inclination angles, passing nearly over the poles. Orbit time is defined so that satellite always passes over the equator at the same local sun time. In this way, these satellites maintain the same relative position with the sun for all of its orbits. Many satellites for remote sensing have the sun-synchronous orbit, in order to have the same sun's conditions.

About the timing, one of the main characteristic of satellite platforms is the revisit time, that is the frequency at which a satellite sensor can acquire data of the same place. It is different from sensor to sensor: it could be from twice a day to every 16 days.

About altitude, common remote sensing satellites typically has orbits which range from 600 to 1000 km (Zhu et al., 2017).

Secondly, sensors mounted on satellites are divided into two main types: active and passive (Fig. 2.2).

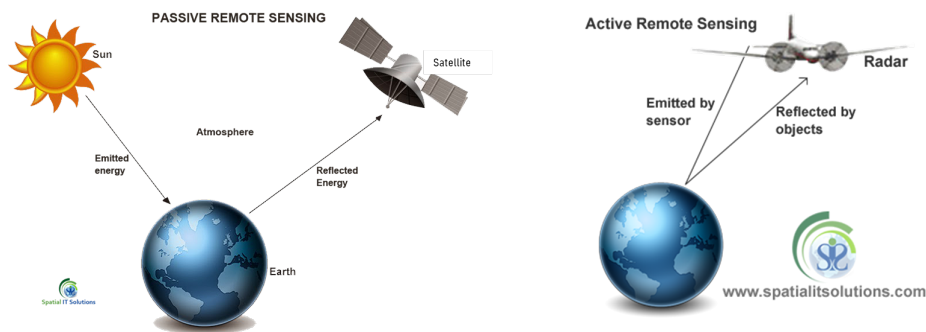


**Figure 2.2.** Passive and active remote sensors (Spatial Solutions, nd)

Passive sensors record the intensity of the reflected electromagnetic energy coming from the Sun or emitted by the Earth. They typically record the wavelengths which correspond to the range of visible and near-infrared (NIR) light. These kinds of sensors are generally called “optical” sensors. The measured power is function of the surface composition, physical temperature, surface roughness and other physical characteristics of the Earth. Among the optical sensors, some of the most used are Landsat, Sentinel-2,

SPOT, EROS, GeoEye and WorldView satellites.

Active sensors emit radiation themselves, collecting the back signal (called *backscattering*); the radiation is backscattered to the sensor with intensity depending on the structural characteristics of the examined surface and on the wavelength ( $\lambda$ ) of the incident energy (Gomarasca, 2009). They typically record in the range of radar waves (radio and microwave). They are typically called “radar sensors”. In figure 2.3, a scheme about optical and radar sensors with their wavelength range is shown.

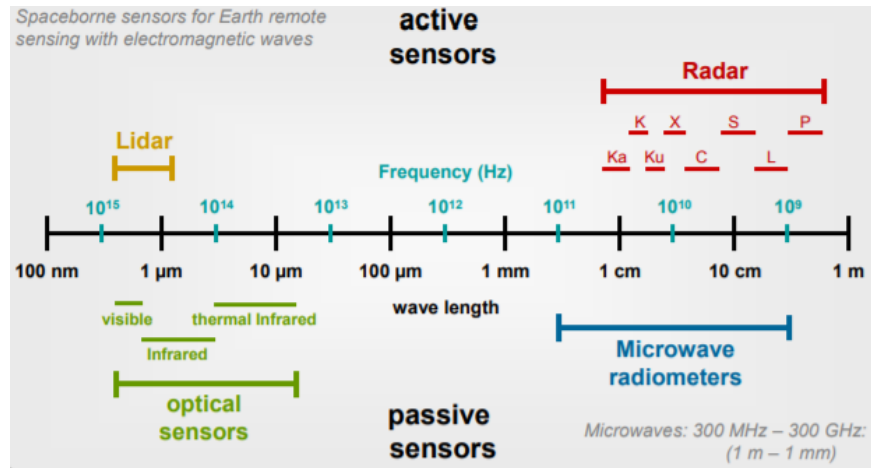


**Figure 2.3.** Scheme about optical and radar sensors with their typical wavelengths ranges (Moreira, 2013)

SAR is the acronym of Synthetic Aperture Radar and it is an example of active system. It is a RADAR (RADio Detection And Ranging) system, capable of acquiring information about the range, angle or velocity of targets using radio or microwaves. Its physics is based on electromagnetic radiation, which is produced by a transmitting antenna, and on the backscatter phenomenon. The radiation is collected by a receiving antenna.

Once the data (optical or radar images in this case) are collected, they are pre-processed and processed in order to extract useful information. In this chapter, a short presentation about optical and SAR systems characteristics and the main differences between them are discussed. Then, some satellite platforms are presented, in particular, Sentinel-2 and WorldView-2 among the passive sensors and Sentinel-1 and COSMO-SkyMed among the active sensors.

---

## 2.2 About resolutions

The term “resolution” is the description of the detected scene in terms of “how many details can the sensor find”. The resolution of remote sensed data can be characterised in several different ways. There are four types of “resolutions” (Humboldt State University, 2019c):

- spatial (or geometric) resolution;
- spectral resolution;
- radiometric resolution;
- temporal resolution.

Spatial resolution is referred to the dimensions of the detected objects in a scene and describes the minimum distance needed to consider distinct two objects (Brivio et al., 2006). It describes how many details are visible to the human eye in an image. In general, it is expressed in metres.

Spectral resolution refers to how many spectral bands an instrument can record. In remote sensing, survey can be conducted simultaneously on different portions (bands or channels) of the electromagnetic spectrum, so that an object can be better recognised. Spectral resolution is also defined by how wide each band is or the range of wavelengths covered by a single band. In other words, it expresses the ability to distinguish two consecutive wavelengths.

Radiometric resolution is how finely a satellite or sensor divides up the radiance it receives in each band. The greater the radiometric resolution the greater the range of intensities of radiation the sensor is able to distinguish and record. In other words, it represents the number of grey level used in an image.

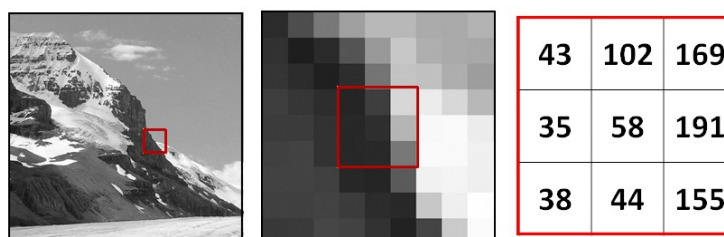
Temporal resolution expresses the amount of time (e.g. days) that passes between imagery collection periods for a given surface location. This resolution is really important to check the dynamics of natural phenomena (change detection).

The recognisability of objects is the main purpose of remote sensing techniques and it could be achieved imposing some boundary conditions.

One of them (and the most used) is the contrast. Distinction between two different object and, of course, measurements of their dimension, are strictly related to their radiometric contrast. It is defined as the ratio between the lightest and the darkest part in a scene, that is the ratio between maximum and minimum irradiance (Brivio et al., 2006).

## 2.3 Passive sensors: optical images

Optical remote sensing makes use of visible and near infrared sensors to form images of the Earth's surface. The source of energy is generally the sun, as it falls within passive remote sensing technique. Target on the ground responds with another energy (electromagnetic radiation) which reaches the sensor on the satellite. Then the image is formed. Image formation technique refers to how the system actually produces an image. Acquisition process of digital image is different from analogical one. It is well known that in traditional photographic systems (it is no longer true for digital cameras) the energy reflected by the surfaces of the framed scene is impressed on a film sensitive to electromagnetic radiation in a determined interval of the electromagnetic spectrum. In the case of optical-electronic devices, this physical recording surface does not exist, but its function is performed by coupling the sensitive area of the detector with a recording system of output electrical signal. These devices are like a black box which works on entrance signal (radiant flow) to produce output signal (number): it is fully characterised once its transfer function is known (Brivio et al., 2006). So, the signal is converted in a number called "Digital Number" (DN): the image is composed by small and squared elements, called pixels (Fig. 2.4).



---

**Figure 2.4.** How an image is formed (Mishra, 2019)

---

Pixels have the same shape and area and they are organized in rows and columns (Gomasasca, 2009).

The mathematical model that describes a digital image is an array of  $R$  rows and  $C$  columns, containing  $N = R \times C$  elements, i.e. pixels (Fig. 2.5). Every pixel is characterised by three values  $(x, y, L)$  where  $x$  and  $y$  are, respectively, row and column index (they determine pixel position in the image) and  $L$  is the number related to the measured radiance value, so it represents the brightness (or grey level). The origin of the axes in an image is on the top left side and the  $y$  axis is oriented on the opposite side with respect to the conventional Cartesian plane (Brivio et al., 2006).

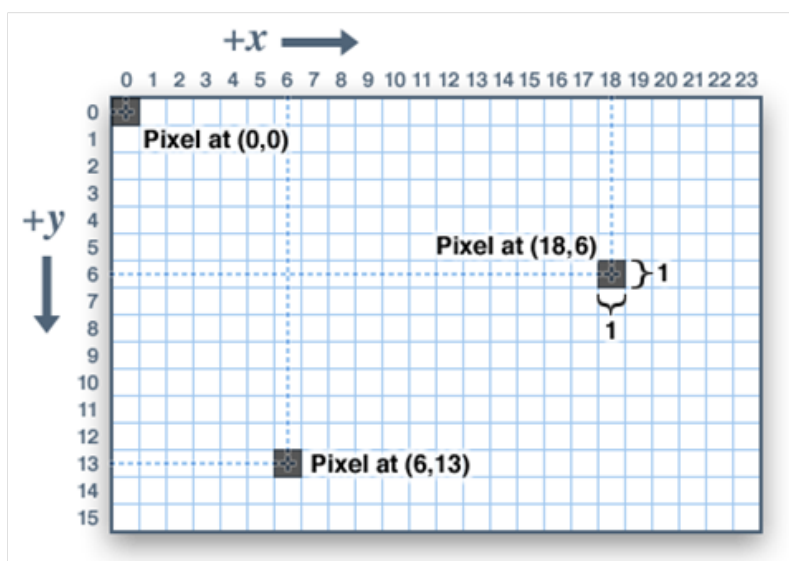


**Figure 2.5.** Structure of image arranged in pixels (Young, 2020)

Then the image needs to be stored on the computer. The analogical signals are transformed into numerical values in function of the established sampling frequency. The signal changes from continuous to discrete. This discretization defines the radiometric depth of the pixel (that is the radiometric resolution). The radiometric resolution indicates the number of bit associated to each pixel of the image and defines the chromatic or tonal scale (Gomasasca, 2009). The elementary unit of information, called bit (binary digit), is composed of two digits 0 and 1, corresponding to the possible states:

- on: 1
- off: 0

A numerical datum can be represented by an ordinate series of bit. The possible numerical combinations in 2-bit image are four: 00, 01, 10, 11. For every further bit, the number of combinations is raised to the square ( $2^k$ , where  $k$  is the number of bit); in 4-bit image, the possible combinations rise to 16 ( $2^4$ ), in 8-bit combination to 256 ( $2^8$ ), and so on. The definition range is between 0 and  $2^k - 1$ ; for example, in the case of 8-bit storage, integer values are  $2^8 = 256$ , starting from 0 (black) to 255 (white), stored respectively as 00000000 and 11111111. So, a digital image is always monochrome. How can a coloured image be obtained? By combining multiple layers, that are called bands. Image bands (also called channels or layers) are a collection of images taken simultaneously of the same place.

Optical remote sensing systems are classified into four types, depending on the number of spectral bands used in the imaging process (CRISP, 2001):

- **Panchromatic imaging system:** the sensor is composed by a single channel which acquires a wide range of wavelengths. If the range is the visible part of the electromagnetic spectrum, the image is grey-scale. Spectral information are lost and the intensity of the target energy response determines the brightness of the pixels in the image;
- **Multispectral imaging system:** the sensor is multichannel and can acquire few spectral bands (in general less than 10). Spectral bands take into account many wavelengths, but considering a narrow range. The resulting images are multilayer and contain both the spectral and the brightness information of the target;
- **Superspectral imaging system:** it is similar to multispectral imaging system, but it considers a narrower bandwidths and the spectral bands are in general more than 10. Spectral and brightness information are more precise than multispectral ones;
- **Hyperspectral imaging system:** similar to the last ones, it can acquire more than 100 contiguous spectral bands (for example PRISMA sensor can acquire almost 240 bands (ESA, European Space Agency, 2020a)), determining more precise information about spectral and brightness characteristics.

---

In this research, the presented case studies take into account panchromatic and multispectral imaging system, so they are explained in detail.

### 2.3.1 Multispectral sensors

Multispectral sensors simultaneously measure data in multiple regions of the electromagnetic spectrum, as explained in section 2.3. The range of wavelength measured by a sensor is called “band” and it is commonly described by the name (Red or NIR (Near InfraRed), for example) and the wavelength of recorded energy (Humboldt State University, 2019b). Human vision is a system that is able to detect three wavelengths or spectral bands. Our brains combine this data detected by our eyes into a single colour image. All of the colours that humans perceive can be created by mixing the three additive primary colours: red, green and blue. This means “3-band” image is needed to display a natural colour image (Fig. 2.6).

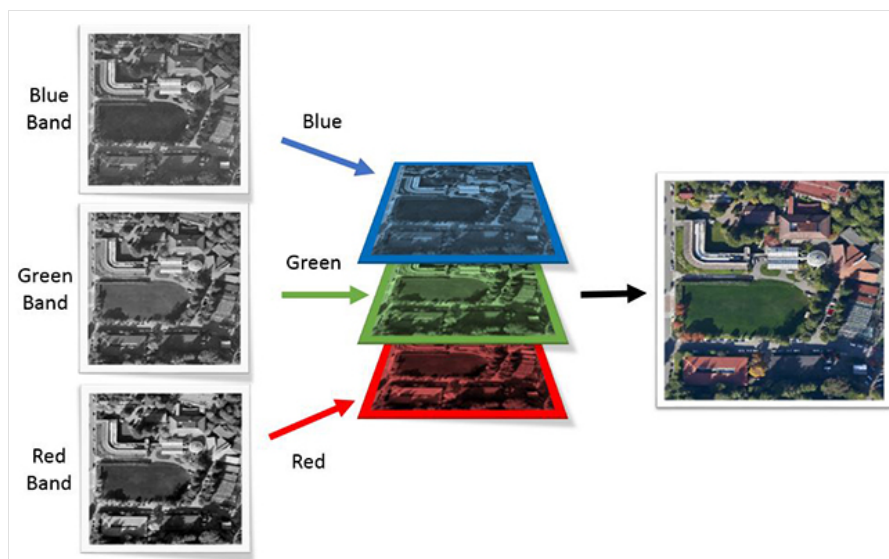


**Figure 2.6.** RGB bands which form the natural colour image (Humboldt State University, 2019b)

Each colour (red, green, blue) is 8-bit, meaning there can be 256 possible colour shades for each of them. Since each colour has 256 shades, 256 for red by 256 for green by 256 for blue can be multiplied to get 16, 777, 216 colours (the same as  $2^{24}$  or 24-bit). The result is a colour image where each pixel colour is determined by a combination of RGB in different brightness. Sensors that simultaneously measure data in multiple regions of the electromagnetic spectrum are known as multispectral sensors (Fig. 2.7).

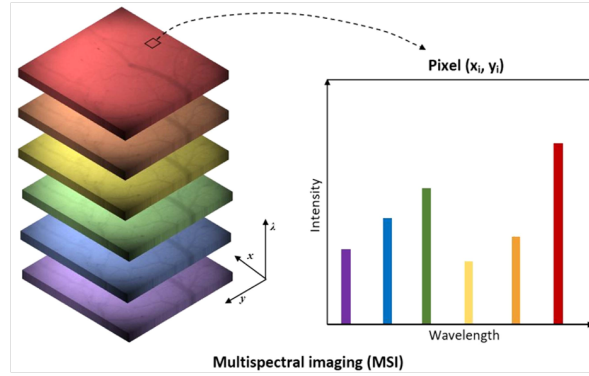


**Figure 2.7.** Example of how a multispectral image is composed (Humboldt State University, 2019b).

Each band of a multispectral image can be displayed at once as a greyscale image, or as a combination of three bands at once as a colour composite image (Humboldt State University, 2019a).

### 2.3.2 Geometric distortion in optical images

Satellite images are affected by geometric distortions, because 3D reality is represented in 2D image. Geometric distortions depends on how the data are acquired and they are caused by various factors, like perspective of the sensor optics, motion of the scanning system, motion and (in)stability of the platform, platform altitude, attitude and velocity, terrain relief, curvature and rotation of the Earth (Natural Resources Canada, 2008). Geometric distortions are classified into (Thakkar et al., 2016):

- internal distortions;
- external distortions.

The internal distortions are caused by the geometry of the sensor, while external distortions by the attitude of the sensor or the form of the object. Relief displacement is one of the most common geometric distortion. Objects under the nadir of the camera show their top visible but the objects not directly under the nadir show also their sides (Fig. 2.8). The more the objects are tall and far from the nadir, the they more will be the influence of this geometric distortion.

Another common geometric distortion, especially in satellite images, is called *skew distortion*. This is caused by variations in platform stability, like

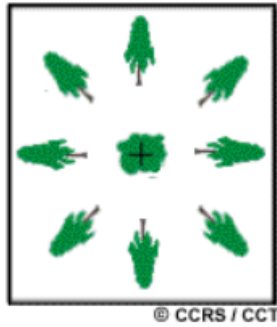


**Figure 2.8.** First example of geometric distortion: objects far from the center of the image along the nadir show not only their tops visible but also their side parts (Natural Resources Canada, 2008)

changes in speed, altitude, and attitude (angular orientation with respect to the ground) during the acquisition. Moreover, Earth rotation creates this distortion because the first part of the image is taken from a specific position but the last part of it is a bit moved to the west. So the final image is skewed across the image (Natural Resources Canada, 2008). A summary of geometric distortions, represented in figure 2.9, can be found in Dave et al. (2015).

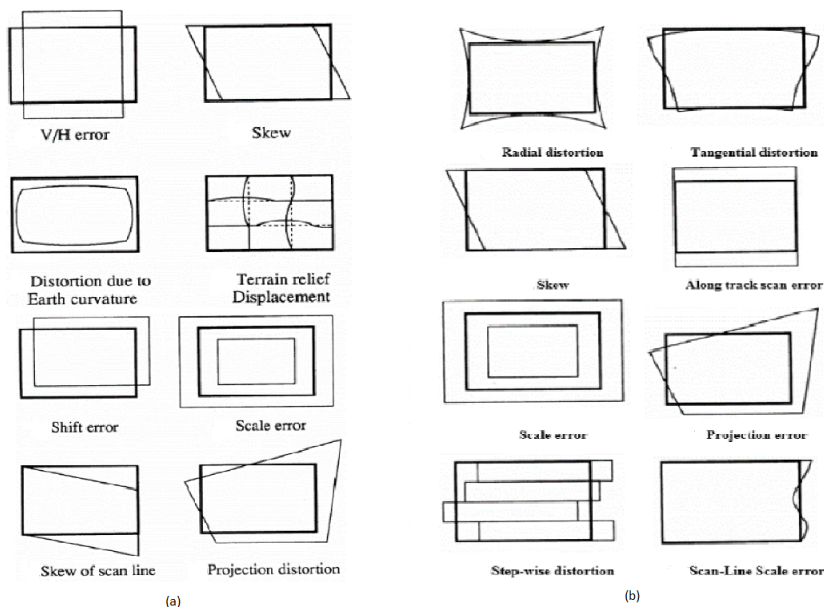


**Figure 2.9.** External (a) and internal (b) distortions in optical satellite images (Dave et al., 2015).

Before start image processing, these errors need to be corrected, using pre-processing techniques, like orthorectification and georeferencing.

### 2.3.3 Radiometric distortion in optical images

Sun radiation that illuminates objects is perturbed by its passage through the atmosphere and does not hit all objects at the same angle. Moreover, the travel from target to sensor also crosses the atmosphere, so the radiation is perturbed again. In addition, gases and dust can absorb and/or reflect specific wavelengths (Belgian Earth Observation, nd). Radiometric distortions happen, then, because of many factors, like sun's azimuth and elevation, atmospheric conditions (fog, aerosol...), sensor's response. These factors change the received energy from targets original value, changing the radiation spectral properties. In order to obtain the real irradiance or reflectance, those radiometric distortions must be corrected, using pre-processing techniques, like resampling (Japan Association of Remote Sensing, 1996).

## 2.4 Active sensors: SAR images

A Synthetic Aperture Radar (SAR) is “a coherent side - looking radar system which utilizes the flight path of a platform to simulate an extremely large antenna or aperture electronically, and that generates high-resolution remote sensing imagery” (Wolff, ndb). It provides high-resolution, day-and-night and weather-independent images (Moreira et al., 2013) because it is a coherent and active system which works in the microwaves field of the electromagnetic spectrum. “Active” because it can produce by itself the radiation energy to “illuminate” the scene to be detected; “coherent” because it acquires both amplitude (module value) and phase (which provides the distance of an object) information of the signal; “microwave” because it works on the microwave region of the electromagnetic spectrum and so it can provide day/night information in any weather conditions. SAR is typically mounted on a moving platform, such as an aircraft or spacecraft.

It is and it works like RADAR, RAdio Detecting And Ranging. It refers to electronic equipment that detects the presence of objects by using reflected electromagnetic energy. Radar system can measure the direction, height, distance, course, and speed of these objects. One of the most important function is the calculation of the range by measuring the de-

lay time (Wolff, nda). An electromagnetic pulse transmitted by the radar travels at the speed of light towards a target that reflects back the signal. The distance  $d$  between radar sensor and target can be calculated by dividing time  $t$  by two, and multiplying it by speed of light in a vacuum  $c = 299,792,458m/s$  (eq. 2.1) (SensorsONE, 2020):

$$d = \frac{c \cdot t}{2} \quad (2.1)$$

The width of a receiving antenna beam determines the azimuth resolution of a radar image, but, in order to have meter resolution, it would be necessary to use an antenna of kilometric size, which is, obviously, impossible. The idea behind SAR allows to overcome this limitation, reaching a compromise between the resolution and the extension of the observed area. The term “Synthetic Aperture Radar” refers to a technique used to “synthesize” an antenna of kilometric size by combining radar echoes received from a real antenna to different positions. When a impulse starts from SAR sensor, after a certain distance it hits a target, which respond with a backscatter. In the meantime, when SAR sensor receives again the backscatter, it moves in another position, creating the so-called “aperture” (the size of the antenna, figure 2.10). Typically, the larger the aperture, the higher the image resolution will be (Moreira et al., 2013).

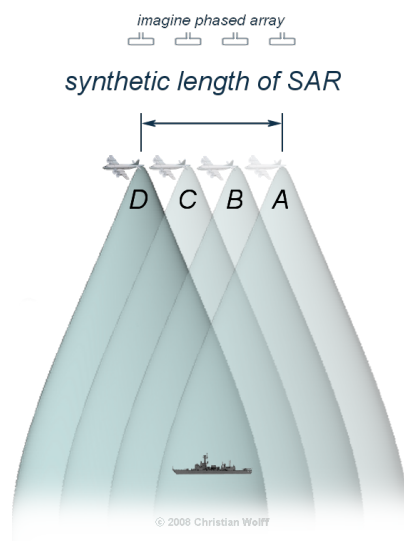


**Figure 2.10.** How a synthetic aperture radar works: the synthesized expanding beamwidth (Wolff, 2008)

### 2.4.1 SAR geometry

The elementary surface, that defines the geometric resolution in a RADAR image, will be constituted by the combination of resolution along the azimuth and the ground range.

To explain SAR images resolutions, in figure 2.11 a typical SAR geometry is shown.

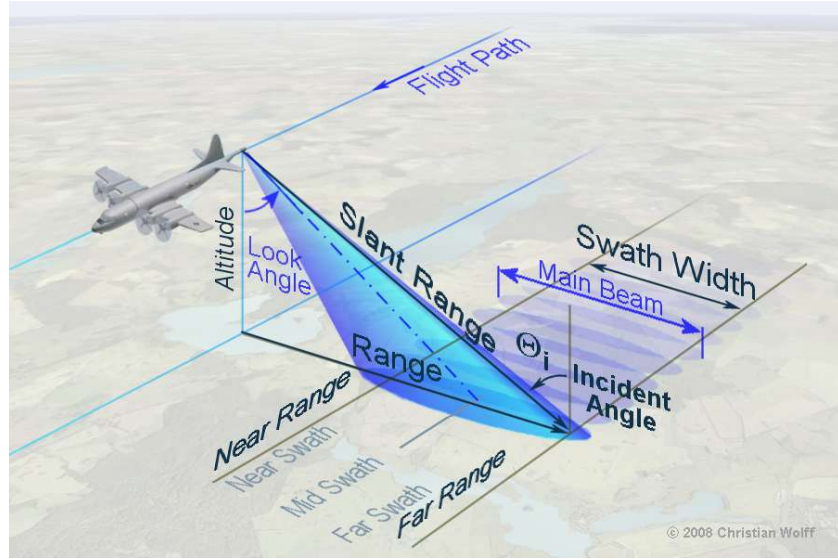


**Figure 2.11.** Imaging geometry for a synthetic aperture radar imaging system. (Sherifview, 2010)

The platform (aircraft or satellite, for example) of a side-looking SAR travels forward in flight direction (called “azimuth”) with nadir directly beneath the platform. Microwave beam is transmitted obliquely at right angles to the direction of flight, illuminating the so-called “swath”. Range refers to the across-track dimension perpendicular to flight direction, while azimuth refers to along-track dimension parallel to flight direction. Swath width refers to the width of the imaged scene in range dimension. Longitudinal extent of swath is defined by motion of the aircraft with respect to the surface, whereas swath width is measured perpendicularly to longitudinal extent of the swath (Sherifview, 2010). Distance between sensor and target is called “slant range” and its projection on the ground is called “ground range”. The part of the image closest to the sensor is called “near range”; on the contrary, the further part is called “far range”. The look angle is called “off-nadir angle” and it is the angle between the slant range direc-

---

tion and the vertical. It is different from the local incident angle  $\Theta_i$ , which depends on the ground slope. Therefore, SAR is a side-looking system. Unlike optical instruments, which can assume a nadir-looking framework because they are able to distinguish targets based on their angular distance from the sensor nadir, RADAR system can distinguish two different targets only considering their backscatters. A nadiral acquisition would not be able to distinguish between two targets at the same distance from the sensor, because a single front incident wave illuminates both points at the same time. Consequently the backscatters from both points arrive at the receiving antenna at the same time (De Agostini and Floris, 2014). This causes left/right ambiguity for all points symmetric with respect to nadir. This is the reason why SAR system needs a side-looking framework: the backscatters come back to the receiving antenna in different times.

#### 2.4.2 SAR images resolution

It is clear from the subsection 2.4.1 that SAR images are “composed” by two main kind of spatial resolutions: range and azimuth resolutions. Range resolution is defined as “the ability of the system to distinguish between two different targets on the ground” while azimuth resolution as “the minimum distance on the ground in the direction parallel to the flight path of the aircraft at which two targets can be separately imaged” (Chan and Koo, 2008). In other words, they can be distinguished when they are not within the radar beam at the same time. Resolution along the slant range  $r_{ss}$  is given by equation 2.1, so its projection on the ground determines the ground range resolution (eq. 2.2):

$$r_{sg} = \frac{c \cdot t}{2 \cdot \sin\theta} \quad (2.2)$$

where  $c = 299,792,458m/s$  is the speed of light in a vacuum,  $t$  is the time taken to travel over the sent-resent distance (that is why it is divided by 2) and  $\theta$  is the incidence angle.

On the other hand, azimuth resolution  $r_{sa}$  is given by (eq. 2.3):

$$r_{sa} = \beta \cdot R_0 \quad (2.3)$$

where  $\beta = \frac{\lambda}{L}$ ,  $L$  is the length of the radar antenna in azimuth,  $\beta$  the radar beam width,  $\lambda$  the wavelength and  $R_0$  the satellite-target distance. The azimuth resolution depends on aperture length.

Both resolutions are displayed in figure 2.12:

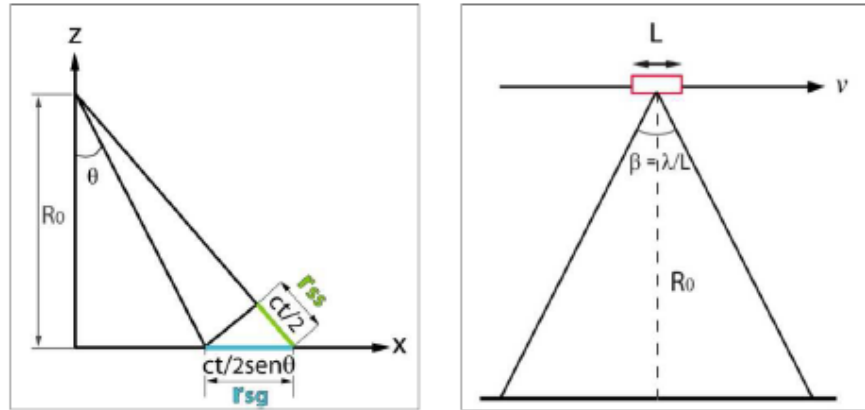


**Figure 2.12.** SAR range (on the left) and azimuth (on the right) resolutions (De Agostini and Floris, 2014)

Azimuth resolution is proportional to the altitude and inversely proportional to the length of the radar antenna. So, the bigger is length  $L$  of the antenna, the smaller is  $\beta$ , the higher will be the azimuth spatial resolution. As explained at the beginning of the present section, in order to have a metre resolution, an antenna of kilometric size would be necessary. That is why SAR system represent a good compromise between length of the antenna and high resolution data.

On the other hand, radiometric resolution is the minimum signal variation acquired by radar and it determines how fine a sensor can distinguish between objects with similar reflection properties. It is an important parameter to define the quality of the radar scene reconstructed from the backscattered returns and it is useful for those application like polarimetry and classification (Márquez-Martínez et al., 2004).

SAR images, as well as optical images, are affected by many distortions that must be corrected. In the following subsections, the main SAR distortions are presented.

### 2.4.3 Geometric Distortions

The acquisition mode (side-looking) of SAR system produces three geometric distortions (Fig. 2.13), in particular perspective deformations due to terrain topography.

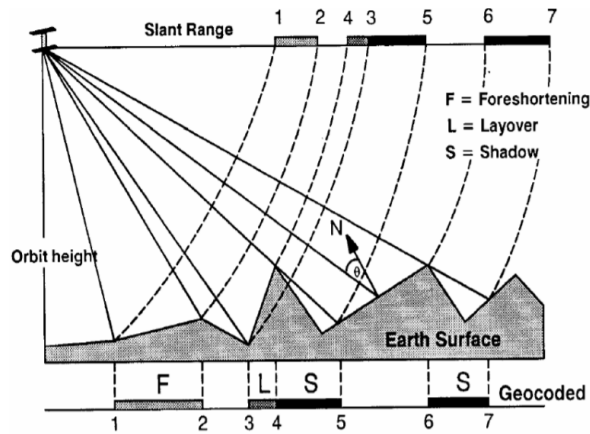


Figure 2.13. SAR geometric distortions (Veci, 2019)

They are hereafter described (Brown, 2020; Pour and Hashim, 2014; Veci, 2019):

- shadowing: an object blocks the path of radar beam and that part corresponds to black colour (like blind spots) in the image, i.e. there is no information in a SAR shadow because there is no return signal;
- foreshortening: it happens because the backscattered returns are arranged in the image based on how far the target is from the antenna along the slant plane (also called LOS, Line Of Sight). The period of time that a slope is illuminated by the transmitted pulse of the radar energy determines the length of the slope on radar imagery. The effect is to compress the image of affected areas, which appear shorter than how it really is in range direction. Resolution cells size is also increased and hence these areas usually appear whiter on amplitude image. It happens in all cases except when the local angle of incidence is equal to  $90^\circ$ ;
- layover: it is an extreme example of foreshortening. The object is so tall that the radar signal reaches higher points before than lower points. This causes the returns from higher points to be placed on the

image closer to the sensor (near range) and obscure the others, as if the top has been overlaid on the foot of the mountain. The sequence at which the points along the terrain are imaged produces an image that appears inverted. “Radar layover is dependant on the difference in slant range distance between the top and bottom of the feature” (Veci, 2019).

#### 2.4.4 Radiometric distortion: Speckle

Speckle is a typical radar distortion which affects radiometric resolution of the image (Fig. 2.14).

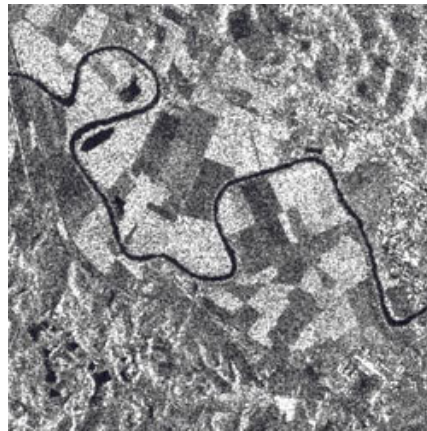


**Figure 2.14.** Speckle effect (ESA, European Space Agency, 2020b)

It is caused by “random constructive and destructive interference resulting in salt and pepper noise throughout the image” (Veci, 2019) and it happens because each resolution cell associated with an extended target contains several scattering centers whose elementary returns, by positive or negative interference, originate light or dark image brightness (ESA, European Space Agency, 2020b). In the image, important grey level variations create a grainy texture, characteristic of radar images. Speckle can be reduced using two methods (ESA, European Space Agency, 2020b):

1. SAR image multi-look processing;
2. filtering techniques.

The first one averages independent measurements of the same target by splitting the synthetic aperture into smaller sub-apertures (called “looks”), each separately processed and then averaged. The grey level variations

---

are reduced by using different looks. This goes to the detriment of spatial resolution, which is reduced. Sometimes it would be more effective using filtering techniques, although the spatial resolution is always reduced but to a lesser extent. They make use of a moving window, which changes the intensity of the central pixel, taking into account the intensities of all the neighbour pixels within the window.

Removing speckle is a great challenge, that is why, in literature, a lot of studies have been conducted on this topic and a lot of algorithms have been implemented to reduce as good as possible speckle distortion (Eichel et al., 1989; Han et al., 2013; Mastriani and Giraldez, 2016; Sivaranjani et al., 2019; Wang et al., 2017; Woo and Yun, 2011; You and Kaveh, 2000). As previously explained, SAR sensors can acquire images in any weather conditions and also in the night. This is true but during a storm or during the night, SAR images are more sensible to speckle distortion, so that the presence of this effect is higher in these situations (Singh and Shree, 2016) and needs to be reduced.

## 2.5 Satellite platforms

In the present section, the main characteristics of some of the most used satellite platforms are presented.

### 2.5.1 Sentinel-1

Sentinel-1 is the first mission within Copernicus project, for the initiative of the European Commission (EC) and the European Space Agency (ESA). Copernicus project is based on observation data received from Earth Observation (EO) satellites and ground-based information (ESA, European Space Agency, ndk). It is a SAR system, working in C-band (central frequency of 5.404 GHz), and it is made up of 2 satellites, Sentinel-1A and Sentinel-1B, sharing the same orbital plane. It can be used for many purposes, like ice monitoring (Dammann et al., 2019; Mouginot et al., 2017; Nagler et al., 2015), oil-spill monitoring (Chaturvedi et al., 2019; Konstantinidou et al., 2019; Nezhad et al., 2018), ship detection for maritime security (Cozzolino et al., 2017; Dechesne et al., 2019; Wang et al., 2018), mapping for forest,

water and soil management (Forkuor et al., 2020; Steinhausen et al., 2018; Van Tricht et al., 2018), shoreline extraction (Lubczonek, 2017; Spinosa et al., 2018) and so on.

Sentinel-1 follows sun-synchronous orbit with 12 day repeat cycle. Both Sentinel-1A and Sentinel-1B share the same orbit plane with 180° orbital phasing difference, so, with both satellites operating, repeat cycle, that is revisit time, is 6 days (ESA, European Space Agency, ndf). In figure 2.15, Sentinel-1 observation scenario, considering revisit time and coverage frequency, is shown.

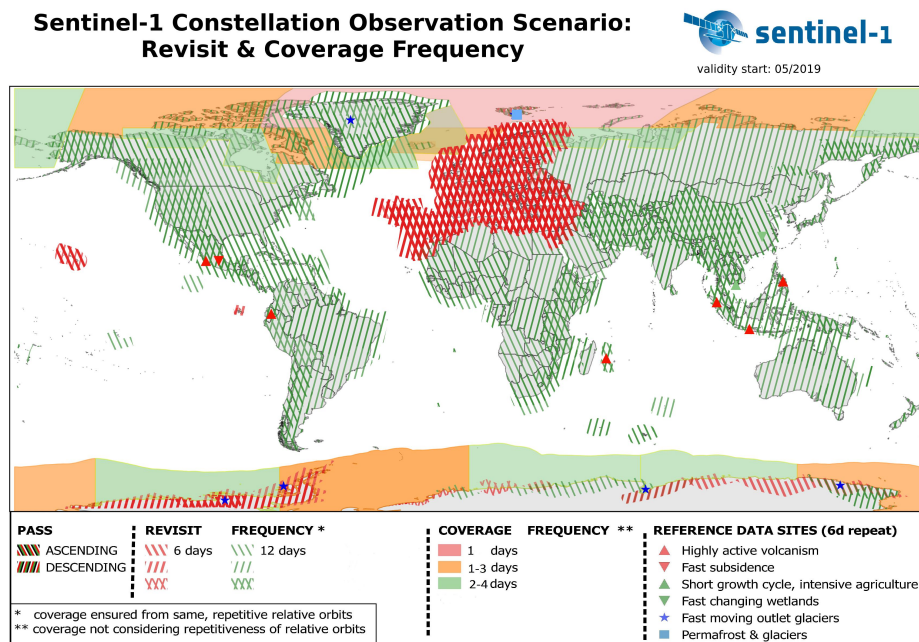


**Figure 2.15.** Sentinel-1 observation scenario all over the world: revisit time and coverage frequency (ESA, European Space Agency, ndl)

One of the greatest advantage of Sentinel-1 images is that they are high-resolution and free of charge. Open and free access data help the utilisation of Sentinel data for the widest range of applications.

Sentinel-1 operates in four acquisition modes (ESA, European Space Agency, ndj):

1. Stripmap (SM);
2. Interferometric Wide swath (IW);
3. Extra-Wide swath (EW);
4. Wave mode (WV).

---

Stripmap mode provides images with a  $5m$  by  $5m$  resolution over a narrow swath width of  $80km$ .

Interferometric Wide swath mode allows combining  $250km$  swath width with a moderate geometric resolution ( $5m$  by  $20m$ ). The IW mode creates three sub-swaths images using Terrain Observation with Progressive Scans SAR (TOPSAR). This mode is used for the majority of applications and it is also used for the present research, as illustrated in case studies (chapters 4 and 5). The image is composed by three sub-swath, each of them composed by many “bursts” (Fig. 2.16). If necessary, they can be merged into pre-processing steps, thanks to the sufficient overlap between each burst and each swath.

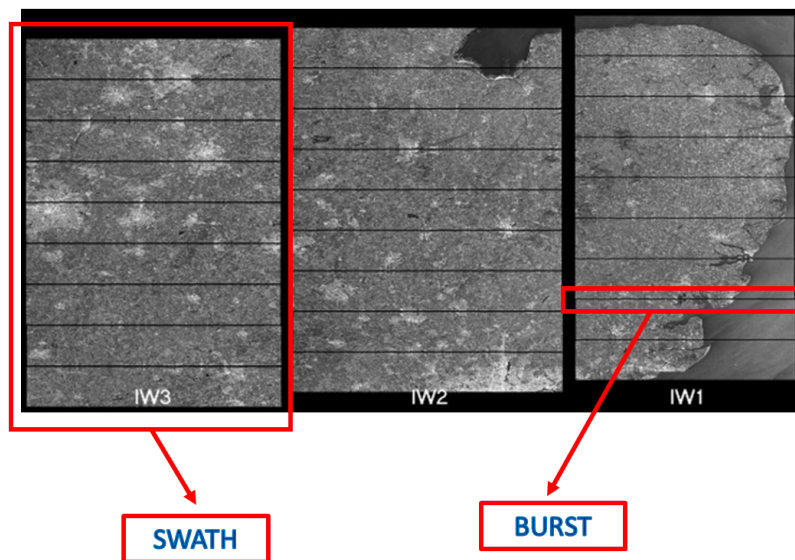


**Figure 2.16.** Sentinel-1 IW acquisition mode: images are formed by three swaths and many bursts (ESA, European Space Agency, ndc)

Extra Wide swath mode is similar to IW mode (using TOPSAR) but it creates five sub-swath instead of three, resulting in a lower resolution ( $20m$  by  $40m$ ). It is generally used for maritime, ice and polar zone applications, because of its wide coverage and short revisit times.

Wave mode provides stripmap “vignettes” of  $20km$  by  $20km$ , acquired alternately on two different incidence angles. Vignettes are acquired every  $100km$ , with vignettes on the same incidence angle separated by  $200km$  (Fig. 2.17).

All Sentinel-1 SAR acquired data are systematically processed to create predefined product types, which are provided into 3 levels: Level 0, Level 1

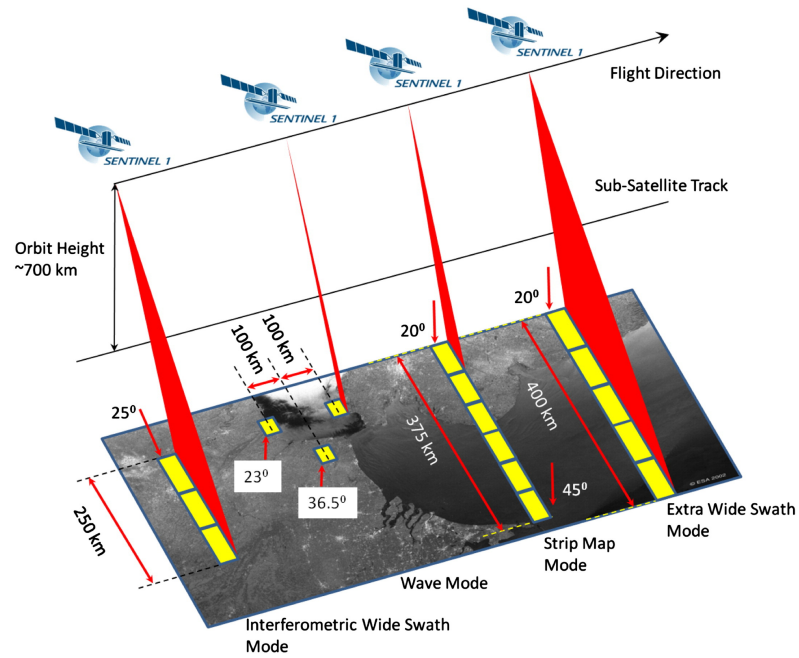


**Figure 2.17.** Sentinel-1 modes (ESA, European Space Agency, ndj)

SLC (Single Look Complex), Level 1 GRD (Ground Range Detected) and Level 2 OCN (Ocean), depending on their availability (globally, regionally and locally) and on a defined timescale (ESA, European Space Agency, ndh).

Single Look Complex products have spatial resolutions that depend on the acquisition mode (ESA, European Space Agency, ndq). They consist of focused SAR data geo-referenced using orbit and attitude data from the satellite and contains both phase and amplitude information (ESA, European Space Agency, ndi).

Ground Range Detected products are available in one of three spatial resolutions (Full Resolution (FR) for SM mode, High Resolution (HR) for SM, IW and EW modes and Medium Resolution (MR) for SM, IW, EW and WV modes) (ESA, European Space Agency, ndp). They consist of focused SAR data that has been detected, multi-looked and projected to ground range using an Earth ellipsoid model and contain only the amplitude information. The ellipsoid projection of the GRD products is corrected using the terrain height specified in the product general annotation. The terrain height varies in azimuth but is constant in range (but can be different for each IW sub-swath) (ESA, European Space Agency, nde). The resulting product has approximately square spatial resolution pixels and square pixel

spacing with reduced speckle at the cost of worse spatial resolution (ESA, European Space Agency, ndi). Level-2 OCN products are provided at a spatial resolution of  $20\text{km}$  by  $20\text{km}$  (ESA, European Space Agency, ndr).

In addition, Sentinel-1 is a phase-preserving dual polarisation SAR system. It can transmit a signal in either horizontal (H) or vertical (V) polarisation, and then receive in both H and V polarisations (ESA, European Space Agency, ndd). All acquisition modes can transmit on both polarizations and their combinations (HH, VV, HH+HV, VH+VV) except WV mode, which transmits only HH and VV. In table 2.1 a summary of the acquisition modes main characteristics, including resolution and swath width, are reported.

**Table 2.1.** Incidence angle, resolutions, swath width and polarization of Sentinel-1 acquisition modes (ESA, European Space Agency, ndg)

Mode	Incidence Angle	Resolution	Swath width	Polarization
SM	20 - 45	5 x 5 m	80 km	HH+HV, VH+VV, HH, VV
IW	29 - 46	5 x 20 m	250 km	HH+HV, VH+VV, HH, VV
EW	19 - 47	20 x 40 m	400 km	HH+HV, VH+VV, HH, VV
WV	22 - 35 - 38	5 x 5 m	20 x 20 km	HH, VV

### 2.5.2 Sentinel-2

Sentinel-2 is the second constellation within Copernicus project for the initiative of the European Commission (EC) and the European Space Agency (ESA). It comprises a constellation of two polar-orbiting satellites (Sentinel-2A and Sentinel-2B), following sun-synchronous orbit, phased at  $180^\circ$  to each other. It is a European wide-swath, high-resolution, multi-spectral imaging mission (ESA, European Space Agency, ndo). It is designed to give a high revisit time of 5 days at the Equator. Sentinel-2 can acquire 13 spectral bands: four bands at 10 m, six bands at 20 m and three bands at 60 m spatial resolution (Fig. 2.18). The orbital swath width is 290 km.

The spectral bands of Sentinel-2 provide High Resolution (HR) data for land cover/change classification, atmospheric correction and cloud/snow separation. Temporal resolution is 5 days at the equator in cloud-free con-

Sentinel-2 Bands	Central Wavelength ( $\mu\text{m}$ )	Resolution (m)
Band 1 - Coastal aerosol	0.443	60
Band 2 - Blue	0.490	10
Band 3 - Green	0.560	10
Band 4 - Red	0.665	10
Band 5 - Vegetation Red Edge	0.705	20
Band 6 - Vegetation Red Edge	0.740	20
Band 7 - Vegetation Red Edge	0.783	20
Band 8 - NIR	0.842	10
Band 8A - Vegetation Red Edge	0.865	20
Band 9 - Water vapour	0.945	60
Band 10 - SWIR - Cirrus	1.375	60
Band 11 - SWIR	1.610	20
Band 12 - SWIR	2.190	20

**Figure 2.18.** Sentinel-2 bands and relative wavelengths (Satellite Imaging Corporation, nda).

ditions (ESA, European Space Agency, ndn). Sentinel-2 images have been used for many application, like land monitoring (Addabbo et al., 2016; Thanh Noi and Kappas, 2018; Topaloğlu et al., 2016), emergency management and security (Drusch et al., 2012; Martimort et al., 2007), agriculture (El Hajj et al., 2017; Veloso et al., 2017), coastal environment and shoreline extraction (Pardo-Pascual et al., 2018; Saleem and Awange, 2019) and so on. In figure 2.19 coverage and revisit time of Sentinel-2 is shown.

Sentinel-2 products are available for users in two levels (ESA, European Space Agency, ndm):

- Level-1C (Top-Of-Atmosphere reflectances in cartographic geometry),
- Level-2C (Bottom-Of-Atmosphere reflectances in cartographic geometry).

Products are a compilation of elementary granules, also called tiles, of fixed size, along with a single orbit. A granule is “the minimum indivisible partition of a product (containing all possible spectral bands)”. For Level-1C and Level-2A tiles are  $100 \times 100\text{km}^2$  ortho-images in UTM/WGS84 projection. All the specification on Sentinel-2 data are reported in the user handbook Delwart (2015).

**Sentinel-2 Constellation Observation Scenario:  
Revisit Frequency**



Validity start: October 2019

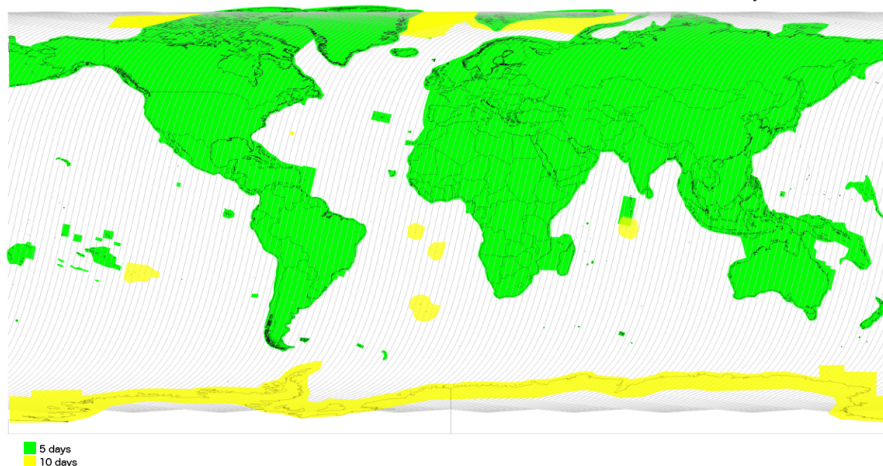


**Figure 2.19.** Sentinel-2 coverage and revisit time (ESA, European Space Agency, nds).

### 2.5.3 WorldView-2

DigitalGlobe’s WorldView-2 sensor provides Very High Resolution (VHR) satellite images. WorldView-2 satellite acquires eight-band multispectral images with a resolution of  $2m$  to provide the best natural representation of the Earth from space, and panchromatic images with a resolution of  $50cm$ . In particular, WorldView-2 is the first commercial high resolution satellite capable of acquiring, in addition to the four typical blue, green, red and near-infrared bands, four additional multispectral bands, previously unavailable on a very high resolution satellite: coastal, yellow, red edge, and Near Infrared 2 (NIR2) bands (Fig. 2.20). WorldView-2 operates at  $770km$  of altitude and its advanced onboard system is capable of capturing images above the Earth (Satellite Imaging Corporation, ndb). These images provide unprecedented detail, enabling very accurate detection.

In table 2.2, the main characteristics of the sensor are reported.

**Table 2.2.** WorldView-2 characteristics

<b>WorldView-2 characteristics</b>	
<i>Resolution</i>	50 cm
<i>Swath Width</i>	16.4 km
<i>Average revisit</i>	1.1 days
<i>Spectral bands</i>	Pan + 8MS
<i>Collection</i>	975,000km <sup>2</sup> per day

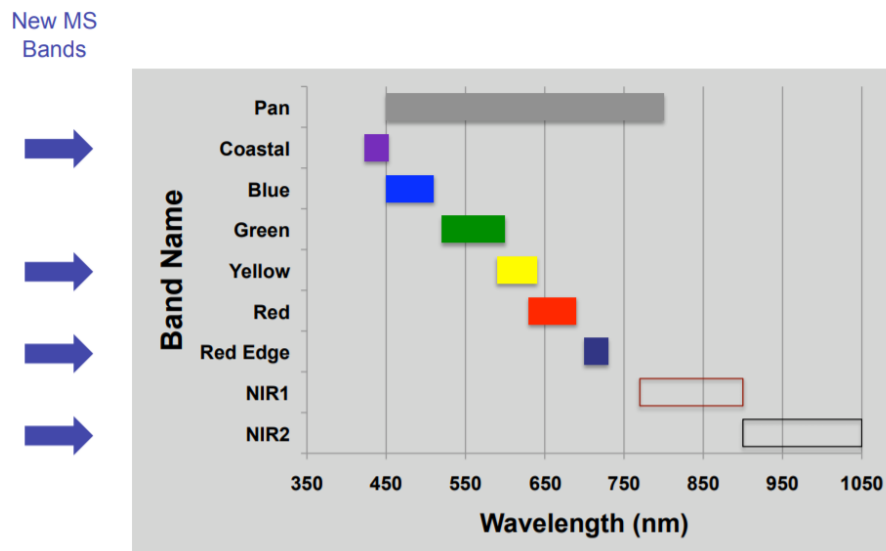


**Figure 2.20.** WorldView-2 bands. In addition to the four typical blue, green, red and near-infrared bands, four additional multispectral bands are available: coastal, yellow, red edge, and Near Infrared 2 (DigitalGlobe, 2009)

The VHR sensor has been used for many studies, like vegetation and biomass estimation (Immitzer et al., 2012; Mutanga et al., 2012; Yan et al., 2018), coastal (Martin et al., 2016; Siddiqui and Zaidi, 2016; Spagnoli et al., 2018), soil (Alexakis et al., 2018; Palombo et al., 2019; Umut et al., 2017), and so on.

#### 2.5.4 COSMO-SkyMed

COSMO-SkyMed (Constellation of Small Satellites for Mediterranean basin Observation) is the largest Italian investment in space systems for Earth Observation, developed by ASI (Italian Space Agency) and funded by Ministry of Education, Universities and Research (MIUR) and Italian Ministry of Defence (MoD), Rome, Italy. It is the first satellite observation system of the Earth conceived for dual purposes, i.e. civil and military (ASI, nd; ESA, European Space Agency, ndb). It is composed by 4 satellites equipped with Synthetic Aperture Radar (SAR) that work in the X-band (central frequency of 9.6 GHz), therefore it is able to see through clouds and during the night. The constellation became fully operational with all 4 satellites in May 2011. The operational life of the CSK system is 7 years and, after that, it is guaranteed by a second generation of satellites: the COSMO Second Generation (CSG) program. The system is great for emer-

gency situations because it can satisfy a user request (ability to deliver the image product required by an end user in a timely manner) within 72 h in the routine mode, 36 h in the crisis mode, and 18 h in the very urgent mode. The system is able to perform up to 450 images per day of the Earth's surface, equal to 1,800 radar images, every 24 hours. COSMO-SkyMed has three acquisition modes (Fig. 2.21) (Battagliere et al., 2019):

- spotlight, watching an area of  $10 \times 10 \text{ km}^2$  providing  $1 \text{ m} \times 1 \text{ m}$  geometric resolution;
- stripmap, observing a continuous strip of Earth's surface, with  $40 \times 40 \text{ km}^2$  extension and  $5 \text{ m} \times 5 \text{ m}$  geometric resolution in HIMAGE mode and  $30 \times 30 \text{ km}^2$  extension and  $20 \text{ m} \times 20 \text{ m}$  geometric resolution in Ping Pong mode;
- scanSAR, covering a region of  $100 \times 100 \text{ km}^2$  with  $30 \text{ m} \times 30 \text{ m}$  geometric resolution in WIDE mode and  $200 \times 200 \text{ km}^2$  with  $100 \text{ m} \times 100 \text{ m}$  geometric resolution in HUGE mode.

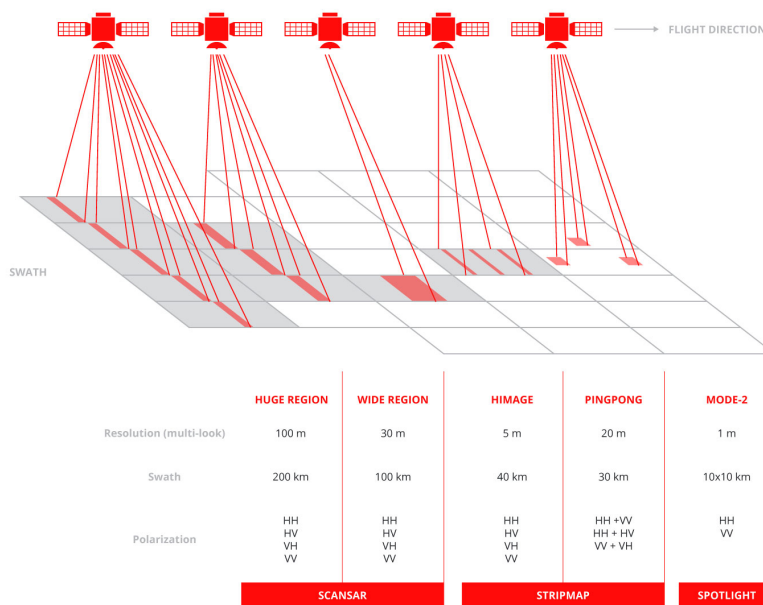
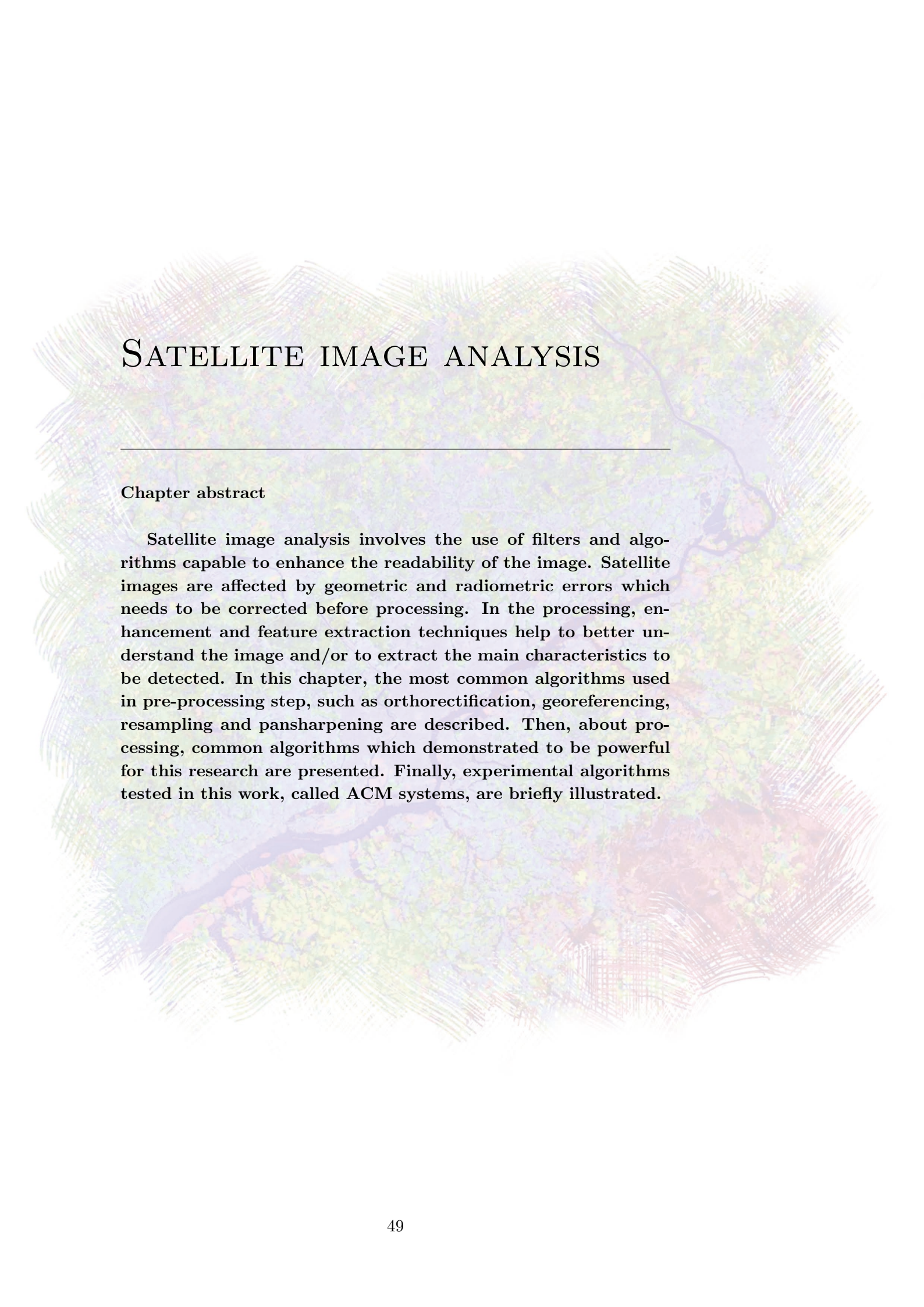


**Figure 2.21.** COSMO-SkyMed acquisition modes (e Geos, nd)

Constant monitoring of the evolution of a specific situation is possible thanks to the short revisit time, less than 12 hours. COSMO-SkyMed has already been used in many applications to monitor environmental disasters,

such as landslides (Bovenga et al., 2012; Konishi and Suga, 2018; Novellino et al., 2017), earthquakes (Lanari et al., 2010; Yun et al., 2015), oil spill (Cheng et al., 2014; Nunziata et al., 2018), flood (Pulvirenti et al., 2011; Refice et al., 2014), but also forests (Deutscher et al., 2013), archeological areas (Jiang et al., 2017; Tapete and Cigna, 2019) coasts (Bruno et al., 2016; Palazzo et al., 2012).



# SATELLITE IMAGE ANALYSIS

---

## Chapter abstract

Satellite image analysis involves the use of filters and algorithms capable to enhance the readability of the image. Satellite images are affected by geometric and radiometric errors which needs to be corrected before processing. In the processing, enhancement and feature extraction techniques help to better understand the image and/or to extract the main characteristics to be detected. In this chapter, the most common algorithms used in pre-processing step, such as orthorectification, georeferencing, resampling and pansharpening are described. Then, about processing, common algorithms which demonstrated to be powerful for this research are presented. Finally, experimental algorithms tested in this work, called ACM systems, are briefly illustrated.

### 3.1 Introduction

Satellite image processing is an essential step for analysing and monitoring forests, coastal areas, landslides and, in general, world cultural heritage. From one side, satellite sensors can provide images at every time and in every place of the Earth. In addition, there is no need to go physically to the places under investigation. Moreover, thanks to SAR system it is possible to acquire during day and night and in any weather condition, while thanks to multispectral images, additional information, which human eyes cannot see, can be captured. On the other side, satellite image processing is extremely complex: one of the first problem is that, in most of cases, computational work is hard and slow, due to the large dimensions of the satellite images. Furthermore, images captured by sensors are “raw” images and it is really important to find the best methodology (which depends on the image and on the purpose of the research) to correct geometric and radiometric distortions (chapter 2). The first ones are generally corrected by orthorectification and georeferencing, while the second one by resampling. It is obvious that, depending both on the purpose of the work and on the sensor taken into account, additional pre-processing steps can be performed (Dermanis and Biagi, 2002; Gomarasca, 2009). For example, pansharpening is one of the most used fusion technique for multispectral images. It merges panchromatic with multispectral image, improving its spatial resolution (Santurri et al., 2012). Other examples could be coregistration and calibration, which are important steps especially when two or more images need to be perfectly overlapped both geometrically and radiometrically. Images may come from the same or from different sensors, and have the same or different spatial resolutions (Turner et al., 2014). Coregistration and calibration are always applied, for example, in change detection analysis, which analyses any changes in the study area over time (Lu et al., 2004; Singh, 1989).

Once the best pre-processing is designed, the image is ready to be processed. This is an essential step for a good visual interpretation of remote sensing images. Processing works on different elements present in a scene, such as shape, hue, tone, texture and so on. The main advantages of visual

---

interpretation using always the same methodology for all the dataset is the repeatability and the objectivity. Manual interpretation allows to analyse one image per time, so it is time-consuming and subjective (Asokan et al., 2020). With the development of technology, alongside the traditional techniques, like enhancement, feature extraction, segmentation, change detection and so on, artificial intelligence and machine learning algorithms are taking hold and they are increasing the readability of satellite images.

In this chapter, at the beginning, some of the most common algorithms used to perform pre-processing (orthorectification, georeferencing, resampling and pansharpening) are described. Then, processing algorithms are presented. They are divided into “common” and “experimental” algorithms. Common algorithms are generally used in literature for many studies, including coastal applications. Experimental algorithms illustrated in this research have never been used on satellite images. They were originally born for the medical field, but they demonstrated to be a valuable resource also in remote sensing field.

## 3.2 Image pre-processing

In chapter 2 (sections 2.3.2, 2.3.3, 2.4.3 and 2.4.4), the most common image distortions have been presented. Before processing, they need to be corrected by means of algorithms and techniques. In particular, for geometric correction, orthorectification is used. Then, images need to be georeferenced: the internal coordinates of the image need to be related to a ground system of geographic coordinates. Moreover, radiometric errors are corrected by means of resampling technique. In conclusion, especially for multispectral images, an additional correction can be performed to enhance image properties: pansharpening.

### 3.2.1 Orthorectification

Orthorectification is a transformation process used to project two-or-more images onto a common image plane (Gobbi et al., 2018). It takes into account the distortions by means of a Digital Elevation Model (DEM) (Satellite Image Corporation, 2017). The DEM allows to transform the incorrect image to an image in which each pixel appears observed from a perpendicular position (Fig. 3.1).

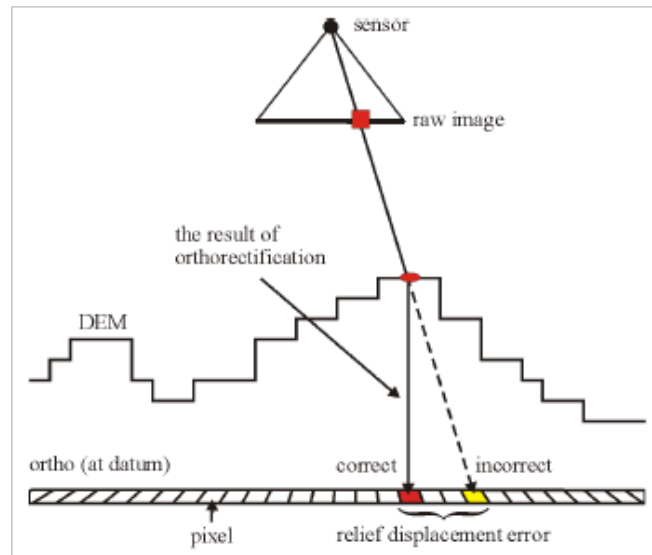


**Figure 3.1.** Orthorectification (PCI Geomatics, nd)

There are two methods to perform orthorectification: rigorous and non-parameter models (Boccardo et al., 2004). Rigorous model consists in the estimation of physical models which describe image distortions due

to the platform (position, velocity and distribution), the sensor (grip angle, panoramic effect), the Earth (reference ellipsoid) and cartographic projection (Gomasca, 2009). They are 3D models which need the knowledge of 3D coordinates of GCPs (Ground Control Points). The transformation between image space and object space takes place, therefore, through the reconstruction of the captured geometry, the knowledge of the acquisition method, the type of sensor and the satellite position. The rigorous approach is substantially photogrammetric (it is based on the collinearity equations) and takes into account the position and attitude of the satellite, the model of the sensor and the possible cartographic transformation, if terrain coordinates are provided in cartographic coordinates. The object coordinates can be resumed from the image coordinates using stereoscopic pairs of images or single records and a DEM (Fig. 3.2).

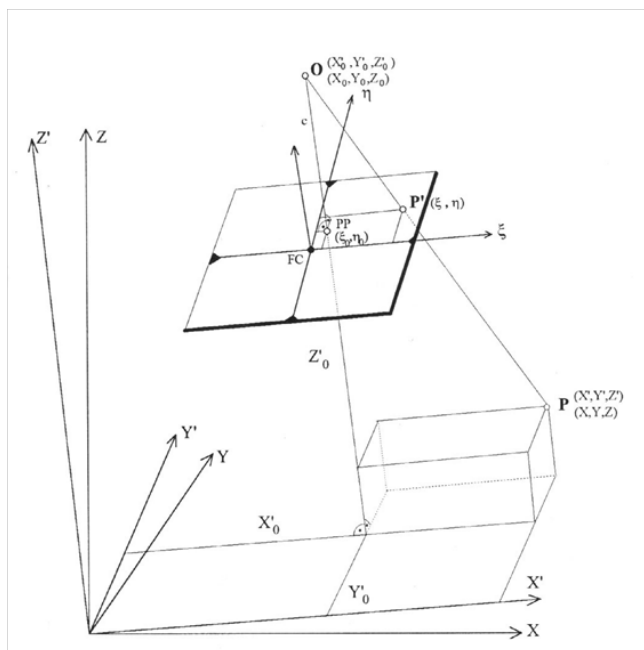


**Figure 3.2.** Rigorous model for orthorectification (Wolf et al., 2014)

Non parametric models are empiric models which try to describe the image distortions without a-priori knowledge of the grip (satellite position, velocity, distribution, grip geometry). They can be 2D (2D coordinates of GCPs) or 3D models (3D coordinates of GCPs). The transformation between image space and object space takes place through a mathematical functional relationship that does not take into account the physical process of geometric image generation (Gomasca, 2009). The most frequently

used non-parametric methods are the Rational Function Model, (RFM), Rational Polynomial Coefficients (RPC) and Rational Function Coefficients (RFC) (Dowman and Tao, 2002), as they are implemented in almost all software packages for satellite images processing. Rational function model, also called Rational Polynomial Function (RPF), consists in finding the relationship between the image coordinates  $(\eta, \xi)$  and the 3D coordinates of the object ( $X, Y$  and  $Z$ ) through polynomial relations (Eq. 3.1).

$$\begin{cases} \xi = \frac{P_a(X,Y,Z)}{P_b(X,Y,Z)} \\ \eta = \frac{P_c(X,Y,Z)}{P_d(X,Y,Z)} \end{cases} \quad (3.1)$$

where

- $\xi$  and  $\eta$  are image coordinates (row, column);
- $X, Y, Z$  are the object coordinates of the GCPs (E, N, H);
- $P_a, P_b, P_c, P_d$  degree polynomials equal to 3 for a total of 20 coefficients to be determined (Eq. 3.2).

Polynomial can be expressed as follow:

$$P_a(X, Y, Z) = a_0 + a_1X + a_2Y + a_3Z + a_4X^2 + a_5XY + \dots + a_{18}YZ^2 + a_{19}Z^3 \quad (3.2)$$

which can be also written as

$$P_a(X, Y, Z) = \sum_{i=0}^{m_1} \sum_{j=0}^{m_2} \sum_{k=0}^{m_3} a_{ijk} X^i Y^j Z^k \quad (3.3)$$

with

$$0 \leq m_1 \leq 3; 0 \leq m_2 \leq 3; 0 \leq m_3 \leq 3; m_1 + m_2 + m_3 \leq 3. \quad (3.4)$$

Equations 3.1 are called ‘‘Upward RFM’’: image coordinates can be obtained starting from the 3D coordinates of a ground point (Boccardo et al., 2004). There is not, therefore, the necessity of having the sensor model, but just the relation between image and ground coordinates. In

---

general, in the data set supplied with the purchased image, ASCII files with the extension .rpb or .rpf are provided. They contain geometric parameters of the camera mounted on the satellite. The coefficients  $a_{ijk}$  are the RPC (Rational Polynomial Coefficients). They are obtained from the satellites ephemeris or from an adequate number of GCPs by solving the equations through the method of least squares. They need a fairly large number of GCPs (at least 20). The 1st order terms models the distortions of the projection; the 2nd order the distortions of Earth curvature, atmospheric refraction and optical system; the 3rd order the camera vibrations and residual distortions (unknown) (Gianinetto, nd).

GCPs are points taken from variety of sources, such as the Global Positioning System (GPS), ground surveys, geocoded images, vectors, Geographic Information Systems (GIS), topographic maps. Their features needs to be clearly identified in the raw image in order to be linked to the known ground coordinates. A GCP determines the relationship between the raw image and the ground by associating the pixel (P) and the line (L) image coordinates to the X, Y and Z coordinates on the ground (Fig. 3.3) (PCI Geomatics, 2020).

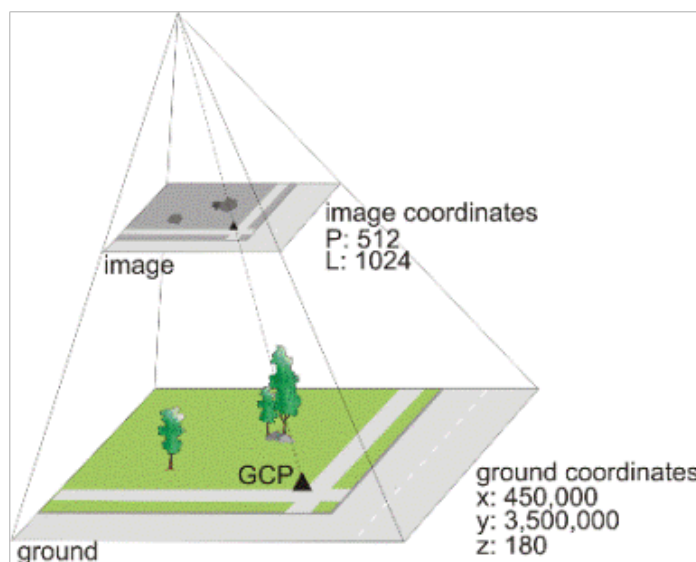


**Figure 3.3.** GCP: Ground Control Point (PCI Geomatics, 2020)

The choice of one of the two ways to perform orthorectification depends on the research purpose. The advantages of the RPF model are that it does not require information about the capture geometry, so they can work on every image; moreover it is implemented in most of the software. On

the other side, in the extended form, they require a big number of GCPs evenly distributed and it is less accurate and precise than rigorous models. Rigorous model requires few GCPs and it is a robust model but all the geometric and optical characteristics of the capture have to be known, and this is not always possible (for example, they are not available for the oldest images). Moreover, it requires more expensive and specific software.

### 3.2.2 Georeferencing

Georeferencing is the process that associates the internal coordinate system of a map or aerial photo image to a ground system of geographic coordinates, so to its right location on Earth (Hastings and Hill, 2009). There are two main methods for georeferencing. One consists in assigning geospatial coordinates directly to data and information objects; the other one, consists in relating the data to one or more pre-existing objects which are already georeferenced. The second way is the most used and can be performed “image to image” or “image to map”. With the first one, the processed image is overlapped on another image of the same previously corrected area; with the second one the image is overlapped on a map using a specific cartographic projection. Georeferencing is a really important step on image pre-processing because it makes aerial and satellite imagery comparable with other data, such as GPS points or data produced at different times.

### 3.2.3 Resampling

Resampling is used to radiometrically correct pixels already corrected geometrically. The process calculates the new pixel values from the original digital pixel values in the uncorrected image. In other words, the corrected radiometric information is assigned to the respective pixels. It is an essential step to bring back the geometric corrected pixels to the original radiometry (Natural Resources Canada, 2008). For all the pixels of the map, values must be calculated and re-assigned. This can be done by interpolating the values starting from the central pixel value. Resampling can be performed in three main techniques (Fig. 3.4) (Dave et al., 2015; Thakkar et al., 2016):

- nearest neighbour: the value of the input pixel, which is the closest

to the new output pixel, is used as output value;

- bilinear transformation: the values of 4 input pixels, which are the closest to the new output pixel, are used to interpolate output values;
- bicubic convolution: the values of 16 input pixels, which are the closest to the new output pixel, are used to interpolate output values.

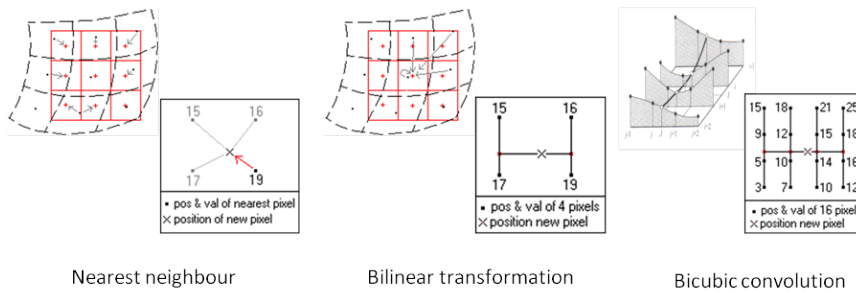


**Figure 3.4.** Resampling techniques (Spatial analyst, nd)

From nearest neighbour to bicubic convolution technique, computational work increases.

### 3.2.4 Pansharpen

In order to increase the quality of the image before its processing, pansharpening can be performed. It is a fusion process, aimed to merge high-resolution panchromatic and lower resolution multispectral imagery to create a single high-resolution coloured image (Humboldt State University, GSP216, 2014; Meng et al., 2019).



**Figure 3.5.** Pansharpening

The resulting image (Fig. 3.5) has the spatial resolution of the panchromatic and spectral and radiometric resolution of the multispectral image. There are many algorithms in literature to perform pansharpening (Loncan et al., 2015; Masi et al., 2016; Vivone et al., 2014). For VHR WorldView-

2 images considered in this research, Hyperspherical Color Space (HCS) algorithm was used (Padwick et al., 2010).

### **3.3 Image processing: state of art**

Image enhancement is the process of adjusting digital images so that the results are more suitable for display or for further image analysis. For example, by removing noise, sharpening, or brightening an image, the identification of the key features is easier. Image processing includes a number of methods used for enhancing subtle radiometric differences so that the eye can easily perceive them. In this section, the most common algorithms used for the presented research are explained.

#### **3.3.1 Decorrelation Stretch**

The decorrelation stretch is a process that is used to stretch the colour differences in a colour image (Alley, 1999). Decorrelation Stretch is useful to remove the high correlation commonly found in multispectral images and to produce a more colorful image (L3Harris Geospatial, nd). Input bands needed to perform decorrelation stretch are at least three, and PCA (Principal Component Analysis) is generally performed before it.

Principal component analysis (PCA) is the oldest multivariate technique and it is “a multivariate technique that analyses a data table in which observations are described by several inter-correlated quantitative dependent variables. Its goal is to extract the important information from the table, to represent it as a set of new orthogonal variables called principal components, and to display the pattern of similarity of the observations and of the variables as points in maps” (Abdi and Williams, 2010). In other words, it is a statistical procedure where the first principal component has the largest possible variance and each succeeding component in turn has lower and lower variance. In this way, dimensionality and, so, computational work are reduced and only significant variables are taken into account.

---

### 3.3.2 NDVI, Normalized Difference Vegetation Index

Among the vegetation indices (VIs), defined as the arithmetic combination of two or more bands related to the spectral characteristics of vegetation (Dermanis and Biagi, 2002), the Normalized Difference Vegetation Index (NDVI) is the most often used. NDVI takes part to the “band ratios” operations for image enhancement. Band ratios can be used to enhance the spectral differences between bands and to reduce the effects of topography. Dividing one spectral band by another produces an image that provides relative band intensities (Humboldt State University, 2014). In other words, the spectral differences between bands in the image is enhanced. NDVI combines NIR and Red bands, following equation 3.5:

$$NDVI = \frac{NIR - Red}{NIR + Red} \quad (3.5)$$

The number range goes from  $-1$  to  $1$  and in the image, bright areas are vegetated (with NDVI tending to  $1$ ) while non-vegetated areas (buildings, rocks, water) are generally dark (with NDVI tending to  $-1$ ). In addition, NDVI is able to compress the size of the data by a factor of two because it replaces two spectral bands with a single band.

### 3.3.3 WWVI, WorldView Water Index

WorldView Water Index (WWVI) takes part of Water Indices (WIs), specifically developed for water body detection, and it derives from the NDWI (Normalized Difference Water Index) (McFeeters, 1996), which has been widely used to delineate water areas from satellite images. NDWI works on the difference of spectral response between green and NIR channels, or between blue and NIR. NIR band is, indeed, strongly absorbed by water, while it is high reflected by vegetation and soil (Xu, 2006). NDWI (Eq. 3.6) is defined as the normalized ratio of the relatively high-reflective band ( $\rho_h$ ) and the low-reflective band ( $\rho_l$ ) (Xie et al., 2016):

$$NDWI = \frac{\rho_h - \rho_l}{\rho_h + \rho_l} \quad (3.6)$$

In the case of WorldView Water Index (WWVI), by taking advantage of coastal band, coastal and NIR bands (Hexagon Geospatial, 2015b) are

combined (Equation 3.7) increasing the spectral difference compared to traditional combination between blue and NIR bands, in terms of wavelengths:

$$WVWI = \frac{CB - NIR2}{CB + NIR2}. \quad (3.7)$$

Like NDVI, the range of the index goes from  $-1$  to  $1$ , with positive values of water features and negative values of vegetation/soil (Singh et al., 2015).

### 3.3.4 Supervised and Unsupervised Classification

Image classification is “the process by which each image in a dataset is identified to be a member of one of the inherent categories present in the image collection” (Olaode et al., 2014). In other words, classification collects pixels with similar values into groups (called clusters) that identify a specific category within the data (Lasalandra, 2009). Pixels are divided into categories based on their spectral properties. Classification can be performed in two ways: supervised and unsupervised.

Supervised classification is “guided” because the analyst controls the process by providing descriptors and giving training pixel samples he wants to classify. Each sample area contains pixels with well-defined spectral characteristics. The classification algorithm will analyse the spectral characteristics of each pixel of the image and associate it with the class with the spectral characteristics most similar to its own (spectral characteristic refers to the DN of the pixel in the bands that form the image). Therefore, this method is based on the hypothesis that the classes of “sample pixels” are known a-priori. The remaining pixels are classified according to their similarity to the sample pixels.

The following characteristics should be taken into account for choosing sample pixels:

- they have to be well-defined;
- pixels that are on the border between one class and another in the image must be avoided;
- all the spectral variations of a class (e.g. deep water and non-deep water) must be considered.

The steps (Martelli et al., 2009) to perform a supervised classification are shown in figure 3.6.

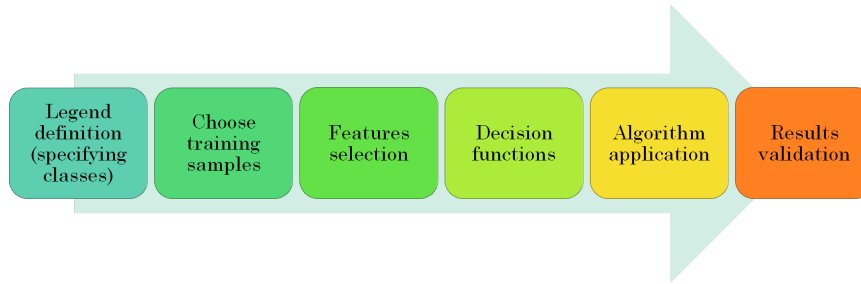


**Figure 3.6.** Steps for supervised classification

At first, classes are defined and then training samples are created by selecting features. Then, a decision function establish the way to classify the other pixels and, in the end, algorithms to classify are applied. The classification algorithm analyses, as aforementioned, the spectral characteristics of each pixel of the image and associates them with the class that have spectral characteristics most similar to its own. This can be done through various types of algorithms. Some of the most used are:

- Minimum distance;
- Parallelepiped classification;
- Maximum Likelihood;
- Spectral Angle Mapping.

Minimum distance uses the mean value of the training pixels for each class. One of the most calculated is the Euclidean distance  $d(x, y)$  (Eq. 3.8) between the measure vector  $x$  of every pixel and the mean value  $\mu_i$  of every class  $\omega_i$ :

$$d(x, y) = \sqrt{\sum_{i=1}^n (x_i^2 - y_i^2)} \quad (3.8)$$

where

- $x$  is the spectral signature vector of an image pixel;
- $y$  is the spectral signature vector of a training area;

- $n$  is the number of image band.

The class  $\omega_i$  for which the distance  $d(x, y)$  is minimal will be assigned to the pixel. The method is mathematically simple and computationally efficient, but it does not recognise the different dispersion degree of the classes in the feature space. Moreover, cases where classes are very close are not even suitable. In these cases, parallelepiped classification or maximum likelihood algorithms are more adequate, because they provide higher accuracy (Sisodia et al., 2014).

Parallelepiped classification (Fig. 3.7) is based on division of every axis in multi-spectral feature vector. For each class, the lowest and highest value on each axis is used to define decision boundary. In other words, it is an algorithm that considers a range of values for each band, forming a multidimensional parallelepiped. From lowest and highest values of each class, the accuracy is calculated and, if the pixel is outside the box, it is unclassified. One of the major drawbacks of this algorithm is that pixels whose signatures lie in the overlapping area of two or more parallelepipeds cannot be classified (Jog and Dixit, 2016).

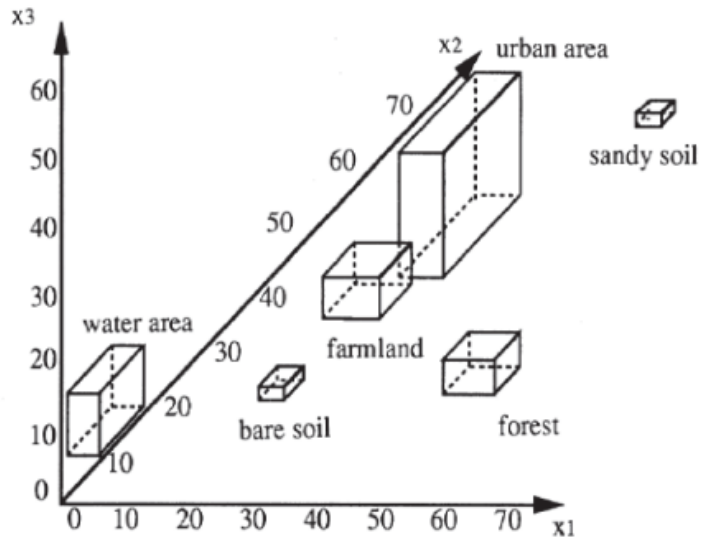


**Figure 3.7.** Parallelepiped classification (Jog and Dixit, 2016)

Maximum likelihood is a parametric classifier which uses statistics of second order Gaussian Probability Distribution Function (PDF) (Fig. 3.8). Gaussian PDF is expressed by equation 3.9:

$$f(x) = \frac{1}{\sigma\sqrt{2\pi}}e^{-(x-\mu)^2/2\sigma^2} \quad (3.9)$$

where,  $\sigma$  represents standard deviation and  $\mu$  represents mean value.

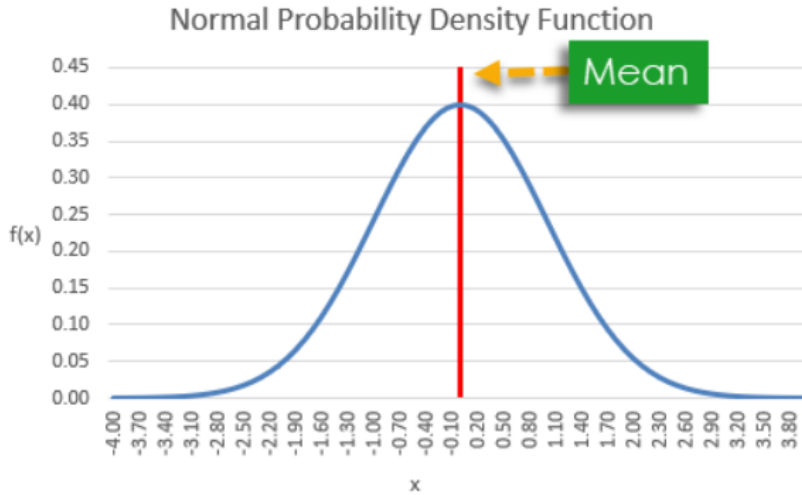


**Figure 3.8.** Gaussian Probability Distribution Function (PDF) (MacDougall, J., 2017)

Spectral Angle Mapping allows a quick classification and it is often used for hyperspectral images, which are characterized by high number of bands (Li et al., 2014; Park et al., 2007). It calculates the spectral angle between spectral signatures of image pixels and training spectral signatures. These spectra are treated as vectors in the feature space. The similarity is expressed as the angular distance between two vectors of the spectra in the n-dimensional space. The assigned class is the one with the shortest angular distance (Sohn and Rebello, 2002). The pixel will remain unclassified if this distance exceeds a threshold set a priori. The angular distance  $\alpha$  is measured in radians and it assumes values between zero and  $\Pi/2$ : low values of  $\alpha$  indicate a high similarity towards the reference spectrum related to a class, high values instead represent strong dissimilarities (Fig. 3.9).

In the unsupervised classification, a priori knowledge of the entity, typology, class descriptions is not required. It is deduced by making observations on the clusters in the feature space. Once the process of identifying the spectral classes is completed, the analyst will associate the thematic classes in relation to the knowledge of the territory. Clustering algorithms are the most used among the unsupervised classification. They group the

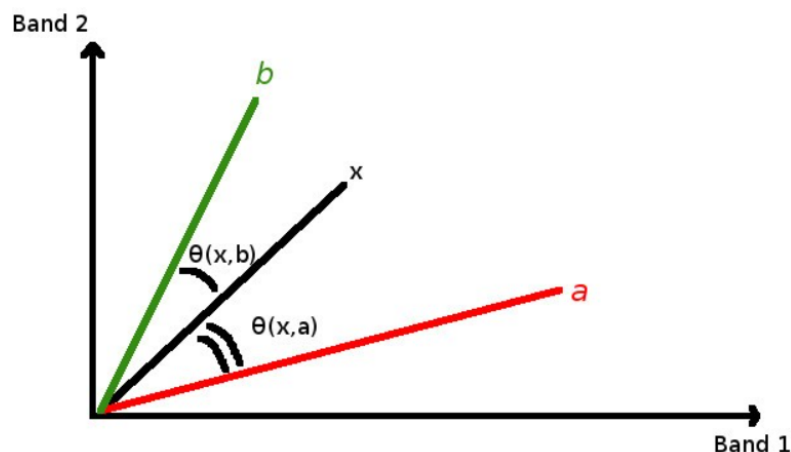


Figure 3.9. Spectral Angle Mapping (Congedo, L., 2020)

samples of a set using similarity concept: two samples in the same cluster are more similar to each other than two samples from different clusters. In other words, clustering means grouping pixels basing on spectral similarity. The main advantage of clustering resides in automation (Congedo, L., 2020). Two of the most famous algorithms for unsupervised classification are K-Means and ISODATA. The K-Means method is based on the calculation of the average spectral signature of clusters. ISODATA classifier is based on the Euclidean distance (Sohn and Rebello, 2002). Unsupervised classification is an iterative process (Fig 3.10) (Abbas et al., 2016).

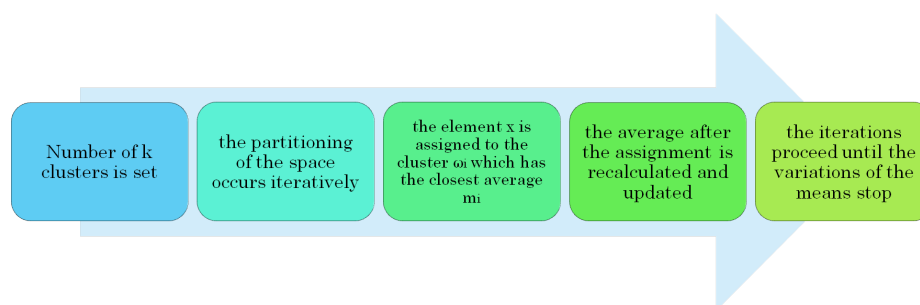


Figure 3.10. Unsupervised classification steps

The main differences between the two algorithms is that, for every iteration, ISODATA recalculates means and reclassifies pixels with respect to the new means, while in the K-Means, the number of clusters  $K$  are the same throughout the iterations (Abbas et al., 2016).

---

### 3.3.5 Canny Edge Detector

Canny edge detector is one of the algorithms among edge detection method. Its main purpose is to extract edges from an image. An edge in an image is a boundary where there is a change in some physical parameters and it is like a contour between two different regions. Key element is the brightness of the image: where there are image brightness changes, there are edges. The Canny edge detector is an edge detection operator that uses a multi-stage algorithm to detect a wide range of edges in images. It was developed by John F. Canny in 1986 (Canny, 1986). The Canny edge detection algorithm is composed of 5 steps (Sahir, S., 2020):

1. Noise reduction;
2. Gradient calculation;
3. Non-Maximum Suppression;
4. Double Thresholding;
5. Edge Tracking by Hysteresis;

Edge detection is really sensible to noise, so the first step removes the noise in the image with a  $5 \times 5$  Gaussian filter. Secondly, Sobel kernel is applied to calculate the first derivative in horizontal ( $G_x$ ) and vertical direction ( $G_y$ ), so that the edge gradient and the direction for each pixel can be found, following equations 3.10 and 3.11:

$$G = \sqrt{G_x^2 + G_y^2} \quad (3.10)$$

$$\theta = \tan^{-1} \left( \frac{G_y}{G_x} \right) \quad (3.11)$$

where  $G$  is the edge gradient and  $\theta$  defines the direction. Gradient direction is always perpendicular to the edges. Thirdly, Non-Maximum suppression is performed. It consists in finding pixels which are not a local maximum in the direction of the gradient and deleting them. The result is a binary image with only the thin edges. The double threshold step identify three kinds of pixels: strong, weak, and non-relevant. Strong pixels have

high intensity so they are used to determine the final edge; weak pixels have a low intensity but not small enough to be considered as non-relevant for the edge detection; the other pixels are considered non-relevant so they are not used to find the edges. Finally, hysteresis thresholding decides which are the real edges of the image. Weak pixels are transformed into strong ones, if and only if they are connected to strong pixels, otherwise they are discarded. At the end of the process, well defined edges are extracted from the image (Van Heesch, 2020).

### 3.4 Image processing: new experimental algorithms

In the previous sections, the most common indices, filters and algorithms used in literature for shoreline studies were presented.

In this section, new experimental algorithms, called ACM (Active Connection Matrix) Systems, never used on satellite images for territorial studies, are described. From the literature, the ACM Systems have presented good results in enhancing contrast and linear features on medical images. So, they seemed to be optimal to extract the instantaneous shoreline from high and very high satellite images. Nowadays, artificial intelligence is gaining ground also in this field, so what this thesis intends to test the applicability of new algorithms coming from this world, adaptable to the needs of this work.

ACM Systems include a number of algorithms developed by Professor Paolo Massimo Buscema, mathematician, Director of the Semeion Research Centre of Science of Communication of Rome and Full Professor Adjoint at the University of Colorado (USA). The patent concerns a systems according to which each image is considered as an active matrix (network) of connected elements (pixels) that develops over time. The main idea upon which this theory is based states that each digital image stores the maximum amount of information within the pixel values and their relationships. Furthermore, it is possible to obtain important information by analysing the reciprocal positions occupied by pixels. For a complete presentation of ACM algorithms, see Buscema (2006); Buscema and Grossi (2010).

Any digital image is a matrix made of as many rows as the pixels that determine the width and as many columns as the pixel related to the height.

Each pixel is identified by its coordinates  $i \in 1, \dots, R$ ,  $j \in 1, \dots, C$  and its brightness  $L \in 2^M$  (e.g., in the case of 256 shades of grey,  $M = 8$ ). For each pixel  $u_{ij}$ , a set containing all the surrounding pixels  $I_{(u_{ij})}$  named the *neighbourhood* can be defined. In the ACM systems, all the pixel  $u_{xy} \in I_{(u_{ij})}$  are linked to the central pixel  $u_{ij}$  by means of the  $w_{(ij),(xy)}$  connections. Figure 3.11 shows what is meant by neighborhood and the meaning of  $w$  connections in the case of *radius* = 1.

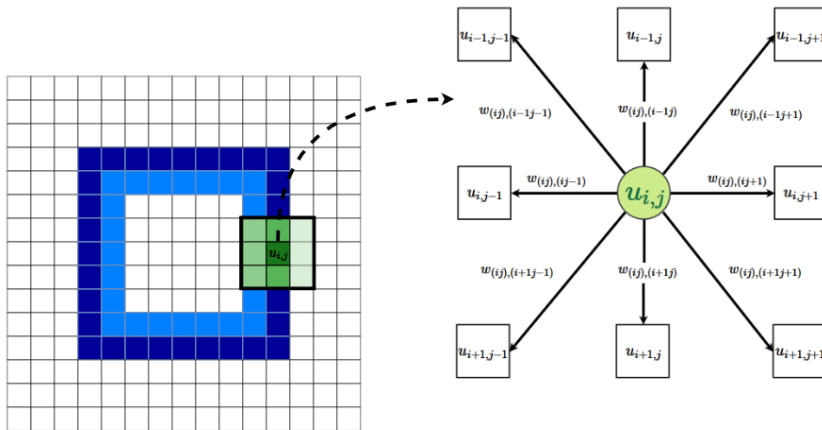


**Figure 3.11.** The  $I_{(u_{ij})}$  neighborhood of an example image with *radius*=1 and the relevant connections

Obviously, it is possible to use a larger radius by extending the number of pixels to be considered as the neighbourhood.

The systems are classified into three orders of complexity, according to the type of evolution over time. In the first order of complexity, the values of connections are initialised once, at the beginning, and then remain fixed while pixel values  $u_{ij}^{[n]}$  evolve over time until convergence, starting from the  $u_{ij}^{[0]}$  value, directly derived from the image. The situation is specular in the case of second order, where the pixels values are fixed and equal to  $u_{ij}^{[0]}$ , while the connections values  $w_{(ij),(xy)}^{[n]}$  are updated at each iteration, after initializing them to values  $w_{(ij),(xy)}^{[0]} \approx 0$ . Finally, the third order of complexity includes models in which both the pixels and the connections change over time.

So, ACM systems can be divided into three subfamilies: ACM systems with fixed connections and unit evolution, dynamic connections with fixed units and dynamic connections with unit evolution (Fig. 3.12).

The following algorithms were tested in this research: Automata Rule

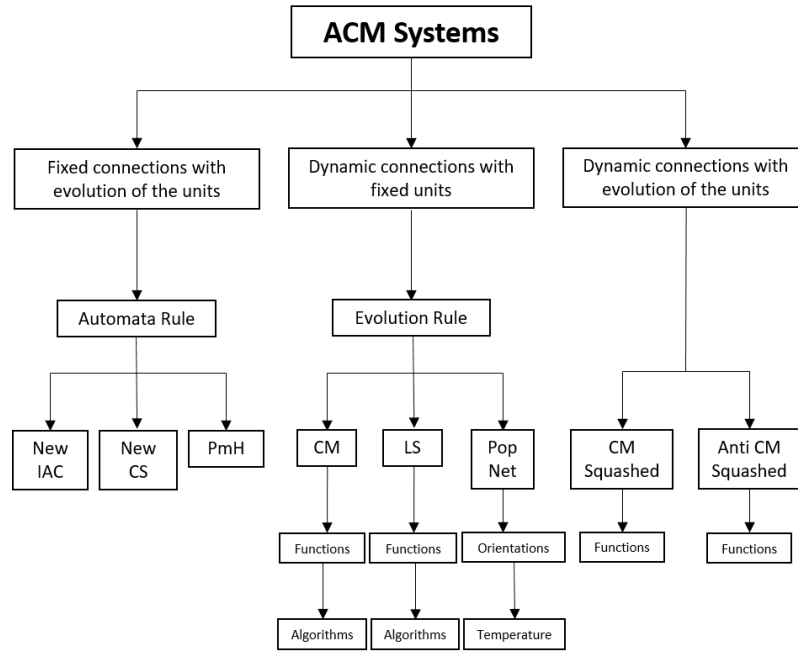


**Figure 3.12.** Groups of ACM Systems (Buscema, 2006)

(AR), New Interactive Activation and Competition (New IAC), New Constraint Satisfaction Networks (New CS), Contractive Map (CM) and J-Net Dynamic. The algorithms are exposed in detail in Appendix A. Here they are briefly explained.

### 3.4.1 Automata Rule

Automata Rule is part of the ACM systems with fixed connections with evolution of the units and it establish how to calculate the initial values for unit connections, starting from their original values. The connections between each pixel unit with each other are defined as a non-linear transformation of their different brightness. In the case of a neighbourhood of radius one, each pixel unit is connected with eight weights which are symmetrical to the pixel units located in its neighbourhood I (Fig. 3.13).

The values vary in a range from -1 to +1; in particular, it tends to define connections the closer to +1 the more the brightness values of the connected units are similar and the closer to -1 the more they are not.

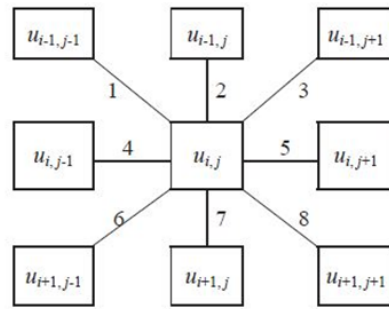


**Figure 3.13.** Pixel-unit connections with Automata Rule (Buscema, 2006)

### 3.4.2 New IAC, Interactive Activation and Competition Network

The central idea of New IAC is to consider each pixel of the image as an agent, connected to the other agents that make up its neighborhood (composed of 8 units in 2D images) by special connections (weights). At first, these connections are calculated by Automata Rule, then they act as constraints in each agent development dynamics (Buscema, 2006). In this case, the connections stay fixed at their initial value and they act only as impulse of the process and as constraint on the agents evolution. The action that each agent can perform consist in changing its brightness over time. Thanks to the weights which connect each agent to another, the light intensity of each agent will be the result of a continuous interaction between each agent and its weighted surroundings. Each agent, indeed, will receive at every instant of time, excitatory and inhibitory impulses from their surroundings. The first will tend to increase its luminous intensity; the second will tend, on the contrary, to reduce it. Moreover, each pulse will tend to dampen its strength over time and therefore each agent will tend towards a condition of low light intensity if not continuously excited from its neighborhood.

In short, New IAC is an ACM where each pixel is an agent that dynamically receives excitations and inhibitions from the others and consequently modifies its state. The system converges when the delta of change of each agent tends to zero and therefore when each unit (or pixel) settles on a value that does not change with the increase in time steps. A unit, the more excited will be, the more its brightness value is similar to that of the units around it. The maximum level of weighted brightness around, equal

to 8 because 8 are the units of the neighborhood, happens when the unit and its neighborhood are all at the maximum level of brightness (white). On the contrary, a unit, the more will be inhibited, the more its brightness value is different from that of the units around it. The minimum neighborhood brightness level, equal to -8, occurs when the unit is at the minimum brightness level (black).

### **3.4.3 New CS, Constraint Satisfaction Networks**

The central idea of New CS consists in considering each pixel-agent of the matrix as “hypothesis”, which can be gradually “true” or “false”, in relation to the brightness value of each pixel-agent (Buscema, 2006). The New CS system also inherits the local connections between each pixel-agent and its surroundings from the Automata Rule. These connections work as constraint conditions during the evolution of the Active Connection Matrix. The New CS algorithm tries to make true every hypothesis of the matrix, and therefore, to maximize the brightness of each pixel-agent.

### **3.4.4 CM, local Contractive Maps**

Local Contractive Maps (CM) is composed of a set of algorithms useful for processing an image through the evolution of local connections between its pixel-agents. The CM starts from the original central value of each pixel and leave it unchanged. Evolution, indeed, happens on the connections and, in every cycle, each new pixel takes its new brightness value according to the weights it has in that moment. In CM system, the connections between the pixel-agents (fixed units) and their neighbourhoods are bidirectional: each pixel-agent communicates with another pixel giving and receiving information.

### **3.4.5 J-Net Dynamic**

J-Net Dynamic, also called J-Net, considers the general situation in which both initial connections and units are dynamic. J-Net is a special algorithm capable of determining shapes and skeleton of an image at different levels of light intensity. The main goal of the J-Net system is to find the main

---

features present in an assigned image (Buscema et al., 2013). The scheme of this algorithm is shown in figure 3.14.

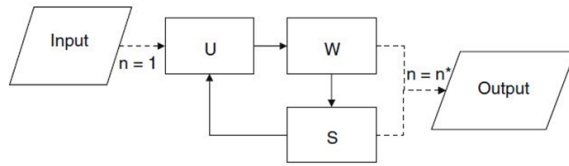


**Figure 3.14.** J-Net Dynamic scheme (Buscema et al., 2013)

The diagram represents the iterative process based on the evolution of three main units: the minimum units U (which represent the image and its dynamics), the connections W (which represent the dynamic link between the unit), and the state of the system S (which, combined with the W connections, allows the entire system to converge).

[Blank page]

# FIRST CASE STUDY: ORTONA'S COAST

---

## Chapter abstract

First case study concerns shoreline extraction in a village located in the centre of Italy, Ortona (CH), using Very High Resolution (VHR) WorldView-2 and High Resolution (HR) Sentinel-1 satellites images. The WorldView-2 eight spectral bands are suitable for this purpose, especially the coastal band, which is designed for coastal and maritime applications, thanks to its ability to penetrate under water surface. On the other side, High Resolution Sentinel-1 SAR images can easily discern boundaries in the image. Both the satellites images contain geometric and radiometric distortions, so they were initially pre-processed. Then, common filters were applied, such as NDVI, WVWI, classification and so on. Subsequently, experimental algorithms, called ACM (Active Connection Matrix), were tested and compared to the common ones. Many different information can be extracted by using these techniques, but, in both sensors, experimental algorithms are able to extract the shoreline closest to reference data.

## 4.1 Introduction

In view of what has been presented so far, four questions come spontaneously:

1. Is it possible to use, beside algorithms commonly used in literature, algorithms that come from machine learning world, never used for Earth applications, in the remote sensing field?
2. Is it possible to exploit and integrate information derived from two completely different sensors, like optical and SAR, for coastal applications?
3. Is it possible to successfully use full, open, free-of-charge, high resolution satellite image, like the ones derived from Copernicus Sentinel mission, to extract the shoreline?
4. Is it possible to develop an automatic/semi-automatic procedure for shoreline extraction?

This thesis has tried to answer to these questions.

The following experimentation, as first case study, concerns the shoreline extraction in Ortona (CH, Italy) using optical VHR WorldView-2 and SAR HR Sentinel-1 satellites images. As explained in chapter 2, WorldView-2 acquires eight spectral bands (coastal, blue, green, yellow, red, red edge, NIR1, NIR2) with 2 m of spatial resolution, and panchromatic band with 0.50 cm of resolution. Especially coastal and NIR2 band, the new bands previously unavailable on VHR satellite images, are useful for the purpose of this experimentation.

During the latest years, this sensor has been widely exploited for shoreline extraction. A recent and really interesting study was conducted by Minghelli et al. (2020). They used WorldView-2 imagery to extract the shoreline and to study its evolution in the presence of foam, before and after a tsunami. They tested a series of algorithms within the supervised classification on principally sandy coasts and they compared the obtained shorelines to manually extracted ones. For both the tested sites taken into account, one of the most important result was that erosion phenomena were

---

higher than accretion after tsunamis. Ataol et al. (2019) used a large set of images, including WorldView-2 to digitize the shoreline changes between 1951 and 2017 and to study erosion problems related to the construction of dams. Apostolopoulos and Nikolakopoulos (2020) used WorldView-2 image to study the accuracy of shorelines derived from diachronic Landsat images on two sandy beaches, proving that the shorelines derived from the low spatial resolution Landsat data are not very suitable for shoreline extraction.

About Sentinel-1, it is a SAR sensor, working in C-band, and it provides HR images, with spatial resolution of 10 m. There is not so much literature related to the use of Sentinel-1 images to study coastal areas and, in particular, shoreline extraction. Some studies are focused on lake or sea shoreline extraction, by means of fuzzy approach (Demir et al., 2019, 2016; Yen and Kim, 2020), proving the power of SAR images for coastline studies and pointing out the advantages of SAR in providing images during day or night and in any weather conditions. Pelich et al. (2020) propose an automatic and unsupervised coastline detection method to average the dynamical variations of coastal areas over a limited period of time by using Sentinel-1 time series, demonstrating that it is possible to improve the detection of vessels located next to the shoreline and to accurately map floods. In order to evaluate the results qualitatively, they used Sentinel-2 optical images, as it is presented in the case study of the present research, because in certain sandy areas, SAR images provide low backscattering values.

The two just presented kind of images were used for this experimentation. As widely explained, images contain geometric and radiometric distortions, so, at first, specific pre-processing is described for each sensor product. Then, common filters were initially applied (NDVI, WVWI, classification and so on), before comparing them to experimental systems called ACM (Active Connection Matrix). Finally, validation is assessed by manually extracted shorelines using visual inspection. This validation is considered to be reliable because the human brain takes into account many contextual parameters such as the color, the shape and the texture of the shore that the computer ignores (Minghelli et al., 2020). In literature, GNSS measurements are also used to validate the extracted shorelines. For

this case study, they are not used, due to time gap between the different data and the processing. However, this was done in the second case study, in Castelldefels' beach (chapter 5), so that both evaluation methods were tested.

---

## 4.2 WorldView-2

WorldView-2 panchromatic and multispectral satellite images of Ortona's coast (CH, centre of Italy) are provided by DigitalGlobe and they were taken on 29 June 2010 at 10:05 in the morning. They are shown in figure 4.1.

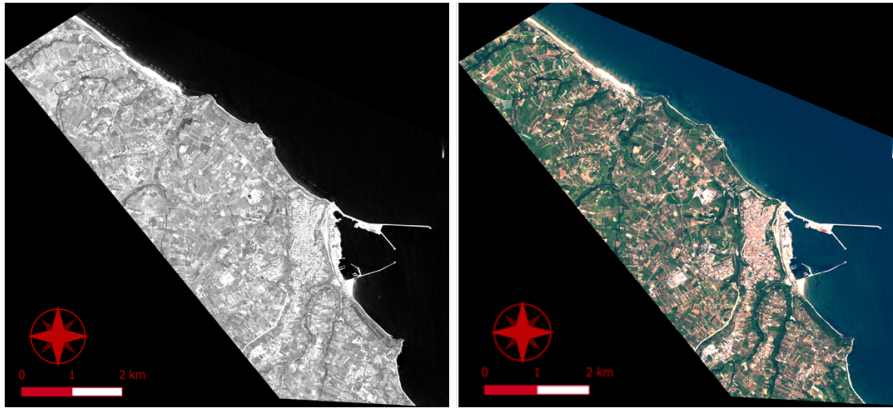


**Figure 4.1.** WorldView-2 raw image: panchromatic (on the left) and multispectral (on the right). Scene: Ortona's coast.

As reminder, WorldView-2 multispectral image (8 bands) has  $2m$  of spatial resolution, while panchromatic image has  $0.5m$ .

### 4.2.1 Pre-Processing

The “raw” images of Ortona's coast (both panchromatic and multispectral) contain geometric and radiometric distortions, so specific software based on rigorous algorithms or on rational polynomials must be used to correct them. The panchromatic and multispectral images are georeferenced to the WGS84 reference system (WGS84/UTM Zone 33 N, EPSG: 32633).

The image correction steps are (Di et al., 2003; Dominici et al., 2006; Hexagon Geospatial, 2015b):

- orthorectification;
- georeferencing;
- resampling;
- pansharpening.

Orthorectification, as explained in detail in chapter 3, is the process which removes perspective and relief effects in the image in order to create

a planimetrically corrected image. In this way, every point in the image is perpendicular to the sensor (OSSIM, 2014). It can be done by using a DEM (Digital Elevation Model, a raster of terrain elevations) and one of the following two models: rigorous or parametric. In this work, parametric model was used.

For the Ortona images, 23 GCPs (Ground Control Points) were acquired during a previous research (Dominici et al., 2006) by means of double-frequency GNSS receivers and processed in post-processing mode compared to the network of permanent stations of the Abruzzo region (Baiocchi et al., 2013). Eight of these were used as CPs (Check Points), to evaluate the accuracy of the measurements. To take into account land elevations, the basis for the relief displacements due to terrain elevations, DEM in software library was used. To correct geometric distortion of WorldView-2 satellite images, Rational Polynomial Coefficients (RPCs) were used. After that, resampling was performed, using the nearest neighbor technique. Then, the “HCS (Hyperspherical Color Space) Resolution Merge” technique was adopted (Padwick et al., 2010) to perform pansharpening. After these steps, the images are ready to be processed using the so-called “enhancement techniques”.

## **4.2.2 Processing**

After pre-processing, filters, algorithms and indices can be applied on the corrected image in order to extract useful information. At first, common techniques are tested. Then, experimental algorithms are applied.

### **4.2.2.1 Common filters, algorithms and indices**

A series of common filters, algorithms and indices (Hexagon Geospatial, 2015a) were tested on the image to find the ones that could show a clear and defined shoreline or gave useful information around it. ERDAS IMAGINE 2015 software was used.

#### **4.2.2.1.1 DECORRELATION STRETCH**

Decorrelation stretch was tested. The first step consisted in applying PCA (Principal Component Analysis), which is used in statistics for the simpli-

---

fication of source data. It is often used as a data compression method: it allows redundant data to be compressed into fewer bands using linear transformation (see chapter 3). Four bands were chosen (coastal, red, green, and blue bands) (Hexagon Geospatial, 2015b). Then, the decorrelation stretch filter was applied. This allows the whole range of DN (Digital Numbers) varying from 0 to 255 to be used and, therefore, a greater amount of information to be extrapolated. The decorrelation stretch is a sort of stretching that is applied only to the chosen four bands (main components) and not to the original image. The potential of this technique is exploited to highlight the elements that are almost invisible to the naked eye, to improve and facilitate visualization. The resulting image enabled clear shoreline distinction due to the radiometric response of the elements on the Earth's surface (Figure 4.2).

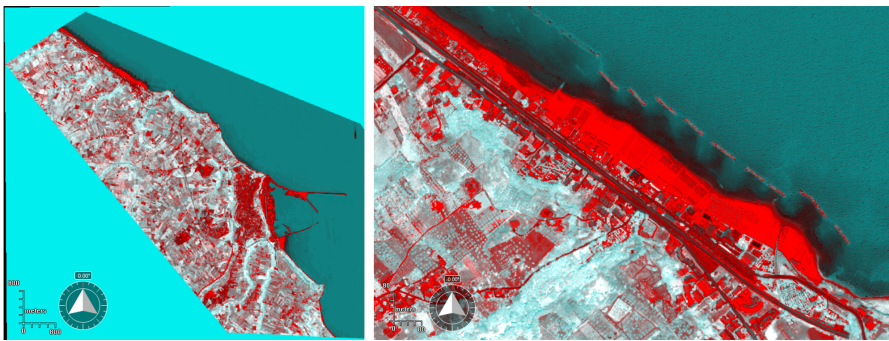


**Figure 4.2.** Results of the decorrelation stretch of the entire image (on the left) and its detail (on the right)

In Figure 4.2, the darker colour of the water indicates the presence of shallow waters, which correspond to artificial barriers (used to mitigate the erosive effect of the sea). The difference between wet and dry sand is revealed in the change of colour from dark to light red, respectively.

#### 4.2.2.1.2 NORMALIZED DIFFERENCE VEGETATION INDEX

The NDVIs (Wolf, 2012) are mainly used for forests or related to agriculture applications (Bao et al., 2014; Gandhi et al., 2015), but they also give excellent results in shoreline definition. As explained in section 3.3.2, the main objective of this index is to analyze the differences between the characteristic components of the vegetations spectral signature. The denominator assumes the role of normalization factor, while the relevant characteristic of

the index is the numerator. NDVI combines the red and the near-infrared (Equation 3.5) pixel by pixel.

According to this definition, NDVI ranges mathematically between  $-1$  and  $+1$ , but, in practice, between  $-0.4$  (water bodies) and  $+0.7$  (very dense and broad-leaved vegetation). In general, still water has low reflectance. The result computed for the shoreline is shown in Figure 4.3.

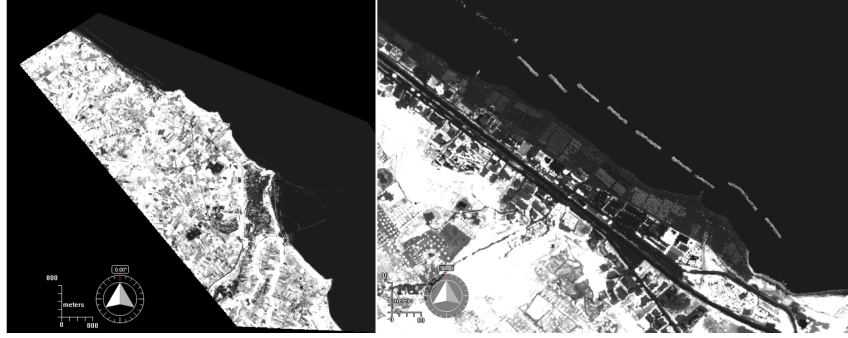


**Figure 4.3.** NDVI on the entire image (on the left) and its detail (on the right)

The shoreline between water and beach is visually well defined: the contrast between them is accentuated by the abrupt transition between black and white, respectively.

#### 4.2.2.1.3 WORLDVIEW WATER INDEX

The WorldView Water Index (WVWI) proved to be one of the most powerful algorithm. Above all, it is specific to images taken by WorldView satellites and, therefore, suitable for this case study. It is good for detecting water or shadows (Hexagon Geospatial, 2015b). As explained in section 3.3.3, traditionally the blue band is normalized with the NIR2 band, because the radiometric answer is clearly visible. The WorldView Water Index considers coastal and NIR2 bands (Equation 3.7) because the difference between these bands, in terms of wavelengths, is greater (coastal band  $400 - 450nm$ , blue band  $450 - 510nm$ , NIR2 band  $860 - 900nm$  (Land Info, 2018; Wolf, 2012)), so it provides an even more discrete threshold to identify water rather than land or vegetation areas.

The results of applying it to the WorldView-2 images are shown in figure 4.4.

Water has a much higher value on the coastal blue band than on the NIR2 band: this is why it is white in colour. The contrast between the

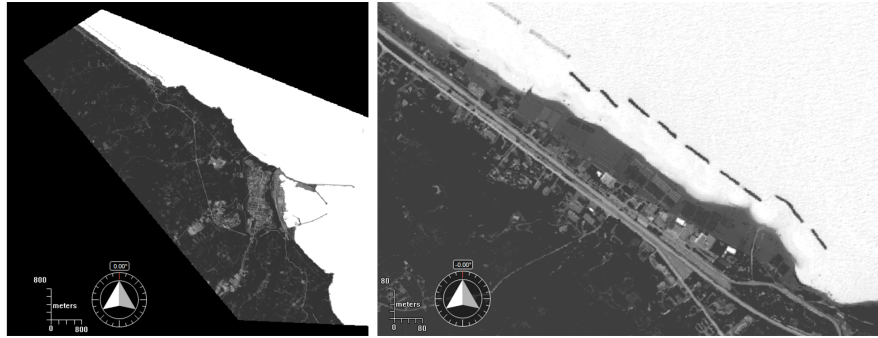


**Figure 4.4.** WorldView Water Index (WWWI) on the entire image (on the left) and its detail (on the right)

water and the ground is very high. The differences between deeper and less deep water and even between dry and wet sand are not evident, but this algorithm is definitely the best of those tested from the point of view of shoreline definition because it shows a clear contrast between water and land.

#### 4.2.2.1.4 UNSUPERVISED AND SUPERVISED CLASSIFICATION

The most delicate problem for classification is defining the type and number of classes. As explained in section 3.3.4, there are two types of classifications: unsupervised and supervised. K-means and ISODATA algorithms were tested for the unsupervised classification (Hexagon Geospatial, 2015b), taking 30 clusters into account. In the supervised classification, 12 clusters were identified, and the maximum likelihood parametric method was used (Lasalandra, 2009).



**Figure 4.5.** Unsupervised (on the left) and supervised classification (on the right)

The shoreline derived from both methods is well defined (Fig. 4.5), but the main information that can be extrapolated in the results of unsupervised classification is the difference in depth in the various areas of water

(from deep to less deep water, colour degrades from blue/grey, pink, blue, orange, to light blue at the shore). The same can be said for the difference between dry and wet sand where the drier sand is green, while wet sand varies from light blue to red. Comparing the results of supervised classification into 12 classes with unsupervised classification into 30 classes, the supervised classification reveals less information about sea depth.

#### 4.2.2.2 ACM Systems

The main purpose of this research is testing some experimental algorithms, so, in this section, they are tested on WorldView-2 images to determine their effectiveness for the case study.

For the Ortona case study, software ACM Batch was used (Buscema, nd). To test possible similarities or differences, the algorithms were tested on:

- a four-band image (coastal, red, green, and blue);
- an image containing only the coastal blue band (which is specific for coastal studies);
- an image with the coastal blue band plus NIR2;
- an image with only the NIR2 band.

These choices were carried out because these bands best respond to shoreline detection.

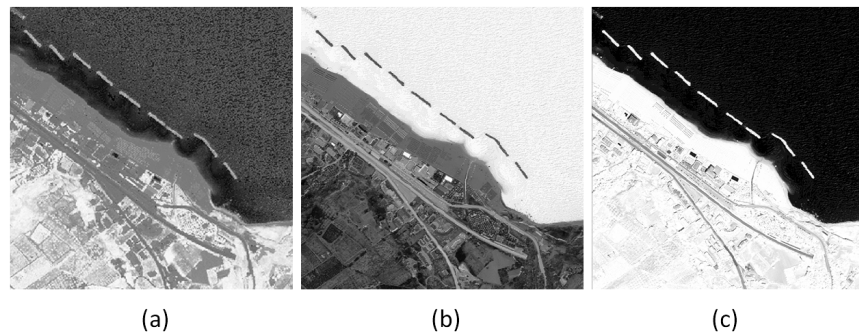


**Figure 4.6.** NDVI image (a), WVWI image (b), and application of CM on the NIR2 band image (c)

In this section of the thesis, only the results obtained by applying the Contractive Maps on the NIR2 image are shown in figure 4.6c, because it

---

had similarities with two of the common filters: NDVI and WVWI (Fig. 4.6a,b). The results of the other filters are shown in Appendix B.

### 4.2.3 Results and discussion

In every processed image, the high reflectance between land and water shows a defined shoreline, which is metrically detected taking three profiles (diagrams of the pixel values as a function of a distance) over three sample distances. As a reference, the pansharpened image is considered (Fig. 4.7). In this image, every color corresponds to a profile, and in particular, Profile 1 is blue, Profile 2 green, and Profile 3 red. These colors will be the same as the profiles plotted in figure 4.8.

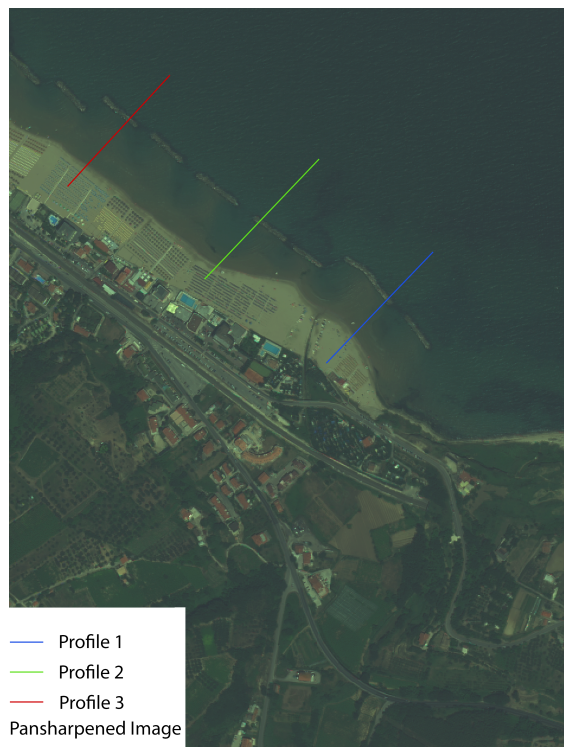


**Figure 4.7.** Profiles over three sample distances on the pansharpened image: Profile 1 is blue, Profile 2 green, and Profile 3 red

The letter A refers to the shoreline extracted from the pansharpened image, used as a reference. It is also worth noting the peaks at the rocks (Lines B and C) because they show similar trends in almost all the graphics. Line D in figure 4.8 refers to the shorelines extracted from, respectively, NDVI, WVWI, and CM over NIR2 band image. Line D was determined in correspondence with the maximum slope on the jump for the CM over the NIR2 image and in correspondence with the middle point of the jump

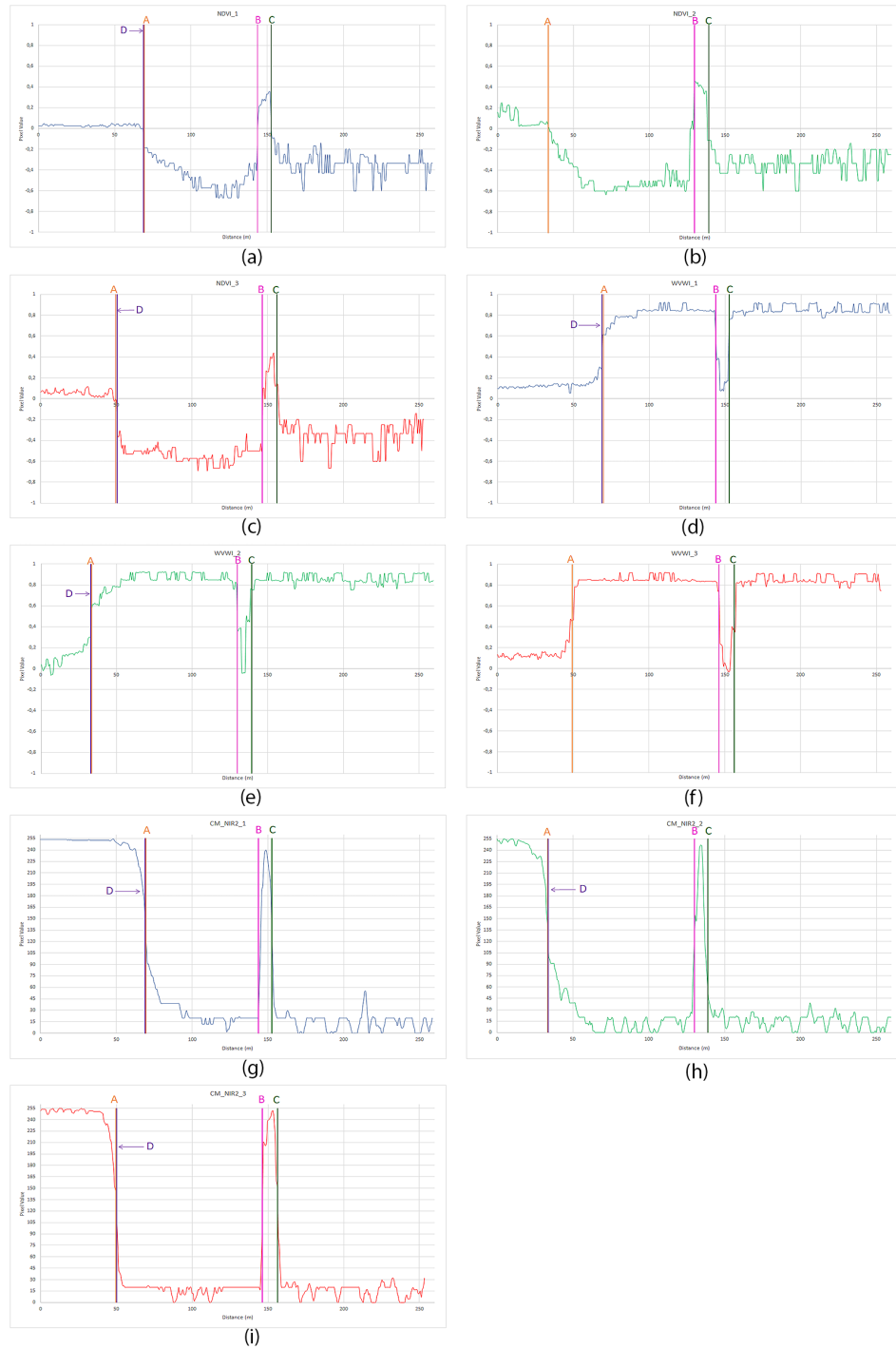


**Figure 4.8.** Profiles over three sample distances on: NDVI (a–c), WWVI (d–f) and CM over NIR2 image (g–i). A, B and C, D are respectively referred to the shoreline extracted from the pansharpned image, used as reference, the artificial rocks and the shoreline extracted from NDVI, WWVI and CM algorithms.

for the NDVI and WWVI. The differences between the reference image (pansharpned, Line A) and the other filter (Line D) was calculated (Tab. 4.1). For Profile Number 2 on the NDVI image (Fig. 4.8b) and Profile 3 on the WWVI image (Figure 4.8f), there was not a clear jump, which

---

emphasizes the shoreline, as in the other cases. For this reason, Line D on these two graphs is not drawn.

**Table 4.1.** Differences between the reference images and the other filters at the shoreline (m)

	NDVI	WVWI	CM
<b>Profile 1</b>	0.70	0.70	0.70
<b>Profile 2</b>	Not well defined	0.40	0.33
<b>Profile 3</b>	1.00	Not well defined	0.65

As shown in the table 4.1, the differences were the same for Profile 1, but they were closer to the reference value taken from the pansharpened image in the case of Profiles 2 and 3 for the CM filter.

A similar trend can be seen in the graphs. Peaks and hollows, which correspond to the passage from the mainland to the sea (and vice versa), are displayed at the same distance in all the graphs. In other words, in Profile 1, the first peak/hollow can be seen around 70 m and the second one around 150 m. This behavior is the same in all three for Profile 1 (Figure 4.8a,d,g). The same can be said for Profiles 2 (Figure 4.8b,e,h) and 3 (Figure 4.8c,f,i). This means that the algorithms worked in a very similar way. The original elaborations are shown in Appendix B.

### 4.3 Sentinel-1

The same area was studied by using SAR Sentinel-1 images. They need, as well as WorldView-2 images, to be pre-processed. Sentinel-1 images are freely available and are also supplied with a level of processing that guarantees immediate use (chapter 2). For this research, seven Sentinel-1 Interferometric Wide (IW) Level-1 GRD images (see Tab. 4.2) have been downloaded from Copernicus Open Access Hub website (ESA, European Space Agency, nda). This number of images proved to be a good compromise between a well-done speckle reduction and computational work for the SAR image in this area.

The chosen images consist, as mentioned in chapter 2, of focused SAR

**Table 4.2.** List of the Sentinel-1 images used for Ortona's coast analysis.

Sentinel-1 Images	
Number	Date dd/mm/yyyy
1	12/01/2017
2	06/01/2017
3	31/12/2016
4	25/12/2016
5	19/12/2016
6	13/12/2016
7	07/12/2016

data that have been detected, multi-looked and projected to ground range using the Earth ellipsoid model WGS84. The IW swath acquires data with 250 km swath at 5 m by 20 m spatial resolution. IW captures three sub-swaths using Terrain Observation with Progressive Scans SAR (TOPSAR) (ESA, European Space Agency, ndc). Ground range coordinates are the slant range coordinates projected onto the ellipsoid of the Earth. Pixel values represent detected amplitude; there is no information about the phase. For the IW GRD products, multi-looking is performed on each burst individually. All bursts in all sub-swaths are then seamlessly merged to form a single, contiguous, ground range detected image per polarization.

Seven Sentinel-1 images are processed in order to better remove the speckle, although just the one was processed for shoreline extraction. Information regarding tides was also taken into account to compare the instantaneous shoreline (TIDES4FISHING, nd). In Ortona area, the maximum high tide recorded in the tide tables is 0.6 m and the minimum height is 0.2 m, referenced to Mean Lower Low Water (MLLW). As the wave action on the Mediterranean coast is limited (Whitfield and Elliott, 2011) the images can be considered at the same tidal moment.

### 4.3.1 Pre-processing

The pre-processing of Sentinel-1 images is a key issue of SAR elaboration because, for a better identification of the shoreline, it is essential to improve the image quality, and in this case, to reduce noise while preserving the edges. Pre-processing methods can be grouped into noise reduction and image correction (Toure et al., 2019).

---

SAR images are affected by speckle, an effect caused by the coherent radiation used by radar systems (chapter 2). There are some adaptive filters, such as the median filter, which are suitable for SAR speckle removal. The median filter uses the median values within a moving kernel in place of each pixel of the image. That way, it smooths the image without smoothing the edges (Toure et al., 2019). The SNAP (Sentinel Application Platform) software is used to pre-process the Sentinel-1 SAR images. The pre-processing steps that were carried out are:

1. Thermal noise removal;
2. Apply Orbit file;
3. Calibration to Beta0;
4. Coregistration;
5. Multitemporal de-speckle;
6. Range doppler terrain correction.

Sentinel-1 Terrain Observation with Progressive Scans Synthetic Aperture Radar (TOPSAR) image is disturbed by additive thermal noise, particularly in the cross-polarization channel (Park et al., 2017). It is the additive background energy that causes a noise floor. The thermal noise removal is a radiometric correction and it is one of the most important pre-processing steps that must be done precisely to assure the quality of the results retrieved from satellite imagery.

Application of the orbit file is a crucial step because the orbit state vectors provided in the metadata of a SAR product are generally not accurate. They can be refined with the precise orbit files which are available days-to-weeks after the generation of the product. The orbit file provides accurate satellite position and velocity information. Based on this information, the orbit state vectors in the abstract metadata of the product are updated (Filipponi, 2019).

The purpose of SAR calibration is to provide imagery in which the pixel values can be directly related to the radar backscatter of the scene. The calibration is part of the radiometric correction. The pixel values

of the SAR images truly represent the radar backscatter of the reflecting surface. The radiometric correction is also necessary for the comparison of SAR images acquired with different sensors, or acquired from the same sensor but at different times, in different modes, or processed by different processors.

In coregistration step, a single image with all the considered bands is generated from the individual Sentinel-1 images. The pixels of the “slaves” images are resampled into the geographical raster of the master. This step is important in order to apply speckle filtering and, then, to consider only the date of interest.

About speckle reduction, multi-temporal filtering is one of the commonly used speckle noise reduction technique (Quegan et al., 2000) and it is applied in this work.

Finally, due to topographical variations of a scene and the tilt of the satellite sensor, distances can be distorted in the SAR images. Image data not directly at the sensors Nadir location will have some distortion. Terrain corrections are intended to compensate for these distortions so that the geometric representation of the image will be as close as possible to the real world.

The pre-processing aims to enhance the image for a better interpretation. In particular, the purpose is to increase the contrast while preserving the edges, using bands, algorithms and polarizations which maximize the difference between coast and water. The following options were tested:

1. Use decibel bands or not;
2. Use polarization VV or VH;
3. Choose the filter for the multitemporal de-speckle.

Two masks, one on the sea and one on the mainland, have been created and statistics (minimum, maximum, mean and standard deviation) have been computed by using the ENVI software (Harris Geospatial Solutions, Broomfield, Colorado, United States). The results show that the contrast between sea and land is higher using the decibel bands and VH polarization. Among the filters computed with SNAP to reduce the speckle, the one

which maximizes the contrast is the IDAN, but it presents the problem of excessively smoothing the edges. For this reason, the Lee filter is used, because it is a good compromise between keeping the spatial resolution and preserving the edges (Marghany et al., 2010; Pradhan et al., 2018; Taha and Elbeih, 2010). Finally, the image selected for analysis and shoreline extraction was the one in decibels, with the VH polarization and whose speckle had been reduced using the Lee filter. Figure 4.9 shows the image acquired on December 31, 2016 after the pre-processing.

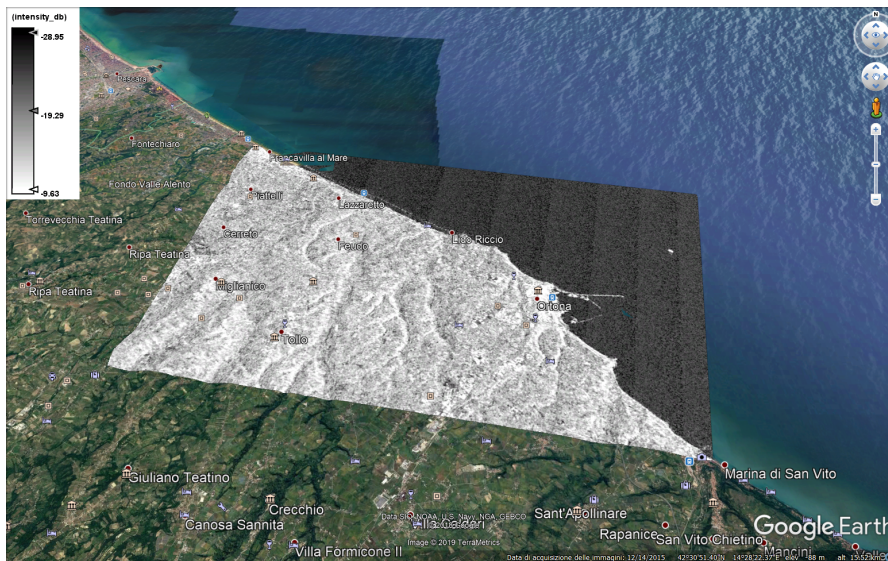


**Figure 4.9.** Pre-processed and georeferenced Sentinel-1 image. Date: December 31, 2016. Units: decibels. Polarization: VH polarization. De-speckle filter: Lee.

### 4.3.2 Processing

After image pre-processing, common filters were tested, as it was done with WorldView-2 images. They are presented in the following subsections.

#### 4.3.2.1 Common filter

Several approaches have been proposed to outline the shoreline using remote sensing, such as edge detection, segmentation and classification approaches (Toure et al., 2019).

Many algorithms have been used for edge detection; for example, the Canny edge detector (Liu and Jezek, 2004; Zhang et al., 2013) or the snake model (Sheng et al., 2012). Segmentation methods can be divided into three categories: threshold-based, region-based and edge-based (Ma and

Zhang, 2019). Concerning classification, they can be pixel-oriented, based on individual pixel classifications, or object-oriented, which instead is able to group characteristics by aggregation in similar regions or polygons.

In this part of the test, edge detection algorithms were used to extract the shoreline. It was also manually vectorized to create a reference. As reference shoreline, both an orthorectified Sentinel-2, acquired on 1 January 2017, and the Sentinel-1 on 31 December 2016 itself were used. Due to the inherent characteristics of the SAR images, a better reference line can derive from orthoimagery. This is the reason why the Sentinel-2 optical image was also used as reference. As it is provided already orthorectified, it was pre-processed by applying the atmosphere correction using the Sen2Cor tool in SNAP, and then, it was resampled to 10 m. Finally, the NIR band (that is band 8 in Sentinel-2) was chosen to extract the reference shoreline. The NIR2 band is indeed suitable for discriminating water from wet and dry sand, as it is almost completely absorbed by the water and possible perturbations are minimized by the shallow bottoms (Alesheikh et al., 2007; Braga et al., 2013).

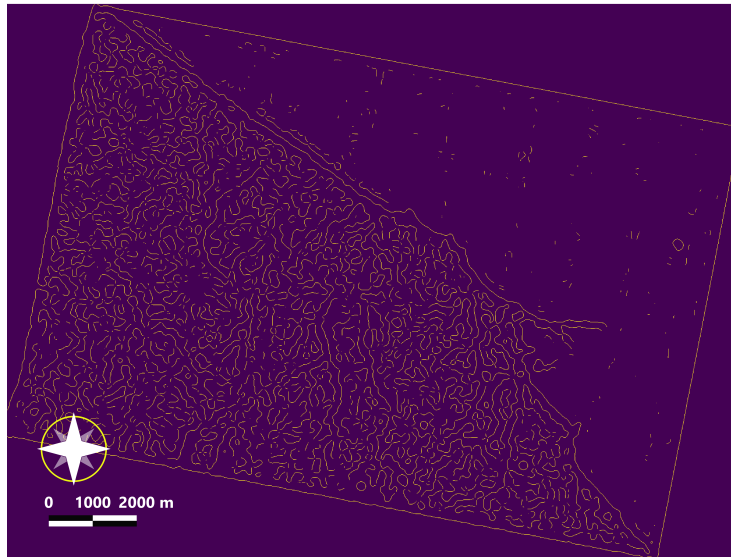


**Figure 4.10.** Canny algorithms applied on the pre-processed Sentinel-1 image acquired on 31 December 2019

The used filter for this case study is the Canny edge detector, which detects a wide range of edges in raster images and produces thin edges as a raster map. As fully explained in chapter 3, it operates, at first, with a Gaussian filter (based on normal distribution) to reduce the noise, then

---

two orthogonal gradient images are computed. Finally, only relevant or significant edges are extracted by thresholding with hysteresis (Kratochvilova and Petras, 2020). The result is shown in Figure 4.10.

#### 4.3.2.2 ACM System

In this section, a new ACM algorithm is tested, because of its capability in extracting edges. In this way, a comparison between common and experimental filters can be done. The experimental algorithm, called J-Net Dynamic (Buscema, 2006; Buscema et al., 2008), was tested both on the very high resolution (VHR) WorldView-2 optical image, and for the first time, on a high resolution (HR) Sentinel-1 SAR image. The J-Net Dynamic algorithm can be considered an edge operator, as it highlights the edges of the image. It is part of the active connection matrix (ACM) system. The system can automatically extract features of the images (edges, tissue differentiation, etc.) when they are activated by original non-linear equations. ACM activation reduces the image noise while maintaining the spatial resolution of high contrast structures.



**Figure 4.11.** Application of the J-Net Dynamic algorithm on the SAR Sentinel-1 image acquired on 31 December 2016

The J-Net Dynamic exploits the dynamic connections between a central pixel and its neighboring pixels (chapter 3). The relationships among these latter pixels with their neighbors is also taken into account, so the new

image is created considering the totality of these contributions at every elaboration cycle. Every single neighbor pixel participates in the evolution of the ACM, which is finally used to create the pixel matrix with the new image. A detailed description of the algorithm can be found in Appendix A.

The result provided by the J-Net Dynamic algorithm on the SAR image is shown in Figure 4.11.

### 4.3.3 Results and discussions

In the first presented part of the work, the potential of the ACM models for the automatic identification of the coastline from very high resolution multispectral satellite images has been tested. The ACM models already successfully applied in other (mainly health) applications have been adapted and tested here for the first time on satellite images. To verify the accuracy and robustness of this approach, the results of the experiments on a sample area were compared with those obtained on the same area using all the algorithms and filters most commonly used for these same applications (Maglione et al., 2014). By combining the various types of images with the various models, it was possible to obtain a wide range of tests in order to validate the model exhaustively on the specific test site. More in detail, by comparing the profiles obtained automatically by the various algorithms, the ACM models always showed an accuracy greater than or equal to that of the most common methodologies. Moreover, the measured deviation from what can be observed on the screen was always the result of the order of the pixel and often subpixel, making the method even more accurate than the much more expensive and time-consuming manual acquisition.

In the second part, SAR Sentinel-1 images was used. In order to link the experimentations, the J-Net Dynamic algorithm has been tested also on WorldView-2 images. At first, WorldView Water Index filter was taken into account. Secondly, a reclassification based on the threshold was performed and finally the shoreline was digitized with the Arcscan tools in ArcMap (ESRI, Redlands, California). Thirdly, a smoothing algorithm was used to improve the quality of vector line (Bodansky et al., 2001).

The J-Net Dynamic algorithm has been tested on the NIR2 band, which

gave the best results, as previously said. The J-Net Dynamic algorithm permitted to obtain a clear separation threshold between water and land (Fig. 4.12).

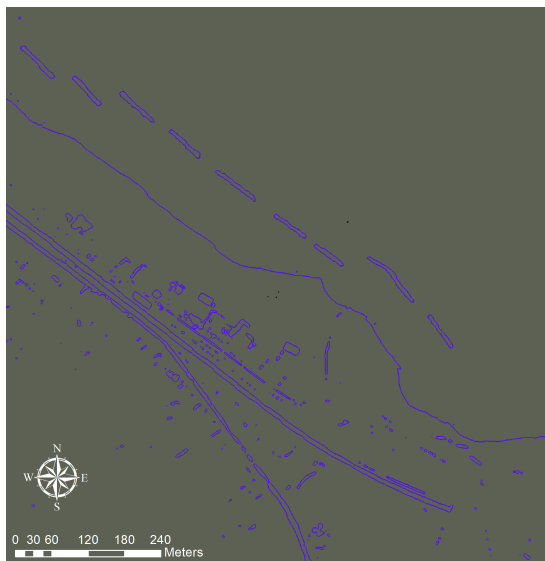


**Figure 4.12.** J-Net algorithm tested on NIR2 band of the WorldView-2 image

The vectorization of the shoreline extracted by J-Net is performed in the same way of the WVWI. The shorelines extracted from the WorldView-2 image are presented in figure 4.13: the red line illustrates the shoreline extracted manually, while the yellow one is the one generated using the WVWI and the blue one from the J-Net Dynamic.

The three instantaneous shorelines extracted using the Sentinel-1 image are shown in figure 4.14: the red one is the shoreline extracted manually, the yellow one is from the Canny algorithm and the blue one is from the J-Net Dynamic algorithm. The additional green line is the shoreline manually extracted from Sentinel-2, acquired on 1 January 2017; that is, one day after the Sentinel-1. It was also used as a reference for the reasons previously explained.

In order to compare the accuracy of the obtained shorelines, an index  $I$  (Eq. 4.1), reported in literature (Guastaferrero et al., 2011; Maglione et al., 2014), is used:

$$I = \frac{S}{L} \quad (4.1)$$

where  $S$  is the area calculated between the shoreline extracted from the

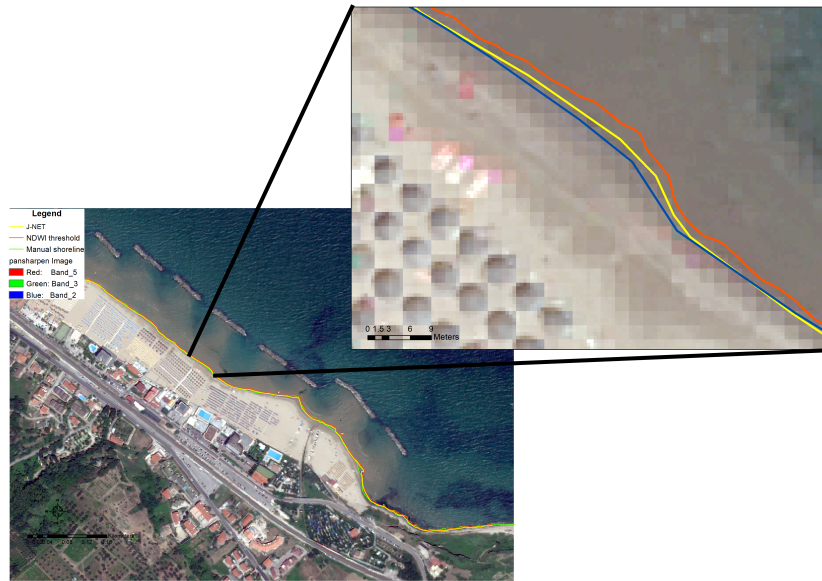


**Figure 4.13.** WorldView-2 image with three shorelines: the red line is the manually extracted shoreline; the yellow one is generated using the WVWI and the blue one from the J-Net Dynamic algorithm

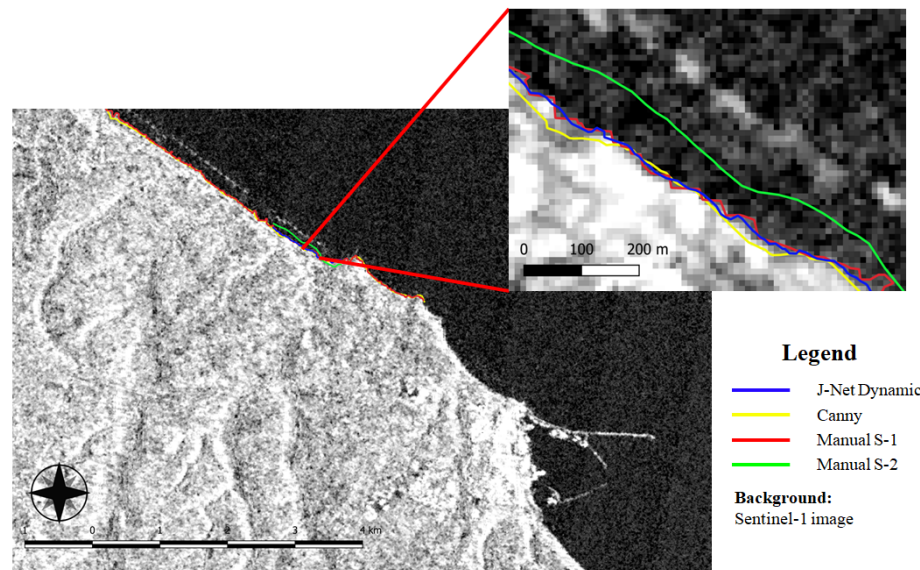


**Figure 4.14.** SAR Sentinel-1 image on the background showing four shorelines: the red and the green lines are, respectively, the shorelines manually extracted from Sentinel-1 and Sentinel-2 images; the yellow one is the one generated using the Canny algorithm and the blue one from the J-Net Dynamic algorithm.

algorithm and the shoreline used as reference; and  $L$  is the length of the reference line. The index is expressed in metres. The obtained values are shown in table 4.3.

The results of the index indicate that the use of J-Net Dynamic algorithm improves the shoreline extraction both in the optical and in the SAR

**Table 4.3.** I Index values (both in metres and in pixel) and percentage of increase for VHR optical and HR Sentinel-1 images

Image	Reference	Algorithm	I (m)	GSD (pixel)	Increase (%)
Optical WV-2	Pansharpened image	WV-WI	1.67	3.34	28.14
		J-Net	1.20	2.40	
SAR S1	Sentinel-1 image	Canny	12.52	1.25	58.19
		J-Net	5.86	0.59	
	Sentinel-2 image	Canny	66.49	6.65	8.60
		J-Net	60.77	6.08	

image compared to the common filters. For the optical WorldView-2 image, the index I is equal to 1.67 m using WVWI indexed image and 1.20 m using the J-Net Dynamic derived image. This means that, in the VHR image, the J-Net Dynamic algorithm improves the accuracy by about 28%. For the SAR Sentinel-1 image, considering as a reference the shoreline extracted from the Sentinel-1 image, the index I is equal to 12.52 m using Canny derived image and 5.86 m with the application of the J-Net Dynamic filter. In brief, in the HR SAR image, the accuracy is increased by about 58%. Considering as reference the shoreline extracted from Sentinel-2 image, the index I is 66.49 m for the Canny and 60.77 m for the J-Net Dynamic, which means an increase of almost 9%. All the results proves that the shoreline extracted from the J-Net Dynamic derived image is over-fitted to the reference compared to the ones extracted from the common filters. Two more things can be also noted: the first one is that there is a higher difference between the SAR image values than the optical image values. This happens because the SAR image has a lower resolution. The second one is that, with respect to the SAR image, there is a big difference depending on the chosen reference shoreline. The ones extracted with the algorithms are further away from the Sentinel-2 than the Sentinel-1 reference shoreline. The SAR image, due to its nature, could have little backscattering from the wet sand, which means that, in this case, it “confuses” the wet sand with water. However, the purpose of this research is to test the J-Net Dynamic on optical and SAR images and to compare the results to the common algorithms. In all of the aforementioned cases, it proved to extract a shoreline closest to the reference one.

To better determine the accuracy of the shoreline extraction, a method

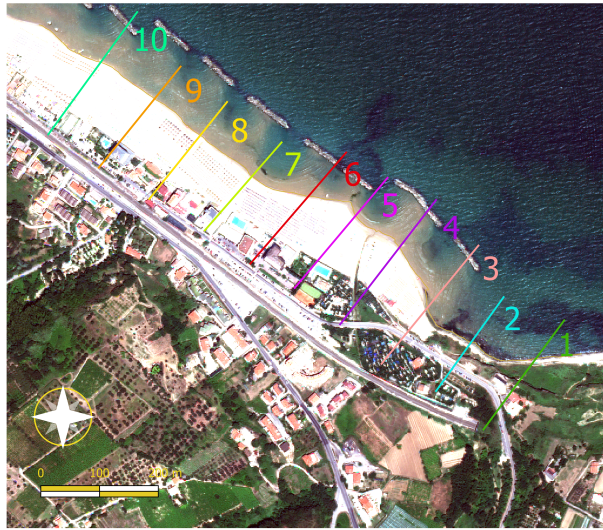


**Figure 4.15.** Ten transects every 100 m, drawn from the land to the sea, to calculate the intersection between them and seven shorelines extracted from WorldView-2, WVWI, J-Net Dynamic on the VHR image, Sentinel-1, Sentinel-2, Canny and J-Net Dynamic on the HR image

already used in literature (Dominici et al., 2019; Esmail et al., 2019) was followed. Ten transects (Fig. 4.15), one every 100 m drawn from the land to the sea, were used to calculate the intersection between them and the seven shorelines extracted from WorldView-2, WVWI, J-Net Dynamic on the VHR image, Sentinel-1, Sentinel-2, Canny and J-Net Dynamic on the HR image.

Then, the differences between the reference shorelines and the ones extracted from the algorithms were measured. In the end, the mean values and the standard deviations of every difference were calculated (Tab. 4.4).

**Table 4.4.** Statistic table. The means and the standard deviations have been calculated on the difference between the reference shorelines with the tested algorithms. The difference has been calculated on the values obtained from the intersection between the transects and the seven shorelines.

Image	Reference	Algorithm	Mean(m)	St.Dev.(m)
Optical WV-2	Pansharpened image	WVWI	1.87	1.13
		J-Net	1.45	1.12
SAR S1	Sentinel-1 image	Canny	17.21	9.10
		J-Net	10.61	8.21
	Sentinel-2 image	Canny	70.11	29.20
		J-Net	66.09	19.57

As shown in table 4.4, for the VHR image, the standard deviation is

---

1.13 m and the mean is 1.87 considering the common filter. On the other hand, the standard deviation of the J-Net Dynamic is 1.12 m and the mean value 1.45 m. For the HR image, considering the Sentinel-2 optical image as a reference, the results show that the mean value of the difference with the Canny derived shoreline is 70.11 m and the standard deviation is 29.20 m. Compared with the J-Net values, that are 66.09 m and 19.57 m respectively, they are higher. The same happens considering the Sentinel-1 as a reference: the mean values for Canny and J-Net are 17.21 m and 10.61 m and the standard deviations are 9.10 m and 8.21 m, respectively. It can be noticed that the mean and standard deviation are lower for the VHR optical image than the HR SAR image, as expected. Moreover, the values obtained for the SAR image using two different reference shorelines confirm the better results obtained by using the Sentinel-1 image as references, as they were found previously. In fact, the standard deviation for the difference between Sentinel-2 and Canny shorelines is 29.20 m, compared to 9.10 m obtained by the difference between the Sentinel-1 and Canny shorelines. The same happens for the differences between the Sentinel-2 with the J-Net (19.57 m) and Sentinel-1 with the J-Net (8.21 m). Of course, residuals are also affected by the quality of the ground truth. It is not easy, even for a human being, to detect the shoreline in a very accurate way by visual inspection or by GNSS in wide areas in a short time. However, in every case, the J-Net Dynamic gives best accuracy compared to the common filters, as already found out with the index I.

In Maglione et al. (2014), the index I was used to compare the results obtained for the shoreline extraction using the NDVI and the NDWI (Normalized Difference Water Index) filters on the WorldView-2 initial and pansharpened image. It confirms that NDWI application provides better results and that the pan-sharpening enhances geometric resolution and reduces, to less than 1 m, the mean value of shifts between the automatically extracted shoreline and the manually vectorized one. They found an index value of 1.386 m for the multispectral image and 0.955 m for the pan-sharpened one. The better accuracy, compared to the one obtained for the research of this paper, that is, 1.67 m, could be due to the fact that they identified a different threshold to detect the shoreline based on a classifi-

cation method using three contrasting classes (sea, land and vegetation) or due to the fact that the range of shoreline was both sandy and rocky. The rocky parts are less sensitive to instantaneous dynamic change than the sandy ones. The index  $I$  was also considered to evaluate the average shift between two temporal consecutive shorelines (Maglione et al., 2014). They compared shorelines during 2005 and 2011 and they evidenced that the effects of the human intervention, like the installation of breakwaters, limit erosion phenomena near shore zone. This tendency was also found for the years 2011-2012.

The index  $I$  has not been used yet in literature to assess the SAR images. In Spinosa et al. (2018), an automated method of the shoreline position detection using Sentinel-1 SAR image was studied. The method aimed at the automatic extraction of shoreline edge from pre-processed images. The algorithm performs four steps: despeckling, binarisation, morphological operations and edge detection by means of the Canny edge detector. Once the shoreline is extracted, it is compared to the one extracted from the images acquired by video system. The VDS (Video-Derived Shoreline) is a collection of shoreline points. So, the distance between each point from the SDS (Satellite-Derived Shoreline) is calculated in order to evaluate quantitatively the correctness of the SDS position. The average offset turns out to be about 10 m and the Root Mean Square Difference (RMSD) is 12.48 m.

To compare the accuracy with the case study discussed in this paper, the vertices of the reference shoreline (so the shoreline manually outlined on the pre-processed Sentinel-1 image) are extracted and the shortest distance between them and the Canny derived shoreline is calculated. The results show that the average offset is around 16 m, while the standard deviation is 11.40 m. So, a robust contrast can be performed also by applying the binarisation, as proposed by Spinosa et al. (2018), because it splits exactly water and land, and as consequence, the edge detector can easily extract the contour of the image. To increase the accuracy, Demir et al. (2017) propose an integration between RASAT pansharpened image and Sentinel-1 SAR image to improve the quality of the results. The first land/water segmentation was obtained using RASAT image by means of random forest

---

classification method. Then, the result was used as training data set to define fuzzy parameters for shoreline extraction from Sentinel-1A SAR image. The manually digitized shoreline was used as a reference and the accuracy assessment was performed by calculating perpendicular distances between reference data and extracted shoreline by the aforementioned method. The mean distance value between the final result and the reference data was calculated to be 5.59 m, which is half pixel size of Sentinel-1A and which is almost three times better than the results obtained in this research. The higher accuracy was due not only to the integration between optical and SAR images, but also to the fact that the coast considered in Demir et al. (2017) is mainly stony rather than sandy.

Due to the high resolution difference, it would be inappropriate to compare the WorldView-2 optical image and the Sentinel-1 SAR image. The purpose of the research was only to discuss potentiality of the J-Net Dynamic algorithm both in optical and in SAR images independently. So, an additional test was performed. To compare the accuracy with the average offset obtained by means of the Canny edge detector (16 m with an RMSD equal to 11.40), the vertices of the pre-processed Sentinel-1 image shoreline were extracted and the shortest distance between them and the J-Net derived shoreline was calculated. An average offset around 7 m and a standard deviation of 7.36 m were found. The accuracy was lower than one pixel. The values confirm the trend that was delineated by means of the index I value: the algorithm J-Net Dynamic increases the accuracy of the extraction.

[Blank page]

# SECOND CASE STUDY:

## CASTELLDEFELS' COAST

---

### Chapter abstract

Shoreline extraction was conducted also in Castelldefels, a city next to Barcelona (Spain). In this case, optical Sentinel-2 and SAR Sentinel-1 images have been taken into account. The main purpose for this case study was to develop a methodology for the automatic/semi-automatic extraction of the shoreline, focusing on accuracy derived from two different sensors (radar and optical). A set of GPS measurements was taken as reference shoreline and 7 Sentinel-1 images before and after the reference days and four Sentinel-2 images, the closest to the reference days, were downloaded. After the usual pre-processing, the area of interest was cropped and the ACM filter (J-Net Dynamic) was applied. Then, the image was transformed from raster to vector and from vector to lines. At the end, the minimum distance between the line extracted in this way and the reference points, obtained by GPS, was calculated. To be sure that the two images were correctly overlapped, the SAR Sentinel-1 images were coregistered over the optical Sentinel-2 image, before applying the methodology of the extraction. In order to validate the algorithm, comparison with common algorithm used in literature for the same purpose (Canny edge detector) was performed. Good results in terms of accuracy was found both in the comparison between SAR and optical images and between experimental and common algorithms.

## 5.1 Introduction

Combining the information derived from two or more images captured from different sensors is more useful from an interpretation point of view and it could provide better accuracies at the end of the experimentation. Capturing information from the Earth by the energy taken in different portions of the electromagnetic spectrum, helps to acquire complementary information about the studied area. An integration and a fusion of these images is much more helpful compared to the single sensor image data. The field about the integration between two completely different sensors, like SAR and optical, is still being studied. Abdel-Hamid et al. (2018) used SAR data of ALOS/PALSAR, and high resolution optical data of RapidEye to study mangrove ecosystem. They tried to develop an approach to map mangroves extents on the Red Sea coastline in Egypt using Object-Based Image Analysis (OBIA), and testing different machine learning algorithms. They took into account various features of the sensors, such as spectral properties, texture features, and SAR derived parameters for discrimination of mangroves ecosystem classes. They found that the highest overall accuracy (92.15%) was achieved by SAR and optical data integration.

Irwin et al. (2017) proposed the fusion between Synthetic Aperture Radar (SAR) satellite missions, optical satellite-based imagery and airborne light detection and ranging (LIDAR) for surface water detection. Each dataset was independently classified for surface water and then fused. Results show a water classification uncertainty of 4-9% using the fused models compared to 17-23% uncertainty using single polarization SAR.

Amani et al. (2017) used RapidEye, Landsat 8 and Radarsat 2 imagery to study wetland areas by applying object-based method. After the classification, the overall accuracies varied between 81% and 91%, proving the high performance of the methodology in classifying both wetland and non-wetland classes using multi-source data.

In this chapter, shoreline extraction by SAR Sentinel-1 and optical Sentinel-2 sensors is studied in Castelldefels (Barcelona). As aforementioned in chapter 2, Sentinel mission is part of Copernicus programme, which aims to provide long-term sustained, full, open and free data, easily

---

to download and to use. It was expected (and it is) to be exploited in various applications, leading to a potentially change of traditional EO (Earth Observation) paradigms. Sentinel high resolution images, indeed, are already used in many field, like agricultural (Masoud et al., 2020; Torbick et al., 2017; Veloso et al., 2017), for ground deformation caused by landslide or earthquake (Bischoff et al., 2020; Montalti et al., 2019; Xu et al., 2020), ice monitoring (Miles et al., 2017; Tom et al., 2020) and so on.

Providing a semi-automatic methodology to extract the position of the instantaneous shoreline from full, free and high resolution data could help institution to quickly monitor coastal state, in order to promptly intervene in emergency management. It could be also useful for a future study on fusion of the two different sensors.

## 5.2 Dataset

Dataset for the present case study is composed by Sentinel-1 and Sentinel-2 images. Seven Sentinel-1 images were downloaded before the date of interest and seven after (tab. 5.1). In the first column of table 5.1 there are years, months and dates of GPS measurements, which will be used as reference. In the following columns there are, in order, Sentinel-2 and Sentinel-1 acquisition date with the time gap between GPS measurements and satellite images dates. Time is reported in UTC. Sentinel-2 images were always acquired between 10.40 and 10.45 in the morning, while Sentinel-1 between 5.52 and 5.53 in the morning.

**Table 5.1.** Dataset: Sentinel-2 and Sentinel-1 images taken into account for shoreline extraction. The time gap is the number of days between GPS measurements and the date of the images.

<i>Shoreline GPS date</i>	<i>S2 imagery date</i>	<i>Time gap S2 (days)</i>	<i>S1 imagery date</i>	<i>Time gap S1 (days)</i>
2017/05/31, 08h	2017/6/02	2	2017/05/31	0
2017/11/20, 11h	2017/11/19	1	2017/11/21	1
2017/11/23, 16h	2017/11/19	4	2017/11/21	2
2017/11/27, 11h	2017/12/09	12	2017/11/27	0
2017/11/28, 15h	2017/12/09	13	2017/11/27	1
2018/01/17, 15h	2018/01/18	1	2018/01/20	3
2018/01/18, 09h	2018/01/18	0	2018/01/20	2
2018/03/14, 16h	2018/03/14	0	2018/03/15	1
2018/03/19, 13h	2018/03/14	5	2018/03/21	2
2018/03/21, 11h	2018/03/14	7	2018/03/21	0

As it can be seen from table 5.1, the time gap between Sentinel-2 and GPS measurements is, for some days, really high (ranging from 5 to 13 days). This does not happen for Sentinel-1 image. As aforementioned, one of the main disadvantages of optical systems, like Sentinel-2, is that no data are available when there are clouds covering the scene. SAR systems, working in the microwave range of the electromagnetic spectrum, can acquire data during day and night and in every weather conditions. For this reason, Sentinel-2 images with time gap of more than 4 days were discarded from the analysis, as their measures may not correspond to the same situation of the reference data and the results may be compromised. In table 5.2, Sentinel-2 images dates considered for this research are summarized (expressed in year/month/day).

---

**Table 5.2.** Sentinel-2 dataset

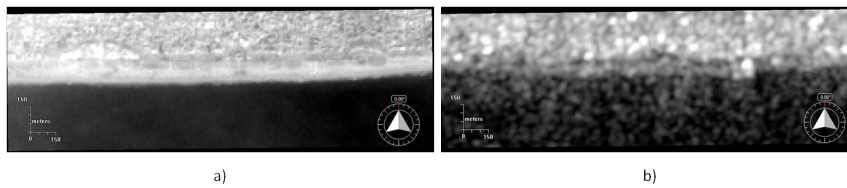
$n^\circ$	Sentinel-2 days of interest (yy/mm/dd)
1	2017/06/02
2	2017/11/19
3	2018/01/18
4	2018/03/14

All Sentinel-1 data, as they are SAR data, can be used, but to maintain consistency with optical data, only the comparable images were considered (tab. 5.3).

**Table 5.3.** Sentinel-1 dataset. In bold, the days of interest, while the others were used to better remove the speckle.

n	Sentinel-1 days of interest (yy/mm/dd)			
1	2017/04/19	2017/10/10	2017/12/09	2018/02/01
2	2017/04/25	2017/10/16	2017/12/15	2018/02/07
3	2017/05/01	2017/10/22	2017/12/21	2018/02/13
4	2017/05/07	2017/10/28	2017/12/27	2018/02/19
5	2017/05/13	2017/11/03	2018/01/02	2018/02/25
6	2017/05/19	2017/11/09	2018/01/08	2018/03/03
7	2017/05/25	2017/11/15	2018/01/14	2018/03/09
8	<b>2017/05/31</b>	<b>2017/11/21</b>	<b>2018/01/20</b>	<b>2018/03/15</b>
9	2017/06/06	2017/11/27	2018/01/26	2018/03/21
10	2017/06/12	2017/12/03	2018/02/01	2018/03/27
11	2017/06/18	2017/12/09	2018/02/07	2018/04/02
12	2017/06/24	2017/12/15	2018/02/13	2018/04/08
13	2017/06/30	2017/12/21	2018/02/19	2018/04/14
14	2017/07/06	2017/12/27	2018/02/25	2018/04/20
15	2017/07/12	2018/01/02	2018/03/03	2018/04/26

Therefore, Sentinel-1 dataset consists in seven images before and seven after the days of interest. This number of images is suitable for speckle reduction, without increasing too much the computational work. In table 5.3, the dates in bold are the central ones used in the experimentation.

**Figure 5.1.** Crops of the original Sentinel-2 a) and Sentinel-1 b) images

In figure 5.1, as example, a crop of two original images (Sentinel-2 taken

on 2018/01/18 and Sentinel-1 taken on 2018/01/20) is shown. Reference system is WGS84/UTM, Zone 31 N (EPSG: 32631).

### 5.3 Pre-processing

In order to remove geometric and radiometric distortion (and speckle filtering in the case of SAR images), pre-processing is needed and it is performed on both Sentinel-1 and Sentinel-2 images.

#### 5.3.1 Sentinel-2

The L2A (Level-2A) Sentinel-2 products were considered and, since the images are already orthorectified and atmospherically corrected using Sen2Cor processor (SNAP tool) and PlanetDEM Digital Elevation Model (DEM), pre-processing consisted in:

1. resampling;
2. creating subset by bands, using only the RGB (2,3,4 bands), NIR (band 8) and SWIR (bands 11 and 12).

Resampling to 10m was performed considering a stack of the bands 2 (blue), 3 (green), 4 (red), 8 (NIR), 11 (SWIR) and 12 (SWIR). Bands with spatial resolution of 60m were not considered due to their not-optimal resampling.

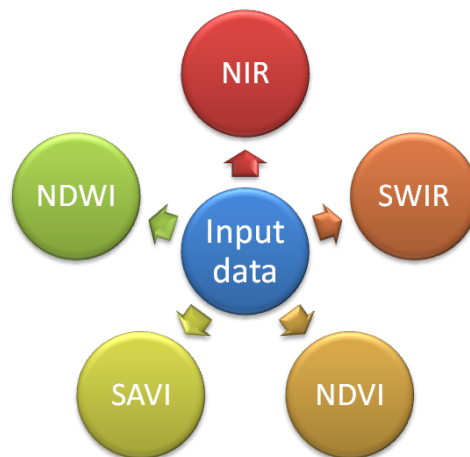


**Figure 5.2.** Sentinel-2 tested input data for Castelldefels shoreline extraction

The chosen bands were appropriately combined to choose the starting point of the experimentation, i.e. the best image for shoreline extraction.

Bands and indices tested as input for the research were NIR, SWIR, NDVI, NDWI (Normalized Difference Water Index) and SAVI (Soil Adjusted Vegetation Index) (Fig. 5.2 and 5.3).

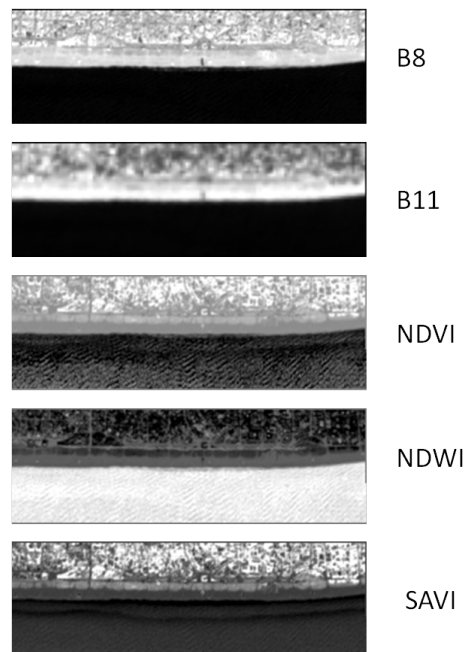


**Figure 5.3.** Sentinel-2 images results tested as input data for Castelldefels shoreline extration

NIR and SWIR are, respectively, band number 8 and 12; NDVI is defined as explained in section 3.3.2, that is the ratio between the difference from NIR and red bands and their sum; NDWI is always a band ratio operation, like NDVI and WVWI (section 3.3.3), but in this case, it considers blue and NIR bands, instead of coastal and NIR, following equation 5.1:

$$NDWI = \frac{BLUE - NIR}{BLUE + NIR} \quad (5.1)$$

SAVI is generally used, as NDVI, to detect vegetated areas but it is more specific in areas where vegetative cover is low (< 40%). It follows equation 5.2

$$SAVI = (1 + L) * \frac{NIR - RED}{NIR + RED + L} \quad (5.2)$$

where “L” is a correction factor which ranges from 0 for very high vegetation cover (it becomes like NDVI equation) to 1 for very low vegetation cover. The most typically used value is 0.5, but it is usually found by trial

and errors. In this case, value 0.5 was used.

As it can be seen from the results in figure 5.3, the best band for this experimentation turns out to be again the NIR (band 8), which visually defined more clearly the separation line between land and water. SWIR band appears more blurry because of the resampling from 20m to 10m, while NDVI, SAVI and NDWI show disturbances on the water, like waves water ripples or double line near to the shore.

### 5.3.2 Sentinel-1

Sentinel-1 images were elaborated as explained in section 4.3.1. Thermal noise removal is the first step and it is applied to remove an additive background energy that causes noise floor, especially in cross-polarization channel. Then, in series, there are application of orbit file, which provides an accurate satellite position and velocity information; calibration, in which pixel value is directly connected to the radar backscatter; coregistration, which aligns all the slaves with the master image, creating a unique image; multi-temporal de-speckle, which aims to reduce speckle effect; in the end, terrain correction, which compensate topographical distortions. The procedure is reported for completeness in figure 5.4.

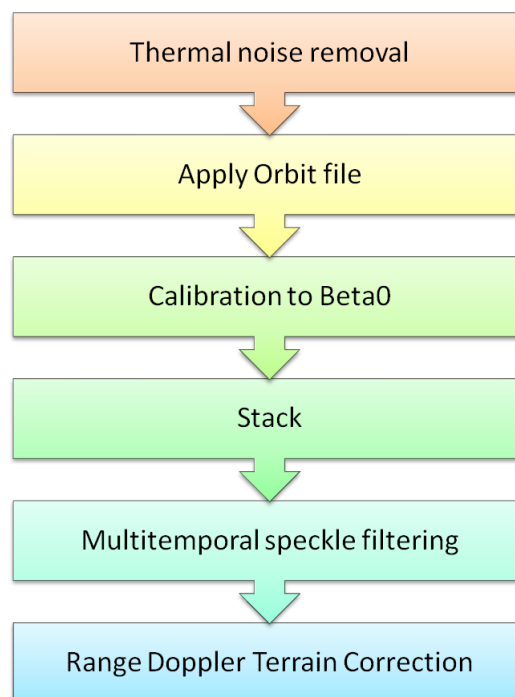


**Figure 5.4.** Sentinel-1 pre-processing steps.

Moreover, decibel band, VH polarization and Lee de-speckle filter were used, according to what was found in chapter 4.

## 5.4 Processing

After the pre-processing, purpose of the research was to find a new methodology to semi-automatically extract the shoreline. Software used for this experimentation is QGIS. At first, Sentinel-2 images were considered and the following procedure developed.

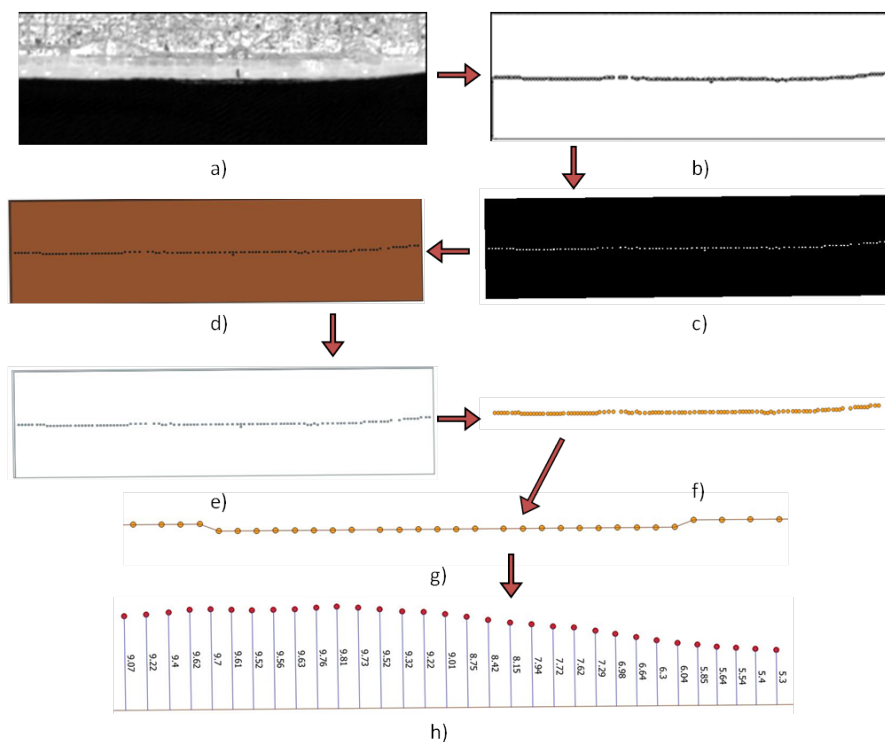


**Figure 5.5.** From the original image to the shoreline extraction: a) Crop of the original NIR band image; b) J-Net Dynamic application; c) Mask of pixels with the same value; d) From raster to vector; e) From vector to line, which are polygons around every pixel; f) From line (polygons) to point; g) Points joined by a line; h) Shorter distance between extracted line and GPS measurements (the measures are expressed in metres).

First step consisted in creating a crop of the image in the area of interest (Fig. 5.5a) by using a buffer of 400m. Secondly, ACM filter was applied, in particular J-Net Dynamic (Fig. 5.5b). Thirdly, pixels with the same value were masked out (Fig. 5.5c), obtaining a binary image which was subsequently converted from raster to vector (Fig. 5.5d), then from vector to line (Fig. 5.5e). The created lines are, actually, polygons around the

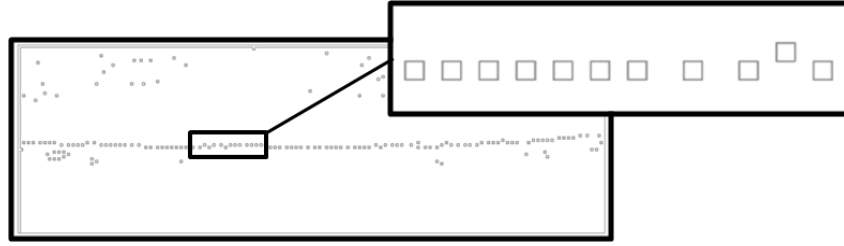


**Figure 5.6.** Zoom on step e) of figure 5.5: the created lines are, actually, polygons around pixels and not a continuous line

pixels and not a continuous line (Fig. 5.6). For this reason, central points (centroid) of these polygons were extracted (Fig. 5.5f) and, consequently, the points were joined to form a continuous line (Fig. 5.5g). Finally, the shortest distance between line and reference points (taken by GPS measurements), was calculated (Fig. 5.5h). In this step, the function used to extract the shortest line was:

```
geom_to_wkt(shortest_line($geometry,geometry(get_feature('line','id','1'))))
```

where “line” was replaced by the name of the line layer, “id” by the attribute to take into account and “1” by the attribute value. The *get\_feature* function allows to recall the geometry of another layer (of line in this case), while *shortest\_line* calculates the shortest line between 2 geometries, so it needs the geometry of the points, which are recalled by \$geometry, and the geometry of the layer to be recalled (line). Finally, *geom\_to\_wkt* permits to transform the geometry in text.

Then, length is calculated by function:

```
length(geom_from_wkt("wkt_short"))
```

where “wkt\_short” is replaced by the name of the attribute previously created.

In the end of the process, a statistical analysis was performed by calculating mean and standard deviation of all the measurements.

Then, the Sentinel-1 image are coregistered on Sentinel-2 and the same procedure was followed with the SAR images. The entire workflow is outlined in figure 5.7.

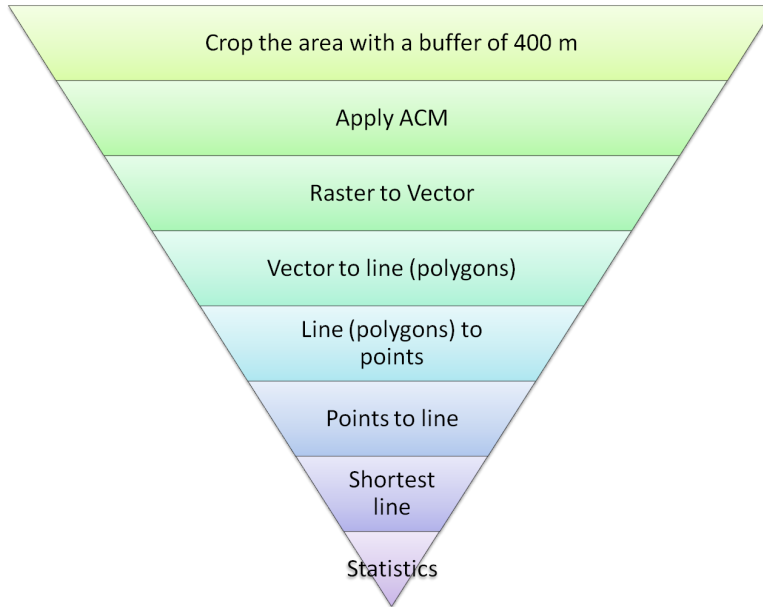


**Figure 5.7.** Semi-automatic methodology chain to extract shorelines

## 5.5 Results and discussion

Second-to-last step of the semi-automatic procedure described in section 5.4 consisted in calculating the shortest distances between Sentinel-1 and Sentinel-2 extracted shorelines with GPS reference points for every considered day. At last, mean and standard deviation were determined. They are reported in table 5.4 for Sentinel-2 and table 5.5 for Sentinel-1.

**Table 5.4.** Mean and standard deviation between Sentinel-2 and GPS reference images in terms of distance by using J-Net Dynamic algorithm

<b>Sentinel-2 / J-Net Dynamic</b>			
<i>Image</i>	<i>GPS Reference</i>	<i>Mean (m)</i>	<i>Standard deviation (m)</i>
2017/06/02	2017/05/31	9.02	3.20
2017/11/19	2017/11/20	6.28	4.79
2017/11/19	2017/11/23	6.01	4.68
2018/01/18	2018/01/17	3.34	2.16
2018/01/18	2018/01/18	3.03	2.39
2018/03/14	2018/03/14	2.15	1.78

As it can be seen from tables 5.4 and 5.5, mean and standard deviation are lower in Sentinel-2 images, as expected. Shorelines extracted from optical images are closer to reference data. SAR images are affected by speckle, which compromise measurements with higher rate. Speckle filtering is still a great topic to be overcome, although there are many approaches and al-

**Table 5.5.** Mean and standard deviation between Sentinel-1 and GPS reference images in terms of distance by using J-Net Dynamic algorithm

<b>Sentinel-1 / J-Net Dynamic</b>			
<i>Image</i>	<i>GPS Reference</i>	<i>Mean (m)</i>	<i>Standard deviation (m)</i>
2017/05/31	2017/05/31	20.96	13.04
2017/11/21	2017/11/20	10.49	6.43
2017/11/21	2017/11/23	10.60	6.91
2018/01/20	2018/01/17	9.34	5.83
2018/01/20	2018/01/18	9.92	6.32
2018/03/15	2018/03/14	15.89	7.93

gorithms that have been implemented (Lee et al., 1994; Lopes et al., 1993; Sivaranjani et al., 2019; Wang et al., 2017).

About Sentinel-2 images, extracted shorelines accuracy is sub-pixel, with a minimum value of  $2.15 \pm 1.78m$  for the last day (2018/03/14) and a maximum value of  $9.02 \pm 3.20m$  for the first day of interest (2017/05/31) and this is a really great result. Despite speckle effects, accuracy achieved by Sentinel-1 ranges from less than 1 to 2 pixels ( $< 10m - 20m$ ), with a minimum value of  $9.34 \pm 5.83m$  for date 2018/01/17 and a maximum value of  $20.96 \pm 13.04m$  for date 2017/05/31. Both from Sentinel-1 and Sentinel-2 imagery, it can be noticed that images compared with more than one GPS reference data, have similar mean values. For example, Sentinel-2 image dated 2017/11/19 was compared to 2017/11/20 and 2017/11/23 GPS dates, obtaining mean values of  $6.28 \pm 4.79m$  and  $6.01 \pm 4.68m$  respectively. The following date, 2018/01/18, was compared to 2018/01/17 and 2018/01/18 GPS dates, providing as result  $3.34 \pm 2.16m$  and  $3.03 \pm 2.39m$ . The same happen for Sentinel-1 image dated on 2017/11/21, which was compared to 2017/11/20 and 2017/11/23 GPS dates and whose values were, respectively,  $10.49 \pm 6.43m$  and  $10.60 \pm 6.91m$ ; about 2018/01/18 image,  $25.43 \pm 9.55m$  and  $24.29 \pm 10.61m$  are mean values obtained comparing satellite image to 2018/01/17 and 2018/01/18 GPS reference data respectively. In both optical and radar images, however, from sub-pixel to 2 pixel accuracy was found, which is a great result for open, free, high resolution satellite images. As reminder, Sentinel-1 images were taken at around 6 a.m., so it was possible to obtain data also during the night.

Currently, it is a standard and good practice to use GPS measurements or video stations as ground truth (Kelly and Gontz, 2018; Maglione et al.,

2015; Ribas et al., 2020), but there is not always the availability of GPS reference, because it is time-consuming and confined to small portions of land. In this case, manually extracted shoreline is used, or extracted from very high resolution multispectral images, after applying pansharpener (Liu et al., 2017), as illustrated in chapter 4. In fact, as explained, the validation is reliable, as well, because the human brain takes into account many contextual parameters, like colours, shapes and textures.

To extract information about instantaneous shoreline position, transect method is generally used and it applies the same concept used for the just presented case study. For example, Vos et al. (2019) calculated erosion/accretion long-term time-series of shoreline changes along the sandy east Australian coastline; similar study was conducted by Syaifulnizam et al. (2018), which used Landsat and SPOT-5 images covering a period for 40 years in Malaysia. In this cases, shoreline position is relative to the others extracted during many years, which is useful to understand the dynamics of past beach behaviour and to calibrate models to predict future changes, but they do not use ground truth to validate the results. This would be good to have accurate and precise measures.

Considering that, in this case study, GPS measurements were acquired, in order to double validate and test the potential of experimental algorithm (J-Net Dynamic) for shoreline extraction, the same methodology was applied by using Canny edge detector, already presented in chapter 4. The results are shown in tables 5.6 and 5.7.

**Table 5.6.** Mean and standard deviation between Sentinel-2 and GPS reference images in terms of distance by using Canny edge detector

<b>Sentinel-2 / Canny</b>			
<i>Image</i>	<i>GPS Reference</i>	<i>Mean (m)</i>	<i>Standard deviation (m)</i>
2017/06/02	2017/05/31	3.15	2.58
2017/11/19	2017/11/20	5.24	3.08
2017/11/19	2017/11/23	5.29	3.20
2018/01/18	2018/01/17	12.68	2.89
2018/01/18	2018/01/18	10.25	3.11
2018/03/14	2018/03/14	10.57	2.79

Canny edge detector proved to be powerful on optical images, achieving minimum mean value of  $3.15 \pm 2.58$ , sub-pixel accuracy, and maximum mean value of  $12.68 \pm 2.89$ . About radar images, minimum mean value is

**Table 5.7.** Mean and standard deviation between Sentinel-1 and GPS reference images in terms of distance by using Canny edge detector

<b>Sentinel-1 / Canny</b>			
<i>Image</i>	<i>GPS Reference</i>	<i>Mean (m)</i>	<i>Standard deviation (m)</i>
2017/06/02	2017/05/31	24.36	9.86
2017/11/19	2017/11/20	7.49	5.03
2017/11/19	2017/11/23	8.15	5.90
2018/01/18	2018/01/17	25.43	9.55
2018/01/18	2018/01/18	24.29	10.61
2018/03/14	2018/03/14	24.03	12.11

$7.49 \pm 5.03$  and maximum mean value is  $24.36 \pm 9.86$ . In both cases, mean values of the same image compared to different GPS measurements are similar, as it happened considering J-Net Dynamic algorithm. Moreover, it can be noticed that Canny is also sensible to speckle effect, providing higher mean values from Sentinel-1 shorelines that the ones from optical images. However, the achieved accuracy is sub-pixel to 1 pixel (10 m) from Sentinel-2 and 1-2 pixels (10 - 20 m) from Sentinel-1 imagery.

All the mean values obtained by using Canny edge detector, therefore, agree with the results obtained by J-Net Dynamic algorithm. About Sentinel-2, they are comparable, ranging between 2 and 10 m. Half mean values are closer to reference data by applying J-Net Dynamic and the other half by applying Canny. The greatest difference can be found on SAR images. In four out of six cases, the experimental algorithm (J-Net Dynamic) discriminates instantaneous shoreline closer to GPS references than common one (Canny). This proves that J-Net Dynamic is less sensitive to speckle and to artefacts present in the image.

To conclude, among the ACM Systems, J-Net Dynamic experimental algorithm demonstrated to extract instantaneous shoreline more accurately than common algorithm Canny edge detector, which is generally used for this purpose, especially on high resolution SAR Sentinel-1 images.

# CONCLUSION

---

## Chapter abstract

In this chapter, conclusions are drawn up. Shoreline extraction was studied both using optical and SAR image, in particular, Very High Resolution (VHR) WorldView-2 and High Resolution (HR) Sentinel-1 and Sentinel-2 satellite images. The main purposes of this research were testing experimental algorithms, never used in remote sensing field, on satellite images, finding a semi-automatic methodology to extract the shoreline, studying the integration between two completely different sensors and checking the results obtained from Copernicus Sentinel mission products. Two test sites were taken into account, one located in the centre of Italy and the other in the North-East of Spain. Reference data was constituted by manually vectorized shoreline using visual inspection for the first case study, and by GPS measurements for the second. In both cases, experimental algorithms, namely ACM Systems, demonstrated to extract the shoreline closer to reference data than common algorithms. The potential of this work consisted also in using mainly full, high resolution and free-of-charge satellite data, Sentinel-1 and Sentinel-2. These data provided, in most of the cases, a sub-pixel accuracy for shoreline extraction, giving, therefore, a good chance to monitor the environment in the most disparate applications over time.

In the presented PhD thesis, the potential of optical and SAR satellite images for shoreline extraction has been studied. Both High and Very High Resolution images have been taken into account, in particular, optical VHR WorldView-2 and HR Sentinel-2 and SAR HR Sentinel-1 sensors.

First case study of this research is located in the centre of Italy (Ortona, Chieti) while the second in the North-East of Spain (Castelldefels, Barcelona). In both cases, experimental algorithms never used on satellite images, called ACM (Active Connection Matrix) Systems were applied and compared to the common ones.

About Italian coast, ACM filter called local Contractive Maps (CM) was tested and compared to the common used NDVI and WWVI on NIR2 band of the optical WorldView-2 satellite image. Three sample distances were taken into account to calculate the distance between shorelines extracted from all the algorithms and reference shoreline, which consisted, in the first case, in the manually vectorised shoreline on the pansharpened image. From the created profiles and the extrapolated values, experimental algorithms proved to be closer to the reference values than the common indices. Then, SAR Sentinel-1 image was studied in the same area. In this case, J-Net Dynamic experimental algorithm was compared to Canny edge detector. J-Net was also applied to WorldView-2 image, in order to link the two experimentations. From the results, both in the optical and in SAR images, J-Net Dynamic extracted a shoreline closer to the reference.

About Spanish coast, the main purpose of the study was to find a semi-automatic methodology to extract the shoreline rapidly. Dataset consisted in optical Sentinel-2 and SAR Sentinel-1 imagery. Also in this case, J-Net Dynamic and Canny edge detector have been tested. Following, images were transformed from raster to vector, vector to line (polygons), line to points, points to continuous line and finally, shortest distance from reference data were calculated. Unlike the first case study, GPS measurements constituted the reference data for Castelldefels coast. The results confirm what was obtained in the first case study: in more than half cases, the ACM System can extract a shoreline closer to GPS reference data than common filter.

From these experiments, the answers to the questions exposed in the

---

introduction of chapter 4 are provided.

At first, some general considerations on the ACM algorithms can be given:

- their ability to define the contours of real images was excellent;
- their adaptation to satellite imagery made them a powerful tool for digital image processing, and they can be used for automatic territory analysis;
- they were capable of distinguishing noise and salient forms within the image;
- they are less sensitive to speckle effect in radar images;
- they can extract the shoreline with sub-pixel accuracy.

So, the new experimental algorithms deriving from machine learning world can be used on satellite remote sensed images for coastal applications.

Other considerations can be done. From the results, the applicability of radar satellite imagery for shoreline extraction is possible, but, sometimes, the backscattering from wet sand is low. This leads to “confuse” wet sand with water, providing a not true extraction. In this case, optical images can come to help, but they cannot give any information during the night or bad weather. So, in this case, SAR satellite images can come to help, because they are not affected by weather or lighting conditions. In this sense, therefore, integration between optical and SAR images can be exploit for greater applicability fields.

Moreover, in this work, a successful semi-automatic procedure to extract the shoreline was found.

To conclude, Copernicus Sentinel-1 and -2 High Resolution images are full, open, free of charge, easy to download and to use, therefore they are important data sources for continuous monitoring. The presented research demonstrated, indeed, that a sub-pixel accuracy can be reached, so they are a successful tool to support management and planning to monitor the position of the shoreline and, as consequence, erosion and accretion in the coastal areas. All these considerations and analysis lead to recommendations and best practices useful for scientific community for shoreline studies.

## 6.1 Future studies

Starting point for future studies is, as natural consequence, optical and SAR data fusion. Definition of image fusion was given by Pohl and Van Genderen (1998): “Image fusion is the combination of two or more different images to create a new image by using a certain algorithm. The main purpose of image fusion is to reach a better and accurate image (output), by integrating and combining different data”. The availability of multitemporal, multiresolution and multifrequency image data has opened the way to image fusion techniques (Mahyoub et al., 2019). One of the most used fusion technique is pansharpen, which was also used in this research to combine WorldView-2 panchromatic with multispectral image, in order to obtain a new enhanced image, with geometric resolution of panchromatic and spectral resolution of multispectral data. One of the most popular topics of recent years is fusion between SAR and optical data. By inheriting all the advantages derived from two completely different sensors, it is possible to have more information and to achieve higher accuracy in final results. SAR images can acquire data all-weather and day and night, it is capable to penetrate clouds. On the other side, optical images are rich in spectral and spatial information.

Fusion between SAR and optical data can be performed by three processing levels (Pohl and Van Genderen, 1998):

- pixel level, where all the fusion processing considers only the pixels of the images and it just requires geocoded and coregistrated data;
- feature level, which requires the extraction of objects, by means of segmentation procedures. Features correspond to characteristics extracted from the original images which depends on their extent, shape and neighbourhood. Similar object (called regions) are recognised in both datasets and fused;
- decision level, which uses individually processed images in order to extract information. Then, it is combined by applying decision rules for a better understanding of the observed objects.

Many studies pointed out that pixel level is unsuitable for optical and

---

SAR images fusion due to speckle noise of SAR and the different work wavelength (Zhang and Xu, 2018; Zhang et al., 2010). It is sometimes used as pre-processing step for the extraction of optical and SAR features (Orynbaikyzy et al., 2020), before applying decision fusion algorithms, which proved to enhance the overall accuracy in the fusion between SAR and optical data, especially in maritime applications (Bioresita et al., 2019).

What this research intends to test in future studies is the fusion of images comparable in terms of resolution, such as Sentinel-1 with Sentinel-2 or WorldView-2 with COSMO-SkyMed products, in order to check the improvement of the accuracy in shoreline extraction.

[Blank page]

# BIBLIOGRAPHY

- Abbas, A. W., Minallh, N., Ahmad, N., Abid, S. A. R., and Khan, M. A. A. (2016). K-Means and ISODATA clustering algorithms for landcover classification using remote sensing. *Sindh University Research Journal-SURJ (Science Series)*, 48(2).
- Abdel-Hamid, A., Dubovyk, O., El-Magd, A., Menz, G., et al. (2018). Mapping mangroves extents on the Red Sea coastline in Egypt using polarimetric SAR and high resolution optical remote sensing data. *Sustainability*, 10(3):646.
- Abdi, H. and Williams, L. J. (2010). Principal component analysis. *Wiley interdisciplinary reviews: computational statistics*, 2(4):433–459.
- Addabbo, P., Focareta, M., Marcuccio, S., Votto, C., and Ullo, S. L. (2016). Contribution of Sentinel-2 data for applications in vegetation monitoring. *ACTA IMEKO*, 5(2):44–54.
- Alesheikh, A. A., Ghorbanali, A., and Nouri, N. (2007). Coastline change detection using remote sensing. *International Journal of Environmental Science & Technology*, 4(1):61–66.
- Alexakis, D., Daliakopoulos, I., Panagea, I., and Tsanis, I. (2018). Assessing soil salinity using WorldView-2 multispectral images in Timpaki, Crete, Greece. *Geocarto International*, 33(4):321–338.
- Alley, R. (1999). Algorithm theoretical basis document for: decorrelation stretch. *JPL Publication ATBD-AST-06*.
- Amani, M., Salehi, B., Mahdavi, S., Granger, J., and Brisco, B. (2017). Wetland classification in Newfoundland and Labrador using multi-source

- SAR and optical data integration. *GIScience & Remote Sensing*, 54(6):779–796.
- American Heritage Dictionary of the English Language (2016). The free dictionary. Houghton Mifflin Harcourt Publishing Company, <https://www.thefreedictionary.com/shoreline>, accessed 2020-03-23.
- Apostolopoulos, D. and Nikolakopoulos, K. (2020). Assessment and quantification of the accuracy of low-and high-resolution remote sensing data for shoreline monitoring. *ISPRS International Journal of Geo-Information*, 9(6):391.
- ASI, I. (n.d.). COSMO-SkyMed, Sistema duale per l'osservazione della Terra. <https://www.asi.it/scienze-della-terra/cosmo-skymed/>, accessed 2020-09-12.
- Asokan, A., Anitha, J., Ciobanu, M., Gabor, A., Naaji, A., and Hemanth, D. (2020). Image processing techniques for analysis of satellite images for historical maps classificationan overview. *Applied Sciences*, 10(12):4207.
- Ataol, M., Kale, M., and Tekkanat, İ. (2019). Assessment of the changes in shoreline using digital shoreline analysis system: a case study of Kızılırmak Delta in northern Turkey from 1951 to 2017. *Environmental Earth Sciences*, 78(19):579.
- Bagli, S., Soille, P., and Fermi, E. (2004). Automatic delineation of shoreline and lake boundaries from Landsat satellite images. *Proceedings of initial ECO-IMAGINE GI and GIS for Integrated Coastal Management, Seville*, pages 13–15.
- Baiocchi, V., Brigante, R., Dominici, D., and Radicioni, F. (2011). Individuazione della linea di costa mediante immagini satellitari multispettrali ad alta risoluzione. In *Atti 15a Conferenza Nazionale ASITA*, pages 183–193, Reggio di Colorno.
- Baiocchi, V., Dominici, D., Ialongo, R., Milone, M. V., and Mormile, M. (2013). DSMs extraction methodologies from EROS-B pseudo-stereopairs, PRISM stereopairs in coastal and post-seismic areas. In *In-*

- 
- ternational Conference on Computational Science and Its Applications*, pages 136–149. Springer.
- Bao, G., Qin, Z., Bao, Y., Zhou, Y., Li, W., and Sanjjav, A. (2014). NDVI-based long-term vegetation dynamics and its response to climatic change in the Mongolian Plateau. *Remote Sensing*, 6(9):8337–8358.
- Battagliere, M., Virelli, M., Lenti, F., Lauretta, D., and Coletta, A. (2019). A Review of the Exploitation of the Operational Mission COSMO-SkyMed: Global Trends (2014-2017). *Space Policy*, 48:60–67.
- Belgian Earth Observation (n.d.). Geometric and radiometric corrections. <https://eo.belspo.be/en/geometric-and-radiometric-corrections>, (accessed 2020-05-21).
- Bianco, F., Conti, P., García-Ayllon, S., and Pranzini, E. (2020). An Integrated Approach to Analyze Sedimentary Stock and Coastal Erosion in Vulnerable Areas: Resilience Assessment of San Vicenzos Coast (Italy). *Water*, 12(3):805.
- Bioresita, F., Puissant, A., Stumpf, A., and Malet, J. (2019). Fusion of Sentinel-1 and Sentinel-2 image time series for permanent and temporary surface water mapping. *International Journal of Remote Sensing*, 40(23):9026–9049.
- Bischoff, C. A., Ferretti, A., Novali, F., Uttini, A., Giannico, C., and Meloni, F. (2020). Nationwide deformation monitoring with SqueeSAR® using Sentinel-1 data. *Proceedings of the International Association of Hydrological Sciences*, 382:31–37.
- Blunden, J. and Arndt, D. S. (2019). State of the climate in 2018. *Bulletin of The American Meteorological Society-(BAMS)*, 100(9):S1–S305.
- Boak, E. H. and Turner, I. L. (2005). Shoreline definition and detection: a review. *Journal of coastal research*, pages 688–703.
- Boccardo, P., Mondino, E. B., Tonolo, F. G., and Lingua, A. (2004). Orthorectification of high resolution satellite images. *Politecnico di Torino, Dipartimento di Georisorse e Territorio, Torino-Italy*.

- Bodansky, E., Gribov, A., and Pilouk, M. (2001). Smoothing and compression of lines obtained by raster-to-vector conversion. In *International Workshop on Graphics Recognition*, pages 256–265. Springer.
- Bonaldo, D., Antonioli, F., Archetti, R., Bezzi, A., Correggiari, A., Davolio, S., De Falco, G., Fantini, M., Fontolan, G., Furlani, S., et al. (2019). Integrating multidisciplinary instruments for assessing coastal vulnerability to erosion and sea level rise: lessons and challenges from the Adriatic Sea, Italy. *Journal of coastal conservation*, 23(1):19–37.
- Bovenga, F., Wasowski, J., Nitti, D., Nutricato, R., and Chiaradia, M. (2012). Using COSMO/SkyMed X-band and ENVISAT C-band SAR interferometry for landslides analysis. *Remote Sensing of Environment*, 119:272–285.
- Braga, F., Tosi, L., Prati, C., and Alberotanza, L. (2013). Shoreline detection: Capability of COSMO-SkyMed and high-resolution multispectral images. *European Journal of Remote Sensing*, 46(1):837–853.
- Brivio, P., Lechi, G., and Zilioli, E. (2006). *Principi e metodi di telerilevamento*. Cittàstudi edition.
- Brown, J. (2020). SAR 101: An Introduction to Synthetic Aperture Radar. <https://www.capellaspace.com/sar-101-an-introduction-to-synthetic-aperture-radar/>, accessed 2020-05-12.
- Bruno, M., Molfetta, M., Mossa, M., Nutricato, R., Morea, A., and Chiaradia, M. (2016). Coastal observation through Cosmo-SkyMed high-resolution SAR images. *Journal of Coastal Research*, (75):795–799.
- Buscema, P. (n.d.). Acn Batch, Semeion Software 33. [www.semeion.it](http://www.semeion.it), accessed 2018-06-04.
- Buscema, P. M. (2006). *Sistemi ACM e Imaging Diagnostico: le immagini mediche come Matrici Attive di Connessioni*. Springer Science & Business Media.
- Buscema, P. M., Catzola, L., and Grossi, E. (2008). Images as active connection matrixes: The J-net system. *International Journal of Intelligent Computing in Medical Sciences & Image Processing*, 2(1):27–53.

- 
- Buscema, P. M. and Grossi, E. (2010). J-Net System: A New Paradigm for Artificial Neural Networks Applied to Diagnostic Imaging. In *Applications of Mathematics in Models, Artificial Neural Networks and Arts*, pages 431–455. Springer.
- Buscema, P. M., Passariello, R., Grossi, E., Massini, G., Fraioli, F., and Serra, G. (2013). J-Net: An Adaptive System for Computer-Aided Diagnosis in Lung Nodule Characterization. In *Data Mining Applications Using Artificial Adaptive Systems*, pages 25–61. Springer.
- Canny, J. (1986). A computational approach to edge detection. *IEEE Transactions on pattern analysis and machine intelligence*, (6):679–698.
- Carli, S., Cipriani, L. E., Bresci, D., Danese, C., Iannotta, P., Pranzini, E., Rossi, L., and Wetzell, L. (2004). Tecniche di monitoraggio dell’evoluzione delle spiagge. *REGIONE TOSCANA. Il Piano Regionale di gestione integrata della costa ai fini del riassetto idrogeologico. Erosione costiera. Firenze: EDIFIR*, pages 125–192.
- Chan, Y. K. and Koo, V. C. (2008). An introduction to synthetic aperture radar (SAR). *Progress In Electromagnetics Research*, 2:27–60.
- Chaturvedi, S. K., Banerjee, S., and Lele, S. (2019). An assessment of oil spill detection using Sentinel-1 SAR-C images. *Journal of Ocean Engineering and Science*.
- Cheng, Y., Liu, B., Li, X., Nunziata, F., Xu, Q., Ding, X., Migliaccio, M., and Pichel, W. (2014). Monitoring of oil spill trajectories with COSMO-SkyMed X-band SAR images and model simulation. *IEEE Journal of Selected Topics in Applied Earth Observations and Remote Sensing*, 7(7):2895–2901.
- Church, J. A. and White, N. J. (2011). Sea-Level Rise from the Late 19th to the Early 21st Century. *Surveys in Geophysics*, 32(4-5):585–602. <http://link.springer.com/10.1007/s10712-011-9119-1>, accessed 2020-05-05.
- Comini, G., Croce, G., and Savino, S. (2011). *Energetica generale*, chapter 4, page 118. S.G.E, 5 edition.

- Congedo, L. (2012-2020). Brief introduction to remote sensing. [https://semiautomaticclassificationmanual.readthedocs.io/en/latest/remote\\_sensing.html](https://semiautomaticclassificationmanual.readthedocs.io/en/latest/remote_sensing.html), accessed 2020-11-09.
- Cozzolino, D., Di Martino, G., Poggi, G., and Verdoliva, L. (2017). A fully convolutional neural network for low-complexity single-stage ship detection in Sentinel-1 SAR images. In *2017 IEEE International Geoscience and Remote Sensing Symposium (IGARSS)*, pages 886–889. IEEE.
- CRISP, C. (2001). Principles of Remote Sensing - Centre for Remote Imaging, Sensing and Processing, CRISP. <https://crisp.nus.edu.sg/~research/tutorial/optical.htm>, accessed 2020-05-19.
- Crowell, M., Douglas, B. C., and Leatherman, S. P. (1997). On forecasting future us shoreline positions: a test of algorithms. *Journal of Coastal Research*, pages 1245–1255.
- Dammann, D. O., Eriksson, L. E., Mahoney, A. R., Eicken, H., and Meyer, F. J. (2019). Mapping pan-Arctic landfast sea ice stability using Sentinel-1 interferometry. *The Cryosphere*, 13(2):557–577.
- Dave, C. P., Joshi, R., and Srivastava, S. (2015). A survey on geometric correction of satellite imagery. *International Journal of Computer Applications*, 116(12).
- De Agostini, A. and Floris, M. (2014). *L'utilizzo dell'interferometria radar satellitare nella caratterizzazione dei fenomeni franosi a differenti scale d'indagine*. Phd thesis, Geoscience department UNIPD. Dipartimento di Geoscienze - Scuola di Dottorato in Scienze della Terra, UNIPD, <http://paduaresearch.cab.unipd.it/6276/>, (accessed 2020-05-12).
- Dechesne, C., Lefèvre, S., Vadaine, R., Hajduch, G., and Fablet, R. (2019). Multi-task deep learning from Sentinel-1 SAR: ship detection, classification and length estimation. In *BiDS19: Conference on Big Data from Space*, Munich, Germany.
- Delwart, S. (2015). ESA Standard Document. (1):64.
- Demir, N., Bayram, B., Şeker, D., Oy, S., İnce, A., and Bozkurt, S. (2019).

- 
- Advanced lake shoreline extraction approach by integration of sar image and lidar data. *Marine Geodesy*, 42(2):166–185.
- Demir, N., Kaynarca, M., and Oy, S. (2016). Extraction of coastlines with fuzzy approach using sentinel-1 sar image. *The International Archives of Photogrammetry, Remote Sensing and Spatial Information Sciences*, 41:747.
- Demir, N., Oy, S., Erdem, F., Şeker, D., and Bayram, B. (2017). Integrated shoreline extraction approach with use of Rasat MS and Sentinel-1A SAR Images. *ISPRS Annals of the Photogrammetry, Remote Sensing and Spatial Information Sciences*, 4:445.
- Dermanis, A. and Biagi, L. G. A. (2002). *Il telerilevamento, informazione territoriale mediante immagini da satellite*. CEA.
- Deutscher, J., Perko, R., Gutjahr, K., Hirschmugl, M., and Schardt, M. (2013). Mapping tropical rainforest canopy disturbances in 3D by COSMO-SkyMed spotlight InSAR-stereo data to detect areas of forest degradation. *Remote sensing*, 5(2):648–663.
- Di, K., Wang, J., Ma, R., and Li, R. (2003). Automatic shoreline extraction from high-resolution IKONOS satellite imagery. In *Proceeding of ASPRS 2003 Annual Conference*, volume 3.
- DigitalGlobe (2009). Worldview-2 overview. [http://satimagingcorp.s3.amazonaws.com/site/pdf/WorldView\\_2\\_Overview.pdf](http://satimagingcorp.s3.amazonaws.com/site/pdf/WorldView_2_Overview.pdf), accessed 2018-05-16.
- Domaradzki, P. (n.d.). Why monitor coastal erosion and accretion? (26):6. <http://www.vliz.be/projects/deduce/IFS/IFS26.pdf>, accessed 2020-06-01.
- Dominici, D., Feltrami, G., and De Girolamo, P. (2006). Ortorettifica di immagini satellitari ad alta risoluzione finalizzata al monitoraggio costiero a scala regionale. *Studi Costieri, Studi Costieri*, 11:145–146.
- Dominici, D., Zollini, S., Alicandro, M., Della Torre, F., Buscema, P. M., and Baiocchi, V. (2019). High resolution satellite images for instan-

- taneous shoreline extraction using new enhancement algorithms. *Geosciences*, 9(3):123.
- Dowman, I. and Tao, V. (2002). An update on the use of rational functions for photogrammetric restitution. *ISPRS Highlights*, 7(3):22–29.
- Drusch, M., Del Bello, U., Carlier, S., Colin, O., Fernandez, V., Gascon, F., Hoersch, B., Isola, C., Laberinti, P., Martimort, P., et al. (2012). Sentinel-2: ESA’s optical high-resolution mission for GMES operational services. *Remote sensing of Environment*, 120:25–36.
- e Geos (n.d.). COSMO-SkyMed, the most advanced SAR constellation. <https://www.e-geos.it/#/satellite-hub/general/satellite-detail/csk>, accessed 2020-09-12.
- Eichel, P., Ghiglia, D., and Jakowatz, C. (1989). Speckle processing method for synthetic-aperture-radar phase correction. *Optics letters*, 14(1):1–3.
- El Hajj, M., Baghdadi, N., Zribi, M., and Bazzi, H. (2017). Synergic use of Sentinel-1 and Sentinel-2 images for operational soil moisture mapping at high spatial resolution over agricultural areas. *Remote Sensing*, 9(12):1292.
- ESA, European Space Agency (2020a). PRISMA (Hyperspectral Precursor and Application Mission). <https://directory.eoportal.org/web/eoportal/satellite-missions/p/prisma-hyperspectral>, accessed 2020-10-03.
- ESA, European Space Agency (2020b). Radar course 3, image interpretation. [https://earth.esa.int/web/guest/missions/esa-operational-eo-missions/ers/instruments/sar/applications/radar-courses/content-3/-/asset\\_publisher/mQ9R7ZVkJg5P/content/radar-course-3-image-interpretation-tone](https://earth.esa.int/web/guest/missions/esa-operational-eo-missions/ers/instruments/sar/applications/radar-courses/content-3/-/asset_publisher/mQ9R7ZVkJg5P/content/radar-course-3-image-interpretation-tone), accessed 2020-05-18.
- ESA, European Space Agency (n.d.a). Copernicus Open Access Hub. <https://scihub.copernicus.eu/dhus/#/home>, accessed 2019-05-22.
- ESA, European Space Agency (n.d.b). COSMO-SkyMed (Constellation of 4 SAR Satellites). <https://earth.esa.int/web/eoportal/satellite->

---

missions/c-missions/cosmo-skymed#:~:text=COsmo%2DSkyMed%  
20(Constellation%20of%20Small,MoD)%2C%20Rome%2C%20Italy.,  
accessed 2020-09-12.

ESA, European Space Agency (n.d.c). Home, User Guides, Sentinel-1 SAR, Acquisition Modes, Interferometric Wide Swath. <https://sentinel.esa.int/web/sentinel/user-guides/sentinel-1-sar/acquisition-modes/interferometric-wide-swath>, accessed 2019-05-24.

ESA, European Space Agency (n.d.d). Home, User Guides, Sentinel-1 SAR, Overview, Polarimetry. <https://sentinel.esa.int/web/sentinel/user-guides/sentinel-1-sar/product-overview/polarimetry>, accessed 2019-05-22.

ESA, European Space Agency (n.d.e). Home, User Guides, Sentinel-1 SAR, Product Types and Processing Levels, Level-1. <https://sentinel.esa.int/web/sentinel/user-guides/sentinel-1-sar/producttypes-processing-levels/level-1>, accessed 2019-05-22.

ESA, European Space Agency (n.d.f). Orbit - Sentinel-1 - Sentinel Handbook. <https://sentinel.esa.int/web/sentinel/missions/sentinel-1/satellite-description/orbit>, accessed 2020-05-19.

ESA, European Space Agency (n.d.g). Resolution and Swath - Sentinel-1 - Missions - Sentinel Online. <https://sentinel.esa.int/web/sentinel/missions/sentinel-1/instrument-payload/resolution-swath>, accessed 2020-05-19.

ESA, European Space Agency (n.d.h). Sentinel-1 - Data Distribution Schedule - Missions - Sentinel Online. <https://sentinel.esa.int/web/sentinel/missions/sentinel-1/data-distribution-schedule>, accessed 2020-05-19.

ESA, European Space Agency (n.d.i). Sentinel-1 - Data Products - Sentinel Online. <https://sentinel.esa.int/web/sentinel/missions/sentinel-1/data-products>, urldate = 2020-05-19, accessed 2020-05-19.

ESA, European Space Agency (n.d.j). Sentinel-1 - Instrument Payload - Sentinel Online. <https://sentinel.esa.int/web/sentinel/missions/sentinel-1/instrument-payload>, accessed 2020-05-19.

ESA, European Space Agency (n.d.k). Sentinel-1 - Overview - Sentinel Online. <https://sentinel.esa.int/web/sentinel/missions/sentinel-1/overview>, accessed 2020-05-19.

ESA, European Space Agency (n.d.l). Sentinel-1- Observation Scenario - Planned Acquisitions - ESA. <https://sentinel.esa.int/web/sentinel/missions/sentinel-1/observation-scenario>, accessed 2020-05-19.

ESA, European Space Agency (n.d.m). Sentinel-2 - Data Products - Sentinel Handbook. <https://sentinel.esa.int/web/sentinel/missions/sentinel-2/data-products>, accessed 2020-05-26.

ESA, European Space Agency (n.d.n). Sentinel-2 - Missions - Resolution and Swath - Sentinel Handbook. <https://sentinel.esa.int/web/sentinel/missions/sentinel-2/instrument-payload/resolution-and-swath>, accessed 2020-05-22.

ESA, European Space Agency (n.d.o). Sentinel-2 - Overview - Sentinel Online. <https://sentinel.esa.int/web/sentinel/missions/sentinel-2/overview>, accessed 2020-05-21.

ESA, European Space Agency (n.d.p). User Guides - Sentinel-1 SAR - Level-1 Ground Range Detected - Sentinel Online. <https://sentinel.esa.int/web/sentinel/user-guides/sentinel-1-sar/resolutions/level-1-ground-range-detected>, accessed 2020-05-09.

ESA, European Space Agency (n.d.q). User Guides - Sentinel-1 SAR - Level-1 Single Look Complex - Sentinel Online. <https://sentinel.esa.int/web/sentinel/user-guides/sentinel-1-sar/resolutions/level-1-single-look-complex>, accessed 2020-05-19.

---

ESA, European Space Agency (n.d.r). User Guides - Sentinel-1 SAR - Level-2 Ocean - Sentinel Online. <https://sentinel.esa.int/web/sentinel/user-guides/sentinel-1-sar/resolutions/level-2-ocean>, accessed 2020-05-19.

ESA, European Space Agency (n.d.s). User Guides - Sentinel-2 MSI - Revisit and Coverage - Sentinel Online. <https://sentinel.esa.int/web/sentinel/user-guides/sentinel-2-msi/revisit-coverage>, accessed 2020-05-26.

Esmail, M., Mahmood, W. E., and Fath, H. (2019). Assessment and prediction of shoreline change using multi-temporal satellite images and statistics: case study of Damietta coast, Egypt. *Applied Ocean Research*, 82:274–282.

European Environment Agency (2004). Coastline dynamics in Europe. <https://www.eea.europa.eu/data-and-maps/figures/coastal-erosion-patterns-in-europe-1>, accessed 2020-05-02.

Ferretti, O., Barsanti, M., Delbono, I., and Furia, S. (2003). Elementi di gestione costiera—Parte II: Erosione Costiera. Lo stato dei litorali italiani. *ENEA, Earth Science Department (Parma University) and Marine Environment Research Center (La Spezia)*.

Filippini, F. (2019). Sentinel-1 GRD Preprocessing Workflow. In *Multidisciplinary Digital Publishing Institute Proceedings*, volume 18, page 11.

Forkuor, G., Zoungrana, J. B., Dimobe, K., Ouattara, B., Vadrevu, K. P., and Tondoh, J. E. (2020). Above-ground biomass mapping in West African dryland forest using Sentinel-1 and 2 datasets-A case study. *Remote Sensing of Environment*, 236:111496.

Gandhi, G. M., Parthiban, S., Thummalu, N., and Christy, A. (2015). NDVI: Vegetation change detection using remote sensing and GIS – A case study of Vellore District. *Procedia Computer Science*, 57:1199–1210.

Gens, R. (2010). Remote sensing of coastlines: detection, extraction and monitoring. *International Journal of Remote Sensing*, 31(7):1819–1836.

- Gianinetto, M. (n.d.). Cartografia da satellite. *Politecnico di Milano, Master Universitario in Protezione Civile*.
- Gobbi, S., Maimeri, G., Tattoni, C., Tattoni, M., Cantiani, M., Rocchini, D., La Porta, N., Ciolli, M., and Zatelli, P. (2018). Orthorectification of a large dataset of historical aerial images: procedure and precision assessment in an open source environment. *International Archives of the Photogrammetry, Remote Sensing & Spatial Information Sciences*, 42.
- Gomarasca, M. A. (2009). *Basics of geomatics*. Springer Science & Business Media.
- Gonçalves, G., Duro, N., Sousa, E., and Figueiredo, I. (2015). Automatic extraction of tide-coordinated shoreline using open source software and Landsat imagery. *The International Archives of Photogrammetry, Remote Sensing and Spatial Information Sciences*, 40(7):953.
- Gonçalves, J. and Henriques, R. (2015). UAV photogrammetry for topographic monitoring of coastal areas. *ISPRS Journal of Photogrammetry and Remote Sensing*, 104:101–111.
- Guastaferrò, F., Maglione, P., Parente, C., and Santamaria, R. (2011). Estrazione in automatico della linea di costa da immagini satellitari IKONOS. In *Proceedings of the conference Geomatica. Le radici del futuro. Tributo a Sergio Degual & Riccardo Galetto, Pavia*, pages 109–116.
- Han, Y., Feng, X.-C., Baciù, G., and Wang, W.-W. (2013). Nonconvex sparse regularizer based speckle noise removal. *Pattern recognition*, 46(3):989–1001.
- Harley, M. D., Turner, I. L., Short, A. D., and Ranasinghe, R. (2011). Assessment and integration of conventional, RTK-GPS and image-derived beach survey methods for daily to decadal coastal monitoring. *Coastal Engineering*, 58(2):194–205.
- Hastings, J. T. and Hill, L. L. (2009). *Georeferencing*, pages 1246–1249. Springer US, Boston, MA. [https://doi.org/10.1007/978-0-387-39940-9\\_181](https://doi.org/10.1007/978-0-387-39940-9_181), accessed 2020-09-15.

- 
- Hexagon Geospatial (2015a). *Planetek, ERDAS IMAGINE Software, PRODUCER Suite of Power Portfolio by Hexagon Geospatial*. ERDAS IMAGINE, Hexagon Geospatial.
- Hexagon Geospatial (2015b). *Planetek, ERDAS IMAGINE TourGuide, PRODUCER Suite of Power Portfolio by Hexagon Geospatial*. ERDAS IMAGINE, Hexagon Geospatial.
- Holman, R. A. and Stanley, J. (2007). The history and technical capabilities of Argus. *Coastal engineering*, 54(6-7):477–491.
- Humboldt State University (2014). Spectral enhancements. [http://gsp.humboldt.edu/OLM/Courses/GSP\\_216\\_Online/lesson5-1/spectral.html](http://gsp.humboldt.edu/OLM/Courses/GSP_216_Online/lesson5-1/spectral.html), (accessed 2020-10-21).
- Humboldt State University (2019a). Composites. [http://gsp.humboldt.edu/OLM/Courses/GSP\\_216\\_Online/lesson3-1/composites.html](http://gsp.humboldt.edu/OLM/Courses/GSP_216_Online/lesson3-1/composites.html), (accessed 2020-05-19).
- Humboldt State University (2019b). Image Bands. [http://gsp.humboldt.edu/OLM/Courses/GSP\\_216\\_Online/lesson3-1/bands.html](http://gsp.humboldt.edu/OLM/Courses/GSP_216_Online/lesson3-1/bands.html), (accessed 2020-05-19).
- Humboldt State University (2019c). Resolution. [http://gsp.humboldt.edu/OLM/Courses/GSP\\_216\\_Online/lesson3-1/resolution.html](http://gsp.humboldt.edu/OLM/Courses/GSP_216_Online/lesson3-1/resolution.html), accessed 2020-03-17.
- Humboldt State University, GSP216 (2014). Introduction to remote sensing - pan sharpening. [http://gsp.humboldt.edu/OLM/Courses/GSP\\_216\\_Online/lesson4-1/pan-sharpen.html](http://gsp.humboldt.edu/OLM/Courses/GSP_216_Online/lesson4-1/pan-sharpen.html), accessed 2020-10-20.
- Ietto, F., Cantasano, N., and Pellicone, G. (2018). A new coastal erosion risk assessment indicator: application to the Calabria tyrrhenian littoral (southern Italy). *Environmental Processes*, 5(2):201–223.
- Immitzer, M., Atzberger, C., and Koukal, T. (2012). Tree species classification with random forest using very high spatial resolution 8-band WorldView-2 satellite data. *Remote Sensing*, 4(9):2661–2693.

- Irwin, K., Beaulne, D., Braun, A., and Fotopoulos, G. (2017). Fusion of SAR, optical imagery and airborne LiDAR for surface water detection. *Remote Sensing*, 9(9):890.
- ISPRA - Istituto Superiore per la Prevenzione e la Ricerca Ambientale (2011). Mare e Ambiente Costiero. <http://www.isprambiente.gov.it/it/pubblicazioni/stato-dellambiente/tematiche-in-primo-pianoannuario-dei-dati-ambientali-2011>, accessed 2016-10-17.
- ISPRA - Istituto Superiore per la Prevenzione e la Ricerca Ambientale (2014). Mare e Ambiente Costiero. <http://www.isprambiente.gov.it/it/pubblicazioni/stato-dellambiente/tematiche-in-primo-piano-annuario-dei-dati-ambientali-2014-2015>, accessed 2016-10-17.
- Japan Association of Remote Sensing (1996). 9.1 Radiometric Correction. <http://wtlab.iis.u-tokyo.ac.jp/wataru/lecture/rsgis/rsnote/cp9/cp9-1.htm>, accessed 2020-05-20.
- Jiang, A., Chen, F., Masini, N., Capozzoli, L., Romano, G., Sileo, M., Yang, R., Tang, P., Chen, P., Lasaponara, R., et al. (2017). Archeological crop marks identified from Cosmo-SkyMed time series: the case of Han-Wei capital city, Luoyang, China. *International Journal of Digital Earth*, 10(8):846–860.
- Jog, S. and Dixit, M. (2016). Supervised classification of satellite images. In *2016 Conference on Advances in Signal Processing (CASP)*, pages 93–98. IEEE.
- Kelly, J. and Gontz, A. (2018). Using GPS-surveyed intertidal zones to determine the validity of shorelines automatically mapped by Landsat water indices. *International journal of applied earth observation and geoinformation*, 65:92–104.
- Konishi, T. and Suga, Y. (2018). Landslide detection using COSMO-SkyMed images: a case study of a landslide event on Kii Peninsula, Japan. *European journal of remote sensing*, 51(1):205–221.

- 
- Konstantinidou, E. E., Kolokoussis, P., Topouzelis, K., and Moutzouris-Sidiris, I. (2019). An open source approach for oil spill detection using Sentinel-1 SAR images. In *Seventh International Conference on Remote Sensing and Geoinformation of the Environment (RSCy2019)*, volume 11174, page 1117412. International Society for Optics and Photonics.
- Kramer, H. J. (2002a). *Observation of the earth and its environment: survey of missions and sensors*. Springer Science & Business Media.
- Kramer, H. J. (2002b). WorldView-2 - eoPortal Directory - Satellite Missions. <https://earth.esa.int/web/eoportal/satellite-missions/v-w-x-y-z/worldview-2>, accessed 2020-04-24.
- Kratochvilova, A. and Petras, V. (2003-2020). GRASS Manual. <https://grass.osgeo.org/grass76/manuals/addons/i.edge.html>, accessed 2019-07-05.
- L3Harris Geospatial (n.d.). Docs Center, Using ENVI, Decorrelation Stretch. <https://www.l3harrisgeospatial.com/docs/DecorrelationStretch.html>, accessed 2020-10-21.
- Lanari, R., Berardino, P., Bonano, M., Casu, F., Manconi, A., Manunta, M., Manzo, M., Pepe, A., Pepe, S., Sansosti, E., et al. (2010). Surface displacements associated with the L'Aquila 2009 Mw 6.3 earthquake (central Italy): New evidence from SBAS-DInSAR time series analysis. *Geophysical Research Letters*, 37(20).
- Land Info (2014-2018). Worldview-2 50cm global high-resolution satellite imagery. <http://www.landinfo.com/WorldView2.htm>, accessed 2020-06-2018.
- Lasalandra, M. G. (2009). Metodologia per la mappatura delle spiagge e della dinamica litoranea mediante la classificazione di immagini digitali. [http://www.isprambiente.gov.it/contentfiles/00004400/4488-lasalandra.zip/at\\_download/file](http://www.isprambiente.gov.it/contentfiles/00004400/4488-lasalandra.zip/at_download/file), accessed 2017-01-23.
- Lee, I.-C., Wu, B., and Li, R. (2009). Shoreline extraction from the integration of lidar point cloud data and aerial orthophotos using mean-shift segmentation. In *Proc. ASPRS Annual Conf*, volume 2, pages 3033–3040.

- Lee, J., Jurkevich, L., Dewaele, P., Wambacq, P., and Oosterlinck, A. (1994). Speckle filtering of synthetic aperture radar images: a review. *Remote sensing reviews*, 8(4):313–340.
- Li, H., Lee, W. S., Wang, K., Ehsani, R., and Yang, C. (2014). “Extended spectral angle mapping (ESAM)” for citrus greening disease detection using airborne hyperspectral imaging. *Precision Agriculture*, 15(2):162–183.
- Lindsey, R. (2019). Climate Change: Global Sea Level. *Climate Watch Magazine*. <https://www.climate.gov/news-features/understanding-climate/climate-change-global-sea-level>, accessed 2020-05-05.
- Liu, H. and Jezek, K. (2004). Automated extraction of coastline from satellite imagery by integrating canny edge detection and locally adaptive thresholding methods. *International journal of remote sensing*, 25(5):937–958.
- Liu, Y., Wang, X., Ling, F., Xu, S., and Wang, C. (2017). Analysis of coastline extraction from Landsat-8 OLI imagery. *Water*, 9(11):816.
- Loncan, L., De Almeida, L. B., Bioucas-Dias, J. M., Briottet, X., Chanussot, J., Dobigeon, N., Fabre, S., Liao, W., Licciardi, G. A., Simoes, M., et al. (2015). Hyperspectral pansharpening: a review. *IEEE Geoscience and remote sensing magazine*, 3(3):27–46.
- Lopes, A., Nezry, E., Touzi, R., and Laur, H. (1993). Structure detection and statistical adaptive speckle filtering in SAR images. *International Journal of Remote Sensing*, 14(9):1735–1758.
- Lu, D., Mausel, P., Brondizio, E., and Moran, E. (2004). Change detection techniques. *International journal of remote sensing*, 25(12):2365–2401.
- Lubczonek, J. (2017). Application of Sentinel-1 imageries for shoreline extraction. In *2017 18th International Radar Symposium (IRS)*, pages 1–9. IEEE.
- Ma, H. and Zhang, L. (2019). Ocean SAR Image Segmentation and Edge Gradient Feature Extraction. *Journal of Coastal Research*, 94(SI):141–144.

- 
- MacDougall, J. (2017). How to create a normally distributed set of random numbers in excel. <https://www.howtoexcel.org/statistics/normal-distribution/>, accessed 2020-10-09.
- Maglione, P., Parente, C., and Vallario, A. (2014). Coastline extraction using high resolution WorldView-2 satellite imagery. *European Journal of Remote Sensing*, 47(1):685–699.
- Maglione, P., Parente, C., and Vallario, A. (2015). High resolution satellite images to reconstruct recent evolution of domitian coastline. *American Journal of Applied Sciences*, 12(7):506.
- Mahyoub, S., Fadil, A., Mansour, E., Rhinane, H., and Al-Nahmia, F. (2019). Fusing of optical and synthetic aperture radar (SAR) remote sensing data: a systematic literature review (SLR). *International Archives of the Photogrammetry, Remote Sensing and Spatial Information Sciences*, 42(4/W12).
- Manno, G., Ciraiolo, G., and Liguori, V. (2012). *Localizzazione della linea di riva, in spiagge sabbiose stabili, considerando le fluttuazioni da onde e maree*. PhD thesis, Palermo University, Department of Civil, Environmental and Aerospace Engineering (DICA). <https://core.ac.uk/download/pdf/53283091.pdf>, accessed 2020-04-07.
- Marghany, M., Sabu, Z., and Hashim, M. (2010). Mapping coastal geomorphology changes using synthetic aperture radar data. *International Journal of Physical Sciences*, 5(12):1890–1896.
- Márquez-Martínez, J., Mittermayer, J., and Rodríguez-Cassolà, M. (2004). Radiometric resolution optimization for future sar systems. In *IGARSS 2004. 2004 IEEE International Geoscience and Remote Sensing Symposium*, volume 3, pages 1738–1741. IEEE.
- Martelli, C., Bitelli, G., Vittuari, L., and Mognol, A. (2008/2009). Estrazione di features con tecniche di classificazione pixel e object-oriented.
- Martimort, P., Arino, O., Berger, M., Biasutti, R., Carnicero, B., Del Bello, U., Fernandez, V., Gascon, F., Greco, B., Silvestrin, P., et al. (2007). Sentinel-2 optical high resolution mission for GMES operational services.

- In *2007 IEEE International Geoscience and Remote Sensing Symposium*, pages 2677–2680. IEEE.
- Martin, J., Eugenio, F., Marcello, J., and Medina, A. (2016). Automatic sun glint removal of multispectral high-resolution WorldView-2 imagery for retrieving coastal shallow water parameters. *Remote Sensing*, 8(1):37.
- Masi, G., Cozzolino, D., Verdoliva, L., and Scarpa, G. (2016). Pansharpening by convolutional neural networks. *Remote Sensing*, 8(7):594.
- Masoud, K. M., Persello, C., and Tolpekin, V. A. (2020). Delineation of Agricultural Field Boundaries from Sentinel-2 Images Using a Novel Super-Resolution Contour Detector Based on Fully Convolutional Networks. *Remote sensing*, 12(1):59.
- Mastriani, M. and Giraldez, A. E. (2016). Enhanced directional smoothing algorithm for edge-preserving smoothing of synthetic-aperture radar images. *arXiv preprint arXiv:1608.01993*.
- McFeeters, S. K. (1996). The use of the Normalized Difference Water Index (NDWI) in the delineation of open water features. *International journal of remote sensing*, 17(7):1425–1432.
- Meng, X., Shen, H., Li, H., Zhang, L., and Fu, R. (2019). Review of the pansharpening methods for remote sensing images based on the idea of meta-analysis: practical discussion and challenges. *Information Fusion*, 46:102–113.
- Mentaschi, L., Vousdoukas, M. I., Pekel, J.-F., Voukouvalas, E., and Feyen, L. (2018). Global long-term observations of coastal erosion and accretion. *Scientific reports*, 8(1):1–11.
- Miles, K. E., Willis, I. C., Benedek, C. L., Williamson, A. G., and Tedesco, M. (2017). Toward monitoring surface and subsurface lakes on the Greenland ice sheet using Sentinel-1 SAR and Landsat-8 OLI imagery. *Frontiers in Earth Science*, 5:58.
- Mills, J., Buckley, S., Mitchell, H., Clarke, P., and Edwards, S. (2005). A geomatics data integration technique for coastal change monitoring.

---

*Earth Surface Processes and Landforms: the Journal of the British Geomorphological Research Group*, 30(6):651–664.

Minghelli, A., Spagnoli, J., Lei, M., Chami, M., and Charmasson, S. (2020). Shoreline Extraction from WorldView2 Satellite Data in the Presence of Foam Pixels Using Multispectral Classification Method. *Remote Sensing*, 12(16):2664.

Mishra, R. K. (2019). Image Processing for Computer Vision(Part 1). <https://medium.com/@rohitm487/image-processing-for-computer-vision-part-1-38d296becd29>, accessed 2020-05-19.

Misra, A. and Balaji, R. (2015). A study on the shoreline changes and land-use/land-cover along the South Gujarat coastline. *Procedia Engineering*, 116(1):381–389.

Montalti, R., Solari, L., Bianchini, S., Del Soldato, M., Raspini, F., and Casagli, N. (2019). A Sentinel-1-based clustering analysis for geo-hazards mitigation at regional scale: a case study in Central Italy. *Geomatics, Natural Hazards and Risk*, 10(1):2257–2275.

Moore, L. J. (2000). Shoreline mapping techniques. *Journal of coastal research*, pages 111–124.

Moreira, A. (2013). Synthetic Aperture Radar (SAR): Principles and Applications. page 62. <https://earth.esa.int/documents/10174/642943/6-LTC2013-SAR-Moreira.pdf>, accessed 2020-05-06.

Moreira, A., Prats-Iraola, P., Younis, M., Krieger, G., Hajnsek, I., and Papathanassiou, K. P. (2013). A tutorial on synthetic aperture radar. *IEEE Geoscience and Remote Sensing Magazine*, 1(1):6–43. <http://ieeexplore.ieee.org/document/6504845/>, accessed 2020-03-20.

Morton, R. A., Leach, M. P., Paine, J. G., and Cardoza, M. A. (1993). Monitoring beach changes using GPS surveying techniques. *Journal of Coastal Research*, pages 702–720.

Morton, R. A. and Speed, F. M. (1998). Evaluation of shorelines and legal boundaries controlled by water levels on sandy beaches. *Journal of Coastal Research*, pages 1373–1384.

- Mouginot, J., Rignot, E., Scheuchl, B., and Millan, R. (2017). Comprehensive annual ice sheet velocity mapping using Landsat-8, Sentinel-1, and RADARSAT-2 data. *Remote Sensing*, 9(4):364.
- Mutanga, O., Adam, E., and Cho, M. A. (2012). High density biomass estimation for wetland vegetation using WorldView-2 imagery and random forest regression algorithm. *International Journal of Applied Earth Observation and Geoinformation*, 18:399–406.
- Nagler, T., Rott, H., Hetzenecker, M., Wuite, J., and Potin, P. (2015). The Sentinel-1 mission: New opportunities for ice sheet observations. *Remote Sensing*, 7(7):9371–9389.
- NASA (2020). What is Remote Sensing? <https://earthdata.nasa.gov/learn/remote-sensing>. accessed 2020-03-12.
- Natural Resources Canada (2008). Geometric Distortion in Imagery. <https://www.nrcan.gc.ca/maps-tools-publications/satellite-imagery-air-photos/remote-sensing-tutorials/satellites-sensors/geometric-distortion-imagery/9401> accessed 2020-05-20.
- Neumann, B., Vafeidis, A. T., Zimmermann, J., and Nicholls, R. J. (2015). Future coastal population growth and exposure to sea-level rise and coastal flooding—a global assessment. *PloS one*, 10(3):e0118571.
- Nezhad, M. M., Groppi, D., Marzialetti, P., Piras, G., and Laneve, G. (2018). Mapping Sea Water Surface in Persian Gulf, Oil Spill Detection Using Sentinel-1 Images. In *Proc. 4th World Congr. New Technol. ICEPR*, volume 179, pages 1–8.
- Novellino, A., Cigna, F., Sowter, A., Ramondini, M., and Calcaterra, D. (2017). Exploitation of the Intermittent SBAS (ISBAS) algorithm with COSMO-SkyMed data for landslide inventory mapping in north-western Sicily, Italy. *Geomorphology*, 280:153–166.
- Nunziata, F., Buono, A., and Migliaccio, M. (2018). COSMO–SkyMed Synthetic Aperture Radar data to observe the Deepwater Horizon oil spill. *Sustainability*, 10(10):3599.

- 
- Olaode, A., Naghdy, G., and Todd, C. (2014). Unsupervised classification of images: a review. *International Journal of Image Processing*, 8(5):325–342.
- Orynbaikyzy, A., Gessner, U., Mack, B., and Conrad, C. (2020). Crop Type Classification Using Fusion of Sentinel-1 and Sentinel-2 Data: Assessing the Impact of Feature Selection, Optical Data Availability, and Parcel Sizes on the Accuracies. *Remote Sensing*, 12(17):2779.
- OSSIM (2014). Orthorectification. <https://trac.osgeo.org/ossim/wiki/orthorectification>, accessed 2020-05-27.
- Ouma, Y. O. and Tateishi, R. (2006). A water index for rapid mapping of shoreline changes of five East African Rift Valley lakes: an empirical analysis using Landsat TM and ETM+ data. *International Journal of Remote Sensing*, 27(15):3153–3181.
- Padwick, C., Deskevich, M., Pacifici, F., and Smallwood, S. (2010). Worldview-2 pan-sharpening. In *Proceedings of the ASPRS 2010 Annual Conference, San Diego, CA, USA*, volume 2630, pages 1–14.
- Palazzo, F., Latini, D., Baiocchi, V., Del Frate, F., Giannone, F., Dominici, D., and Remondiere, S. (2012). An application of COSMO-Sky Med to coastal erosion studies. *European Journal of Remote Sensing*, 45(1):361–370.
- Palombo, A., Pascucci, S., Loperte, A., Lettino, A., Castaldi, F., Muolo, M. R., and Santini, F. (2019). Soil Moisture Retrieval by Integrating TASI-600 Airborne Thermal Data, WorldView 2 Satellite Data and Field Measurements: Petacciato Case Study. *Sensors*, 19(7):1515.
- Papakonstantinou, A., Topouzelis, K., and Pavlogeorgatos, G. (2016). Coastline zones identification and 3D coastal mapping using UAV spatial data. *ISPRS International Journal of Geo-Information*, 5(6):75.
- Paravolidakis, V., Moirogiorgou, K., Ragia, L., Zervakis, M., and Synolakis, C. (2016). Coastline extraction from aerial images based on edge detection. *ISPRS Annals of the Photogrammetry, Remote Sensing and Spatial Information Sciences*, 3:153.

- Paravolidakis, V., Ragia, L., Moirogiorgou, K., and Zervakis, M. E. (2018). Automatic coastline extraction using edge detection and optimization procedures. *Geosciences*, 8(11):407.
- Pardo-Pascual, J. E., Almonacid-Caballer, J., Ruiz, L. A., and Palomar-Vázquez, J. (2012). Automatic extraction of shorelines from Landsat TM and ETM+ multi-temporal images with subpixel precision. *Remote Sensing of Environment*, 123:1–11.
- Pardo-Pascual, J. E., Sánchez-García, E., Almonacid-Caballer, J., Palomar-Vázquez, J. M., Priego De Los Santos, E., Fernández-Sarría, A., and Balaguer-Beser, Á. (2018). Assessing the accuracy of automatically extracted shorelines on microtidal beaches from Landsat 7, Landsat 8 and Sentinel-2 imagery. *Remote Sensing*, 10(2):326.
- Park, B., Windham, W., Lawrence, K., and Smith, D. (2007). Contaminant classification of poultry hyperspectral imagery using a spectral angle mapper algorithm. *Biosystems Engineering*, 96(3):323–333.
- Park, J., Korosov, A., Babiker, M., Sandven, S., and Won, J. (2017). Efficient thermal noise removal for Sentinel-1 TOPSAR cross-polarization channel. *IEEE Transactions on Geoscience and Remote Sensing*, 56(3):1555–1565.
- Parris, A., Bromirski, P., Burkett, V., Cayan, D., Culver, M., Hall, J., Horton, R., Knuuti, K., JO, R. M., Sallenger, A., et al. (2016). Global sea level rise scenarios for the us national climate assessment; 2012.
- PCI Geomatics (2020). Explaining ground control points. [https://www.pcigeomatics.com/geomatica-help/COMMON/concepts/GCP\\_explainGCPs.html#:~:text=A%20ground%20control%20point%20\(GCP,have%20a%20known%20ground%20coordinate.&text=A%20GCP%20determines%20the%20relationship,z%20coordinates%20on%20the%20ground.,](https://www.pcigeomatics.com/geomatica-help/COMMON/concepts/GCP_explainGCPs.html#:~:text=A%20ground%20control%20point%20(GCP,have%20a%20known%20ground%20coordinate.&text=A%20GCP%20determines%20the%20relationship,z%20coordinates%20on%20the%20ground.,) accessed 2020-10-15.
- PCI Geomatics (n.d.). Understanding orthorectification. <https://www.pcigeomatics.com/>, accessed 2018-12-05.

- 
- Pelich, R., Chini, M., Hostache, R., Matgen, P., and López-Martínez, C. (2020). Coastline Detection Based on Sentinel-1 Time Series for Ship-and Flood-Monitoring Applications. *IEEE Geoscience and Remote Sensing Letters*.
- Pohl, C. and Van Genderen, J. (1998). Review article multisensor image fusion in remote sensing: concepts, methods and applications. *International journal of remote sensing*, 19(5):823–854.
- Pour, A. B. and Hashim, M. (2014). Structural geology mapping using PALSAR data in the Bau gold mining district, Sarawak, Malaysia. *Advances in Space Research*, 54(4):644–654.
- Pradhan, B., Rizeei, H. M., and Abdulle, A. (2018). Quantitative assessment for detection and monitoring of coastline dynamics with temporal RADARSAT images. *Remote Sensing*, 10(11):1705.
- Pranzini, E., Wetzel, L., and Williams, A. T. (2015). Aspects of coastal erosion and protection in Europe. *Journal of coastal conservation*, 19(4):445–459.
- Pulvirenti, L., Chini, M., Pierdicca, N., Guerriero, L., and Ferrazzoli, P. (2011). Flood monitoring using multi-temporal COSMO-SkyMed data: Image segmentation and signature interpretation. *Remote Sensing of Environment*, 115(4):990–1002.
- Quegan, S., Le Toan, T., Yu, J., Ribbes, F., and Floury, N. (2000). Multi-temporal ERS SAR analysis applied to forest mapping. *IEEE Transactions on Geoscience and Remote Sensing*, 38(2):741–753.
- Rajib, S. (2019). Chapter 1 - Global Coasts in the Face of Disasters. In *Coastal Management*, pages 1–4. R.R. Krishnamurthy, M.P. Jonathan, Seshachalam Srinivasalu, Bernhard Glaeser, academic press edition. (<http://www.sciencedirect.com/science/article/pii/B9780128104736000017>), accessed 2020-04-24.
- Refice, A., Capolongo, D., Pasquariello, G., D’Addabbo, A., Bovenga, F., Nutricato, R., Lovergine, F., and Pietranera, L. (2014). SAR and InSAR for flood monitoring: Examples with COSMO-SkyMed data. *IEEE*

- Journal of Selected Topics in Applied Earth Observations and Remote Sensing*, 7(7):2711–2722.
- Ribas, F., Simarro, G., Arriaga, J., and Luque, P. (2020). Automatic shoreline detection from video images by combining information from different methods. *Remote Sensing*, 12(22):3717.
- Rishikeshan, C. and Ramesh, H. (2017). A novel mathematical morphology based algorithm for shoreline extraction from satellite images. *Geo-spatial information science*, 20(4):345–352.
- Roskopf, C. M., Di Paola, G., Atkinson, D. E., Rodríguez, G., and Walker, I. J. (2018). Recent shoreline evolution and beach erosion along the central Adriatic coast of Italy: the case of Molise region. *Journal of Coastal Conservation*, 22(5):879–895.
- Sahir, S. (2019 (accessed November 10, 2020)). Canny edge detection step by step in python - computer vision. <https://towardsdatascience.com/canny-edge-detection-step-by-step-in-python-computer-vision-b49c3a2d8123>, accessed 2020-10-10.
- Saleem, A. and Awange, J. (2019). Coastline shift analysis in data deficient regions: exploiting the high spatio-temporal resolution Sentinel-2 products. *Catena*, 179:6–19.
- Salman, A., Lombardo, S., and Doody, P. (2004). Living with coastal erosion in Europe: sediment and space for sustainability. *Eurosion project reports*.
- Santurri, L., Aiazzi, B., Baronti, S., and Carlà, R. (2012). Influence of spatial resolution on pan-sharpening results. In *2012 IEEE International Geoscience and Remote Sensing Symposium*, pages 5446–5449. IEEE.
- Satellite Image Corporation (2001-2017). Orthorectification. <https://www.satimagingcorp.com/services/orthorectification/>, accessed 2020-10-06.
- Satellite Imaging Corporation (n.d.a). Sentinel-2A SatelliteSensor - Satellite Imaging Corp. <https://www.satimagingcorp.com/satellite->

- 
- sensors/other-satellite-sensors/sentinel-2a/, accessed 2020-05-21.
- Satellite Imaging Corporation (n.d.b). WorldView-2 Satellite Sensor | Satellite Imaging Corp. <https://www.satimagingcorp.com/satellite-sensors/worldview-2/>, accessed 2020-05-26.
- Scientific American (2008). What causes beach erosion? <https://www.scientificamerican.com/article/what-causes-beach-erosion/>, accessed 2020-04-21.
- Sekovski, I., Stecchi, F., Mancini, F., and Del Rio, L. (2014). Image classification methods applied to shoreline extraction on very high-resolution multispectral imagery. *International Journal of Remote Sensing*, 35(10):3556–3578.
- SensorsONE (2020). Radar Distance Sensing. <https://www.sensorsone.com/radar-distance-sensing/>, accessed 2020-05-12.
- Sheng, G., Yang, W., Deng, X., He, C. and Cao, Y., and Sun, H. (2012). Coastline detection in synthetic aperture radar (SAR) images by integrating watershed transformation and controllable gradient vector flow (GVF) snake model. *IEEE Journal of Oceanic Engineering*, 37(3):375–383.
- Sherifview (2010). Radar Technology and Products: SLAR Side Looking Radar. <http://radar-air-land-sea.blogspot.com/2010/07/slarside-looking-radar.html>, accessed 2020-03-23.
- Shoshany, M. and Degani, A. (1992). Shoreline detection by digital image processing of aerial photography. *Journal of Coastal Research*, pages 29–34.
- Siddiqui, M. D. and Zaidi, A. Z. (2016). Worldview-2 and Landsat 8 Satellite Data for Seaweed Mapping along Karachi Coast. *Pakistan Journal of Engineering, Technology & Science*, 5(2).
- Singh, A. (1989). Review article digital change detection techniques using remotely-sensed data. *International journal of remote sensing*, 10(6):989–1003.

- Singh, K. V., Setia, R., Sahoo, S., Prasad, A., and Pateriya, B. (2015). Evaluation of NDWI and MNDWI for assessment of waterlogging by integrating digital elevation model and groundwater level. *Geocarto International*, 30(6):650–661.
- Singh, P. and Shree, R. (2016). Analysis and effects of speckle noise in sar images. In *2016 2nd International Conference on Advances in Computing, Communication, & Automation (ICACCA)(Fall)*, pages 1–5. IEEE.
- Sisodia, P. S., Tiwari, V., and Kumar, A. (2014). A comparative analysis of remote sensing image classification techniques. In *2014 International Conference on Advances in Computing, Communications and Informatics (ICACCI)*, pages 1418–1421. IEEE.
- Sivaranjani, R., Roomi, S., and Senthilarasi, M. (2019). Speckle noise removal in SAR images using Multi-Objective PSO (MOPSO) algorithm. *Applied Soft Computing*, 76:671–681.
- Small, C. and Nicholls, R. J. (2003). A global analysis of human settlement in coastal zones. *Journal of coastal research*, pages 584–599.
- Smith, G. L. and Zarillo, G. A. (1990). Calculating long-term shoreline recession rates using aerial photographic and beach profiling techniques. *Journal of coastal research*, pages 111–120.
- Sohn, Y. and Rebello, N. S. (2002). Supervised and unsupervised spectral angle classifiers. *Photogrammetric engineering and remote sensing*, 68(12):1271–1282.
- Sorensen, R. M. (2005). *Basic coastal engineering*, volume 10. Springer Science & Business Media.
- Spagnoli, J., Minghelli, A., and Charmasson, S. (2018). Shoreline Monitoring Using WorldView-2 Images Along the Coast of Sendai after the Tohoku Tsunami in Presence of Foam. In *2018 OCEANS-MTS/IEEE Kobe Techno-Oceans (OTO)*, pages 1–8. IEEE.
- Spatial analyst (n.d.). Resample. [http://spatial-analyst.net/ILWIS/html/ilwisapp/resample\\_functionality.htm](http://spatial-analyst.net/ILWIS/html/ilwisapp/resample_functionality.htm), accessed 2020-09-15.

- 
- Spatial Solutions (n.d.). Spatial IT Solutions. <https://spatialitsolutions.com/>, accessed 2020-03-17.
- Spinosa, A., Ziemba, A., Saponieri, A., Navarro-Sanchez, V. D., Damiani, L., and El Serafy, G. (2018). Automatic extraction of shoreline from satellite images: a new approach. In *2018 IEEE International Workshop on Metrology for the Sea; Learning to Measure Sea Health Parameters (MetroSea)*, pages 33–38. IEEE.
- Stafford, D. B. and Langfelder, J. (1971). Air photo survey of coastal erosion. *Photogrammetric engineering*, 37(6):565–575.
- Steinhausen, M. J., Wagner, P. D., Narasimhan, B., and Waske, B. (2018). Combining Sentinel-1 and Sentinel-2 data for improved land use and land cover mapping of monsoon regions. *International journal of applied earth observation and geoinformation*, 73:595–604.
- Stockdonf, H. F., Sallenger Jr, A. H., List, J. H., and Holman, R. A. (2002). Estimation of shoreline position and change using airborne topographic lidar data. *Journal of Coastal Research*, pages 502–513.
- Sutherland, J. (2019). EUROSION project - Coastal Wiki. [http://www.coastalwiki.org/wiki/EUROSION\\_project](http://www.coastalwiki.org/wiki/EUROSION_project), accessed 2020-05-05.
- Sweet, W. V., Kopp, R. E., Weaver, C. P., Obeysekera, J., Horton, R. M., Thieler, E. R., and Zervas, C. (2017). Global and regional sea level rise scenarios for the United States.
- Syaifulnizam, A., Norwati, M., Sulaiman, M. N., Husin, Nor Azura, H., and R.A.H., M. (2018). Change analysis on historical shorelines extracted from medium resolution satellite images: a case study on the southern coast of Peninsular Malaysia. In *IOP Conference Series: Earth and Environmental Science*, volume 169, page 012101. IOP Publishing.
- Taha, L. G. E. and Elbeih, S. F. (2010). Investigation of fusion of SAR and Landsat data for shoreline super resolution mapping: the northeastern Mediterranean Sea coast in Egypt. *Applied Geomatics*, 2(4):177–186.
- Tapete, D. and Cigna, F. (2019). COSMO-SkyMed SAR for detection and

- monitoring of archaeological and cultural heritage sites. *Remote Sensing*, 11(11):1326.
- Thakkar, D., Patel, A., and Patel, M. (2016). Geometric distortion and correction methods for finding key points: a survey. *IJSRD - International Journal for Scientific Research & Development*, 4(2):311–314.
- Thanh Noi, P. and Kappas, M. (2018). Comparison of random forest, k-nearest neighbor, and support vector machine classifiers for land cover classification using Sentinel-2 imagery. *Sensors*, 18(1):18.
- TIDES4FISHING (n.d.). TIDES4FISHING. <https://tides4fishing.com/>, accessed 2019-05-29.
- Tom, M., Aguilar, R., Imhof, P., Leinss, S., Baltsavias, E., and Schindler, K. (2020). Lake Ice Detection from Sentinel-1 SAR with Deep Learning. *arXiv preprint arXiv:2002.07040*.
- Topaloğlu, R. H., Sertel, E., and Musaoğlu, N. (2016). Assessment of classification accuracies of Sentinel-2 and Landsat-8 data for Land Cover/Use mapping. *International archives of the photogrammetry, remote sensing & spatial Information Sciences*, 41.
- Torbick, N., Chowdhury, D., Salas, W., and Qi, J. (2017). Monitoring rice agriculture across myanmar using time series Sentinel-1 assisted by Landsat-8 and PALSAR-2. *Remote Sensing*, 9(2):119.
- Toure, S., Diop, O., Kpalma, K., and Maiga, A. S. (2019). Shoreline detection using optical remote sensing: a review. *ISPRS International Journal of Geo-Information*, 8(2):75.
- Turner, D., Lucieer, A., Malenovsky, Z., King, D., and Robinson, S. (2014). Spatial co-registration of ultra-high resolution visible, multispectral and thermal images acquired with a micro-UAV over Antarctic moss beds. *Remote Sensing*, 6(5):4003–4024.
- Turner, I. L., Harley, M. D., and Drummond, C. D. (2016). UAVs for coastal surveying. *Coastal Engineering*, 114:19–24.

- 
- Umut, H., Mamat, S., Ilyas, N., Rukiya, S., and Wang, J. (2017). Inversion model of soil salt content based on WorldView-2 image. *Transactions of the Chinese Society of Agricultural Engineering*, 33(24):200–206.
- UNFCCC, United Nations Climate Change (2020). The Paris Agreement. [https://unfccc.int/process-and-meetings/the-paris-agreement/the-paris-agreement#:~:text=The%20Paris%20Agreement%20is%20a,compared%20to%20pre%2Dindustrial%20levels.](https://unfccc.int/process-and-meetings/the-paris-agreement/the-paris-agreement#:~:text=The%20Paris%20Agreement%20is%20a,compared%20to%20pre%2Dindustrial%20levels.,), accessed 2020-07-03.
- Universitat Autònoma de Barcelona (2002). Coastal erosion indicators study. *EuroSION project*. <https://www.eea.europa.eu/data-and-maps/data/hydrodynamics-and-sea-level-rise/coastal-erosion-indicators-study/coastal-erosion-indicators-study/download>, accessed 2020-05-05.
- University of Hawaii (2016). UHSLC Legacy Data Portal. <http://uhslc.soest.hawaii.edu/data/?fd>, accessed 2020-05-05.
- Van Heesch, D. (2020). Canny edge detection. [https://docs.opencv.org/master/da/d22/tutorial\\_py\\_canny.html](https://docs.opencv.org/master/da/d22/tutorial_py_canny.html), accessed 2020-10-28.
- Van Tricht, K., Gobin, A., Gilliams, S., and Piccard, I. (2018). Synergistic use of radar Sentinel-1 and optical Sentinel-2 imagery for crop mapping: a case study for Belgium. *Remote Sensing*, 10(10):1642.
- Veci, L. (2019). SAR Basics Tutorial. page 19. <http://step.esa.int/docs/tutorials/S1TBX%20SAR%20Basics%20Tutorial.pdf>, accessed 2020-05-26.
- Veloso, A., Mermoz, S., Bouvet, A., Le Toan, T., Planells, M., Dejoux, J.-F., and Ceschia, E. (2017). Understanding the temporal behavior of crops using Sentinel-1 and Sentinel-2-like data for agricultural applications. *Remote sensing of environment*, 199:415–426.
- Vivone, G., Alparone, L., Chanussot, J., Dalla Mura, M., Garzelli, A., Licciardi, G. A., Restaino, R., and Wald, L. (2014). A critical comparison among pansharpening algorithms. *IEEE Transactions on Geoscience and Remote Sensing*, 53(5):2565–2586.

- Vos, K., Harley, M., Splinter, K., Turner, I., et al. (2019). Satellite-derived shorelines along the east coast of Australia between 1987 and 2019. In *Australasian Coasts and Ports 2019 Conference: Future directions from 40 [degrees] S and beyond, Hobart, 10-13 September 2019*, page 1198. Engineers Australia.
- Wang, P., Zhang, H., and Patel, V. M. (2017). SAR image despeckling using a convolutional neural network. *IEEE Signal Processing Letters*, 24(12):1763–1767.
- Wang, Y., Wang, C., and Zhang, H. (2018). Combining a single shot multibox detector with transfer learning for ship detection using Sentinel-1 SAR images. *Remote sensing letters*, 9(8):780–788.
- Whitfield, A. and Elliott, M. (2011). Ecosystem and biotic classifications of estuaries and coasts. *Treatise on Estuarine and Coastal Science; Elsevier: Amsterdam, The Netherlands*, pages 99–124.
- Wolf, A. F. (2012). Using WorldView-2 Vis-NIR multispectral imagery to support land mapping and feature extraction using normalized difference index ratios. In *Algorithms and Technologies for Multispectral, Hyperspectral, and Ultraspectral Imagery XVIII*, volume 8390, page 83900N. International Society for Optics and Photonics.
- Wolf, P., Dewitt, B., and Wilkinson, B. (2014). Development of Collinearity Condition Equations. McGraw-Hill Education, New York. <https://www.accessengineeringlibrary.com/content/book/9780071761123/back-matter/appendix4>, accessed 2020-04-21.
- Wolff, C. (2008). Synthetic Aperture Radar - Radartutorial. <https://www.radartutorial.eu/20.airborne/ab07.en.html>, accessed 2020-05-11.
- Wolff, C. (n.d.a). Radar Basics - Radar Principle. <https://www.radartutorial.eu/01.basics/Radar%20Principle.en.html>, accessed 2020-03-24.
- Wolff, C. (n.d.b). Radar Basics - Synthetic Aperture Radar. <https://www.radartutorial.eu/01.basics/SAR.en.html>, accessed 2020-03-24.

---

//www.radartutorial.eu/20.airborne/ab07.en.html, accessed 2020-03-20.

- Woo, H. and Yun, S. (2011). Alternating minimization algorithm for speckle reduction with a shifting technique. *IEEE Transactions on Image Processing*, 21(4):1701–1714.
- Xie, C., Huang, X., Zeng, W., and Fang, X. (2016). A novel water index for urban high-resolution eight-band WorldView-2 imagery. *International journal of digital earth*, 9(10):925–941.
- Xu, H. (2006). Modification of normalised difference water index (NDWI) to enhance open water features in remotely sensed imagery. *International journal of remote sensing*, 27(14):3025–3033.
- Xu, X., Sandwell, D. T., and Smith-Konter, B. (2020). Coseismic displacements and surface fractures from Sentinel-1 InSAR: 2019 Ridgecrest earthquakes. *Seismological Research Letters*.
- Yan, J., Zhou, W., Han, L., and Qian, Y. (2018). Mapping vegetation functional types in urban areas with WorldView-2 imagery: Integrating object-based classification with phenology. *Urban Forestry & Urban Greening*, 31:230–240.
- Yen, N. and Kim, T. (2020). Coastline changes detection from Sentinel-1 satellite imagery using spatial fuzzy clustering and interactive thresholding method in Phan Thiet, Binh Thuan. *Vietnam journal of Hydrometeorol*, 6:1–10.
- You, Y.-L. and Kaveh, M. (2000). Fourth-order partial differential equations for noise removal. *IEEE Transactions on Image Processing*, 9(10):1723–1730.
- Young, G. (2020). Why in computer science do the screen coordinates have the opposite y? - Quora. <https://www.quora.com/Why-in-computer-science-do-the-screen-coordinates-have-the-opposite-y>, accessed 2020-05-19.
- Yun, S., Hudnut, K., Owen, S., Webb, F., Simons, M., Sacco, P., Gurrola, E., Manipon, G., Liang, C., Fielding, E., et al. (2015). Rapid Damage

- Mapping for the 2015 M w 7.8 Gorkha Earthquake Using Synthetic Aperture Radar Data from COSMO–SkyMed and ALOS-2 Satellites. *Seismological Research Letters*, 86(6):1549–1556.
- Zhang, H. and Xu, R. (2018). Exploring the optimal integration levels between SAR and optical data for better urban land cover mapping in the Pearl River Delta. *International journal of applied earth observation and geoinformation*, 64:87–95.
- Zhang, J., Yang, J., Zhao, Z., Li, H., and Zhang, Y. (2010). Block-regression based fusion of optical and SAR imagery for feature enhancement. *International Journal of Remote Sensing*, 31(9):2325–2345.
- Zhang, K., Huang, W., Douglas, B. C., and Leatherman, S. (2002). Shoreline position variability and long-term trend analysis. *Shore and Beach*, 70(2):31–35.
- Zhang, T., Yang, X., Hu, S., and Su, F. (2013). Extraction of coastline in aquaculture coast from multispectral remote sensing images: object-based region growing integrating edge detection. *Remote sensing*, 5(9):4470–4487.
- Zhu, L., Suomalainen, J., Liu, J., Hyypä, J., Kaartinen, H., and Haggren, H. (2017). A Review: Remote Sensing Sensors. *Multi-purposeful Application of Geospatial Data*. <https://www.intechopen.com/books/multi-purposeful-application-of-geospatial-data/a-review-remote-sensing-sensors>, accessed 2020-05-11.

[Blank page]



# LIST OF TERMS

**ACM** Active Connection Matrix. 49, 66–69, 73, 75, 82, 91, 92, 101, 109, 114–117, 163–165, 168, 171–175

**ANN** Artificial Neural Network. 13

**AR** Automata Rule. 68, 163, 165, 166, 171

**ASI** Italian Space Agency. 46

**CBD** Colour Band Divergence. 13, 15

**CH** Chieti. 73, 74, 77

**CM** Contractive Map. 68, 70, 83, 85, 116, 166, 171

**COSMO-SkyMed** COnstellation of small Satellites for Mediterranean basin Observation. 19, 24, 46, 47, 119

**CP** Check Point. 78

**CSG** COSMO Second Generation. 46

**CSK** COSMO-SkyMed. 46

**DEM** Digital Elevation Model. 52, 53, 78, 106

**DGPS** Differential Global Positioning System. 18

**DN** Digital Number. 26, 60, 79

**EC** European Commission. 39, 43

**EO** Earth Observation. 18, 39, 103

**ESA** European Space Agency. 39, 43

- ETM+** Enhanced Thematic Mapper Plus. 18–20
- EW** Extra Wide swath. 40, 42
- FR** Full Resolution. 42
- GCP** Ground Control Point. 53–56, 78
- GHG** GreenHouse Gases. 5, 6
- GIS** Geographic Information System. 19, 55
- GNSS** Global Navigation Satellite System. 15, 78
- GPS** Global Positioning System. 19, 55, 56, 101, 104, 110–116
- GRD** Ground Range Detected. 42, 85, 86
- HCS** Hyperspherical Color Space. 58, 78
- HR** High Resolution. 42, 43, 73–75, 91, 95–97, 115, 116
- HWL** High Water Line. 13
- IR** InfraRed. 19
- ISODATA** Iterative Self-Organizing Data Analysis Technique. 20, 64, 81
- ISPRA** Istituto Superiore per la Protezione e la Ricerca Ambientale. 9
- IW** Interferometric Wide swath. 40–42, 85, 86
- LIDAR** Light Detection And Ranging. 15, 102
- LOS** Line Of Sight. 37
- MHW** Mean High Water. 13
- MIUR** Ministry of Education, Universities and Research. 46
- MLLW** Mean Lower Low Water. 86
- MoD** Ministry of Defence. 46
- MR** Medium Resolution. 42

---

**NDVI** Normalised Difference Vegetation Index. 59, 60, 73, 75, 79, 80, 83, 84, 97, 107, 108, 116

**NDWI** Normalised Difference Water Index. 18, 19, 59, 97, 107, 108

**New CS** New Constraint Satisfaction Networks. 68, 70, 165, 171

**New IAC** New Interactive Activation and Competition. 68, 69, 164, 165, 171

**NIR** Near InfraRed. 23, 29, 45, 59, 60, 74, 80, 82, 83, 90, 92, 106–108, 116

**NOAA** National Oceanic and Atmospheric Administration. 4

**OBIA** Object-Based Image Analysis. 102

**OCN** OCeaN. 42, 43

**PCA** Principal Component Analysis. 58, 78

**PDF** Probability Distribution Function. 62

**PIC** Pixel Intensity Clustering. 13

**QGIS** Quantum Geographic Information System. 19, 109

**RADAR** RADio Detection And Ranging. 24, 32, 34, 35

**RFC** Rational Function Coefficient. 54

**RFM** Rational Function Model. 54

**RGB** Red Green Blue. 29

**RMSD** Root Mean Square Difference. 98, 99

**RPC** Rational Polynomial Coefficient. 54, 55

**RPF** Rational Polynomial Function. 54, 55

**SAR** Synthetic Aperture Radar. 16, 19, 24, 32–39, 41–43, 46, 50, 73–75, 85–88, 90, 92, 94, 95, 97–99, 101, 102, 104–106, 110, 111, 114–116, 118, 119

**SAVI** Soil Adjusted Vegetation Index. 107, 108

- SDS** Satellite Derived Shoreline. 98
- SLC** Single Look Complex. 42
- SM** Strip Map. 40, 42
- SNAP** Sentinel Application Platform. 87, 88, 90, 106
- SWIR** Short Wave InfraRed. 106–108
- TCW** Tasseled Cap Wetness. 18
- TM** Thematic Mapper. 18, 19
- TOPSAR** Terrain Observation with Progressive Scans SAR. 41, 86, 87
- UAV** Unmanned Aerial Vehicle. 16
- UK** United Kingdom. 6
- USA** United States of America. 22, 66
- USGS** United States Geological Survey. 18
- UTM** Universal Transverse Mercator. 44, 77, 106
- VDS** Video-Derived Shoreline. 98
- VHR** Very High Resolution. 45, 46, 57, 73, 74, 91, 95–97, 115, 116
- VI** Vegetation Index. 59
- WGS84** World Geodetic System 84. 44, 77, 86, 106
- WI** Water Index. 59
- WV** WaVe mode. 40, 42, 43
- WWVI** WorldView Water Index. 59, 73, 75, 80, 83, 84, 93, 95, 96, 107, 116

# LIST OF PUBLICATIONS

The following papers are indexed on ISI/Scopus and/or of A level in ANVUR ranking.

- Dominici, D., **Zollini, S.**, Alicandro, M., Della Torre, F., Buscema, P. M., & Baiocchi, V. (2019). High Resolution Satellite Images for Instantaneous Shoreline Extraction Using New Enhancement Algorithms. *Geosciences*, 9(3), 123.
- Alicandro, M., Candigliota, E., Dominici, D., Immordino, F., Quaresima, R., & **Zollini, S.**(2019). Alba Fucens Archaeological Site: Multiscale and Multidisciplinary Approach for Risk Assessment and Conservation. *ISPRS-International Archives of the Photogrammetry, Remote Sensing and Spatial Information Sciences*, 4211, 47-53.
- **Zollini, S.**, Alicandro, M., Cuevas-González, M., Baiocchi, V., Dominici, D., & Buscema, P. M. (2020). Shoreline Extraction Based on an Active Connection Matrix (ACM) Image Enhancement Strategy. *Journal of Marine Science and Engineering*, 8(1), 9.
- Dominici, D.; **Zollini, S.**(2020). Remote Sensing in Coastline Detection. *Journal of Marine Science and Engineering*, 8, 498.
- **Zollini, S.**; Alicandro, M.; Dominici, D.; Quaresima, R.; Giallonardo, M. (2020). UAV Photogrammetry for Concrete Bridge Inspection Using Object-Based Image Analysis (OBIA). *Remote Sensing*, 12, 3180.
- Alicandro, M., Dominici, D., Quaresima, R., **Zollini, S.**, De Luca, D., & Pietrangeli, S. (2020, November). Geomatic multiscale approach

for the conservation of archeological sites: the case of Alba Fucens (LAquila-Italy). In IOP Conference Series: Materials Science and Engineering, 949(1), 012032). IOP Publishing.

---

## International and national conference papers

- Dominici D., Alicandro M., **Zollini, S.**(19-20 October 2017). Cultural Heritages monitoring with geomatic techniques. In: Carlo Baggio, Giorgio Monti, Camillo Nuti, Silvia Santini, Gianfranco Valente, Davide Lavorato. Dynamic interaction of soil and structure (DISS\_17). p. 135-152, Rome, Proceedings.
- Dominici D., Alicandro M., **Zollini, S.**(8-13 April 2018). The smart management of “construction site” in a post-seismic scenario using UAV photogrammetry. Geophysical Research Abstracts, Vol. 20, EGU2018-15620, 2018, EGU General Assembly 2018, Vienna, Austria.
- **Zollini, S.**, Cuevas-González, M., Dominici, D., Monserrat, O., Alicandro, M. (25-26 June 2019). Sentinel 1 and Sentinel 2 applications in coastal areas. 12<sup>th</sup> Themed Remote Sensing Workshop, Extended abstract. ISBN 978-88-8286-377-7.

[Blank page]

# APPENDIX A: ACM SYSTEMS

In the following, the most useful algorithms used in this thesis will be illustrated.

## A.1 Automata Rule

The Automata Rule (AR) (Buscema, 2006) serves to initialize the values of the connections in the ACM with fixed connections (first order of complexity). This algorithm defines the connections between each pixel-unit as a non-linear transformation of their different brightnesses:

$$w_{(ij),(xy)}^{[0]} = \tanh(R'_{(ij),(xy)}) \quad (\text{A.1})$$

where:

$$R'_{(ij),(xy)} = \frac{c}{1-\varepsilon} (2 \cdot R_{(ij),(xy)} - \varepsilon - 1) \quad (\text{A.2})$$

$$R_{(ij),(xy)} = e^{-(\sigma \cdot u_{ij} - \sigma \cdot u_{xy})^2}, \quad 0 \leq \sigma \leq 2^N \quad (\text{A.3})$$

$$\varepsilon = e^{\sigma^2} \quad (\text{A.4})$$

The parameter  $\sigma$  serves to modulate the connection strength. The values obtained with Equation A.1 are close to one the more the brightness values are similar to each other. In this case,  $R_{(ij),(xy)} \approx 1$ , so that  $R'_{(ij),(xy)} \approx c$ . The  $c$  value is a scale factor useful to make the calculations easier since it moves the  $R_{(ij),(xy)}$  value into the  $[-c, c]$  interval (e.g.,  $c = 5$ ). As for the weights' initialization, the automata rule can also be used as a filter on the initial image. A new image will be created where each pixel

value  $u_{ij}^{AR}$  is the average of all the weights connecting  $u_{ij}$  with each pixel of its neighborhood (see Equation A.5):

$$u_{ij}^{AR} = \frac{1}{|I_{u_{ij}}|} \cdot \sum_{u_{x,y} \in u_{ij}} w_{(i,j),(xy)} \quad (\text{A.5})$$

The resulting image will highlight the edges of the pictures in the image. In fact, the more pixels are similar, the more the connection values will look like one (white), so the mean rate will be high. If the pixels have different values, the weights will be closer to  $-1$  (black), as will the average.

## A.2 New IAC

As with all the ACM algorithms, New Interactive Activation and Competition (Buscema, 2006) (New IAC) considers each pixel as an agent connected to the others in its neighborhood. The connections linking  $u_{ij}$  to all the  $u_{xy} \in I_{u_{ij}}$  are initialized by means of the automata rule, then they remain fixed until the end of the process; therefore, New IAC belongs to the first order family. Each  $u_{ij}$  receives excitations and inhibitions from the surroundings and changes its state accordingly at each iteration. Equations A.6 and A.7 allow the computation of the excitation and inhibition values released by the neighborhood of the pixel  $u_{ij}$  at the iteration  $n$ . Equation A.8 determines the input arriving at it as a weighed sum of those quantities. The final value of the activation of the pixel  $u_{ij}$  is then computed by means of Equation A.9:

$$E_{ij}^n = \sum_{u_{xy} \in I_{u_{ij}}} u_{xy}^{[n]} \cdot w_{(ij),(xy)} \cdot \chi_{\{w_{(ij),(xy)} > 0\}}(w_{(ij),(xy)}) \quad (\text{A.6})$$

$$In_{ij}^{[n]} = \sum_{u_{xy} \in I_{u_{ij}}} u_{xy}^{[n]} \cdot w_{(ij),(xy)} \cdot \chi_{\{w_{(ij),(xy)} < 0\}}(w_{(ij),(xy)}) \quad (\text{A.7})$$

where  $\chi_A$  is the indicator function, i.e.,  $\chi_A(x) = 1$  if  $x \in A$ , otherwise  $\chi_A(x) = 0$ ;

$$Net_{ij}^{[n]} = \alpha \cdot E_{ij}^{[n]} + \beta \cdot In_{ij}^{[n]} \quad (\text{A.8})$$

---


$$Act_{ij}^{[n]} = \tanh(Net_{ij}^{[n]}) \quad (\text{A.9})$$

The  $\alpha$  and  $\beta$  parameters modulate the influence of inhibitory and excitatory stimuli coming from the neighborhood. A frequent choice is to place  $\alpha = \beta = \frac{\sigma}{2M}$ . The value of each pixel changes over time, and step by step, new values are computed based on the value that it had in the previous iteration and a quantity, named  $\Delta_{ij}^{[n]}$ , which takes into account the  $Act_{ij}^{[n]}$  value, i.e.,  $u_{ij}^{[n+1]} = f(u_{ij}^{[n]}, \Delta_{ij}^{[n]})$ . Equation A.10 shows how this function works:

$$u_{ij}^{[n+1]} = u_{ij}^{[n]} + \tanh(\Delta_{ij}^{[n]}) \quad (\text{A.10})$$

$$\begin{aligned} \Delta_{ij}^{[n]} = & [(M - u_{ij}^{[n]}) \cdot Act_{ij}^{[n]} - d \cdot (u_{ij}^{[n]} - r)] \cdot \chi_{\{Act_{ij}^{[n]} \geq 0\}}(Act_{ij}^{[n]}) + [(u_{ij}^{[n]} - m) \cdot \\ & \cdot Act_{ij}^{[n]} - d \cdot (u_{ij}^{[n]} - r)] \cdot \chi_{\{Act_{ij}^{[n]} < 0\}}(Act_{ij}^{[n]}) \end{aligned} \quad (\text{A.11})$$

where  $M$  and  $m$  are the maximum and minimum value that the pixels' value can take on and  $d$  and  $r$  are two learning coefficients related to the decay and the rest of the updating units, usually  $M = 1$ ,  $m = 0$ , while  $d = r = 0.1$ . It is possible to say that New IAC allows the pixels to coordinate themselves by exploiting the connections determined by AR. The areas where the pixel brightness is similar are moved toward white, while when there are sudden changes in luminance, the relevant pixels are led to dark.

### A.3 New CS

New Constraints Satisfaction Network (Buscema, 2006) (New CS) is an ACM system with fixed connections based on the constraint satisfaction network model [1]. The main idea behind New CS is to consider each pixel-agent of the matrix as a ‘‘hypothesis’’, which may be true or false in a fuzzy way, in relation to the brightness of the pixel itself. New CS tries to make every hypothesis of the matrix ‘‘true’’ by maximizing the brightness

of each pixel-agent, having as a constraint the value of fixed connections previously calculated with AR (Equations A.1–A.4). The maximization problem to solve is then:

$$Max \frac{1}{2} \cdot \sum_{i \in \{1, \dots, R\}, j \in \{1, \dots, C\}} \sum_{u_{xy} \in I_{ij}} u_{ij} \cdot u_{xy} \cdot w_{(ij), (xy)} \quad (\text{A.12})$$

*s.t.*

$$u_{ij} \in [0, 1] \quad \forall i \in \{1, \dots, R\} \text{ and } j \in \{1, \dots, C\} \quad (\text{A.13})$$

$$w_{(ij), (xy)} = \tanh(R'_{(ij), (xy)}) \quad \forall i, x \in \{1, \dots, R\} \text{ and } j, y \in \{1, \dots, C\} \quad (\text{A.14})$$

To achieve the maximization requested in Equation A.12, the units' values interact and evolve according to Equations A.15–A.17:

$$Net_{ij}^{[n]} = \sum_{(xy) \text{ s.t. } u_{xy} \in I_{ij}} u_{ij}^{[n]} \cdot w_{(ij), (xy)} \quad (\text{A.15})$$

$$\Delta_{ij}^{[n]} = Net_{ij}^{[n]} \cdot (1 - u_{ij}^{[n]}) \cdot \alpha \cdot \chi_{\{Net_{ij}^{[n]} \geq 0\}} (Net_{ij}^{[n]}) + Net_{ij}^{[n]} \cdot u_{ij}^{[n]} \cdot \alpha \cdot \chi_{\{Net_{ij}^{[n]} < 0\}} (Net_{ij}^{[n]}) \quad (\text{A.16})$$

$$u_{ij}^{[n+1]} = u_{ij}^{[n]} + \Delta_{ij}^{[n]} \quad (\text{A.17})$$

Thus,  $\Delta_{ij}^{[n]}$  pushes the unit's value towards higher or lower values according to the values of its neighborhood, weighted by the values of connections. The  $\alpha$  value is a parameter for adjusting the magnitude of corrections, generally  $\alpha = 1.0$ .

## A.4 Contractive Maps

Contractive Maps (CM) (Buscema, 2006) belongs to the first order of complexity family. The initial values  $u_{ij}^{[0]}$  remain unchanged over time and act as a constant impulse of the system. On the contrary, connections evolve over time, leading to the creation of new images. Equations A.18–A.20

show the  $w_{(ij),(xy)}^{[n]}$  updating process. To make it more easily legible, all the occurrences of  $u_{ij}^{[0]}$  have been replaced by  $u_{ij}$ ; furthermore, we use the parameter  $C = |I_{ij}|$ :

$$Net_{ij}^{[n]} = u_{xy} \cdot \left(1 - \frac{w_{(ij),(xy)}^{[n]}}{C}\right) \quad (\text{A.18})$$

$$AntiNet_{ij}^{[n]} = (u_{xy})^2 \cdot w_{(ij),(xy)}^{[n]} \cdot \left(1 - \frac{w_{(ij),(xy)}^{[n]}}{C}\right) \quad (\text{A.19})$$

$$\Delta w_{(ij),(xy)}^{[n+1]} = Net_{ij}^{[n]} \cdot AntiNet_{ij}^{[n]} \quad (\text{A.20})$$

At each iteration, a new image is drawn, i.e., new values  $P_{ij}^{[n]}$  for pixels must be computed. There exist different ways to do that, and Table A.1 shows some of them.

**Table A.1.** Some of the rules available to create new images

Name	Equation
Mean	$P_{ij}^{[n]} = \frac{1}{C} \cdot \sum_{\substack{(xy) \\ u_{xy} \in I_{ij}}} w_{(ij),(xy)}^{[n]}$
Variance	$P_{ij}^{[n]} = \sqrt{\frac{1}{C} \cdot \sum_{\substack{(xy) \\ u_{xy} \in I_{ij}}} \left[ \left( \frac{1}{C} \cdot \sum_{\substack{(xy) \\ u_{xy} \in I_{ij}}} w_{(ij),(xy)}^{[n]} \right) - w_{(ij),(xy)}^{[n]} \right]^2}$
Maximum	$P_{ij}^{[n]} = \max_{\substack{(xy) \\ u_{xy} \in I_{ij}}} \left( w_{(ij),(xy)}^{[n]} \right)$
Minimum	$P_{ij}^{[n]} = \min_{\substack{(xy) \\ u_{xy} \in I_{ij}}} \left( w_{(ij),(xy)}^{[n]} \right)$

At each iteration, the values of pixels of the image at the previous step are replaced by those computed by means of one of the methods of table A.1. Then, the values of connections are updated considering the original value of pixels. The process ends when the dynamic system reaches its attractor and  $\Delta w_{(ij),(xy)}^{[n]} \rightarrow 0$ .

## A.5 J-Net Dynamic

J-Net Dynamic (Buscema et al., 2008; Buscema and Grossi, 2010) is a ACM system with dynamic connections and units (third order of complexity). The main prerogative of this method is to consider in its equations not only the central pixel as such, with its relative neighborhood, but also as part of the surroundings of each of the pixels around it, when they are considered in turn as the central pixel. At the beginning of the process, the units  $u_{ij}$  are linearly scaled into the range  $[-1 + \alpha, 1 + \alpha]$ , where  $\alpha$  is a parameter to be set up. By varying the  $\alpha$  value it is possible to study images in an iterative manner. The first part of computations involves exclusively the central pixel and its neighborhood  $I_{ij}$ , as shown by Equations A.22–A.29. J-Net follows the schema: update of weights (Equations A.21–A.25, computation of the new pixel values based on the weights (Equation A.26), update of units (Equations A.29–A.38, re-update of weights and so on. In this case, the update of units also involves the neighborhoods  $I_{xy}$  such that  $u_{xy} \in I_{ij}$ .

$$S_{ij}^{[n]} = \pi \cdot (r_{ij}^{[n]})^2 \quad (\text{A.21})$$

$$D_{ij}^{[n]} = \sum_{(xy) \text{ s.t. } u_{xy} \in I_{ij}} (u_{ij}^{[n]} - w_{(ij),(xy)}^{[n]}) \quad (\text{A.22})$$

$$J_{ij}^{[n]} = \frac{e^{D_{ij}^{[n]}} - e^{-D_{ij}^{[n]}}}{e^{D_{ij}^{[n]}} + e^{-D_{ij}^{[n]}}} \quad (\text{A.23})$$

$$\Delta w_{(ij),(xy)}^{[n]} = -(u_{ij}^{[n]} - J_{ij}^{[n]}) \cdot (-2 \cdot J_{ij}^{[n]}) \cdot (1 - (J_{ij}^{[n]})^2) \cdot (u_{xy}^{[n]} - w_{(ij),(xy)}^{[n]}) \quad (\text{A.24})$$

$$w_{(ij),(xy)}^{[n+1]} = w_{(ij),(xy)}^{[n]} + \Delta w_{(ij),(xy)}^{[n]} \quad (\text{A.25})$$

$$P_{ij}^{[n]} = S_P \cdot \frac{1}{|I_{ij}|} \cdot \left( \sum_{(xy) \text{ s.t. } u_{xy} \in I_{ij}} w_{(ij),(xy)}^{[n]} \right) + O_P, \quad (\text{A.26})$$

where:

---


$$S_P = \frac{M_P}{M_w - m_w} \quad (\text{A.27})$$

$$O_P = -\frac{m_w \cdot M_P}{M_w - m_w}. \quad (\text{A.28})$$

$M_P$  denotes the maximum value available for pixels,  $M_w$  and  $m_w$  are, respectively, the maximum and the minimum weights  $w_{(ij),(xy)}^{[n]} \forall i, x \in \{1, \dots, R\}$  and  $j, y \in \{1, \dots, C\}$ .

$$Out_{ij}^{[n]} = S_0 \cdot \frac{1}{|I_{ij}|} \cdot \left( \sum_{(xy) s.t. u_{xy} \in I_{ij}} w_{(ij),(xy)}^{[n]} \right) + O_0 \quad (\text{A.29})$$

where, with the usual notation:

$$S_0 = \frac{2}{M_w - m_w} \quad (\text{A.30})$$

$$O_0 = -\frac{M_w + m_w}{M_w - m_w}. \quad (\text{A.31})$$

The internal activation state of each pixel is then defined as:

$$S_{ij}^{[n]} = |Out_{ij}^{[n]}|. \quad (\text{A.32})$$

Therefore, the closer the weighted average of the connections of each pixel with those of its surroundings is to a neutral value, 0 or 127 depending on the encoding, the higher the value of the internal activation state of the pixel itself. With the aim of defining an update rule for units, the quantity  $\Delta S_{(ij),(xy)}^{[n]}$  is considered (Equation A.33). Then, according to Equations A.34–A.35, the transition from  $I_{ij}$  to  $I_{xy}$  takes place.

$$\Delta S_{(ij),(xy)}^{[n]} = -\tanh(S_{ij}^{[n]} - u_{xy}^{[n]}) \quad (\text{A.33})$$

$$\varphi_{ij}^{[n]} = L \cdot u_{ij}^{[n]} \cdot \sum_{(xy) s.t. u_{xy} \in I_{ij}} \left( 1 - \left( \Delta S_{(xy),(ij)}^{[n]} \right)^2 \right) \quad (\text{A.34})$$

$$\psi_{ij}^{[n]} = \sum_{(xy) s.t. u_{xy} \in I_{ij}} \tanh(\varphi_{xy}^{[n]}). \quad (\text{A.35})$$

The delta quantities required for correction shall be calculated in the last step. It is possible to choose for two different update laws named union (Equation A.36) and intersection (Equation A.37).

$$\delta u_{ij}^{[n]} = \varphi_{ij}^{[n]} + \psi_{ij}^{[n]} \quad (\text{A.36})$$

$$\delta u_{ij}^{[n]} = \varphi_{ij}^{[n]} \cdot \psi_{ij}^{[n]} \quad (\text{A.37})$$

$$u_{ij}^{[n+1]} = u_{ij}^{[n]} + \delta u_{ij}^{[n]}. \quad (\text{A.38})$$

# APPENDIX B: ACM ELABORATIONS

In this appendix, some elaborations with ACM algorithms for Ortona's coast are shown (Fig. B.2, B.3, B.4, B.5). The first image on the top left is the original image used as input, while the others are processed by ACM algorithms, in order CM, AR, New CS and New IAC. It can be observed that in all cases, Contractive Maps algorithm gave a better definition of the shoreline and that on NIR2 band image it is more effective. Figure B.1 represents ACM Batch software platform.

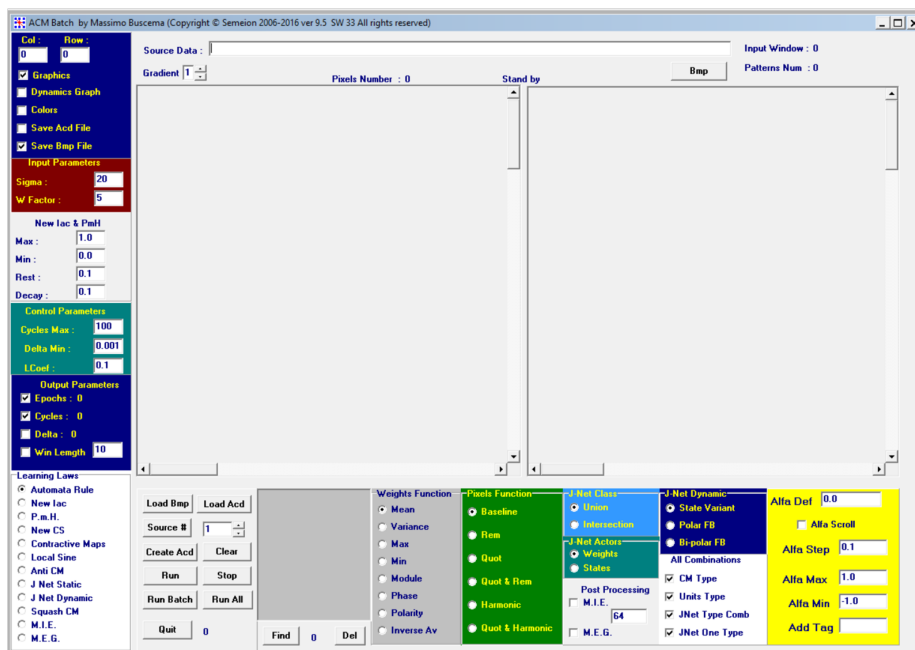
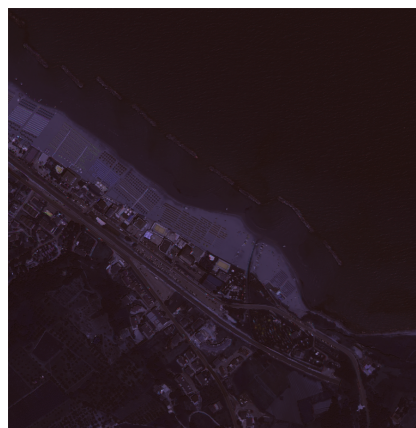


Figure B.1. ACM Batch software platform



a) Original 4-band image



b) Contractive Maps



c) Automata Rule



d) New CS



e) New IAC

**Figure B.2.** Four-band image elaborated by ACM filters



a) Original Coastal band image



b) Contractive Maps



c) Automata Rule



d) New CS



e) New IAC

**Figure B.3.** Coastal image elaborated by ACM filters

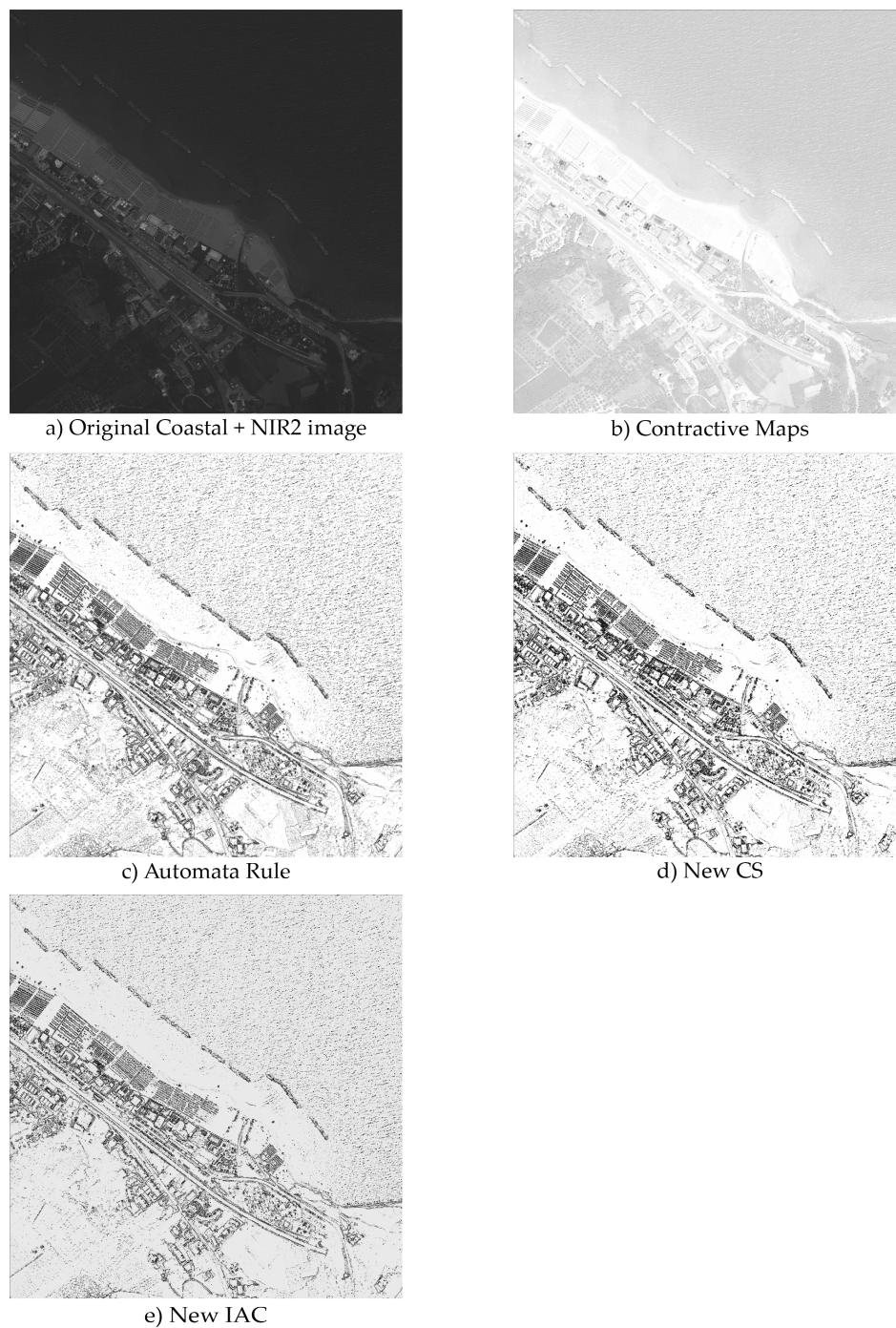


**Figure B.4.** Coastal plus NIR2 band image elaborated by ACM filters



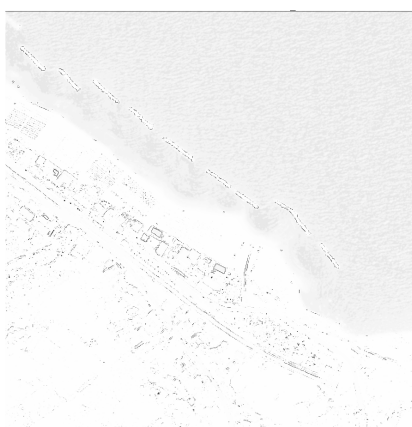
a) Original NIR2 image



b) Contractive Maps



c) Automata Rule



d) New CS



e) New IAC

**Figure B.5.** NIR2 band image elaborated by ACM filters